博士学位請求論文

論文題目　Functional analysis of

mucin-type core 1 glycan

in *Drosophila* neuromuscular junction

専 攻 名　生命情報工学専攻

学籍番号　12D5601

氏　　名　伊藤 和義

指導教員　西原 祥子

創 価 大 学 大 学 院
工 学 研 究 科

Functional analysis of mucin-type core 1 glycan in *Drosophila* neuromuscular junction

2018 年 9 月

Kazuyoshi Itoh

Table of contents

1. Introduction

Drosophila melanogaster (fruit fly) has been used as a model organism in modern biology. There are many benefits of using *Drosophila* as model organism. As about 60–70% of the *Drosophila* genes share homology with human genes, biological mechanism of *Drosophila* has a lot in common with that of human. Many of these shared genes are associated with diseases, such as cancer and muscular dystrophy. Another advantage of *Drosophila* is short life cycle. Crossing experiments can be performed easily, as generation interval of *Drosophila* is only 10 days at 25 °C. Moreover, genetic knowledges and techniques of *Drosophila* are fully accumulated, facilitating analyses using advanced genetic techniques, such as tissue-specific gene knockdown and genetic mosaic technique. Additionally, mutants and RNAi lines that cover almost all of *Drosophila* protein-coding genes are available from stock centers. Human disease model flies are also available. Therefore, *Drosophila* is very useful and excellent model organism to study gene function and human disease mechanism.

Drosophila neuromuscular junctions (NMJs) are widely used as a mammalian synapse model. There are some benefits of analyzing *Drosophila* NMJs. As *Drosophila* larval NMJs are large and easy to observe, histological and electrophysiological analyses are performed easily. For this reason, *Drosophila* NMJs are used as a model of the mammalian neuromuscular synapse. Moreover, *Drosophila* larval NMJ synapse is analogous to mammalian synapse in central nervous system (CNS) because both the synapses are glutamatergic. *Drosophila* NMJ synapse uses glutamate receptors (GluRs) corresponding to AMPA-type GluRs in the mammalian CNS, although mammalian NMJ synapse is acetylcholinergic. Therefore, *Drosophila* NMJs are also used as a model of the mammalian CNS synapse.

In *Drosophila* embryos and larvae, each abdominal segment is bilaterally symmetric, and 30 muscle cells numbered respectively are regularly arranged in each hemisegment (Fig. 1). Those muscle cells are innervated by motoneurons of which axons extend from the CNS. Axon terminal of each motoneuron forms NMJ boutons on each muscle. In this study, we focused on NMJs formed on muscles 6 and 7. NMJs are initially formed at the late stage of *Drosophila* embryogenesis (Prokop, 1999). During NMJ formation, RP3 motoneuron, which is a synaptic partner of the muscles 6 and 7, arrives at the ventral surface of the boundary between the two muscles and goes through the cleft between them (Chiba et al., 1993; Fig. 2). Then, on the dorsal surfaces of muscle 6/7, the branched axon terminal establishes synaptic contact with the two muscles and forms NMJ boutons. Subsequently, basement membranes (BMs) are formed and surround the surfaces of presynaptic bouton and postsynaptic muscle, except for the cleft between bouton and muscle. The BMs are essential for providing a rigid connection between bouton and muscle (Koper et al., 2012). During larval development, NMJs exhibit morphological change: NMJs dramatically enlarge, the number of boutons rises, and subsynaptic reticulum (SSR; postsynaptic structure) grows.
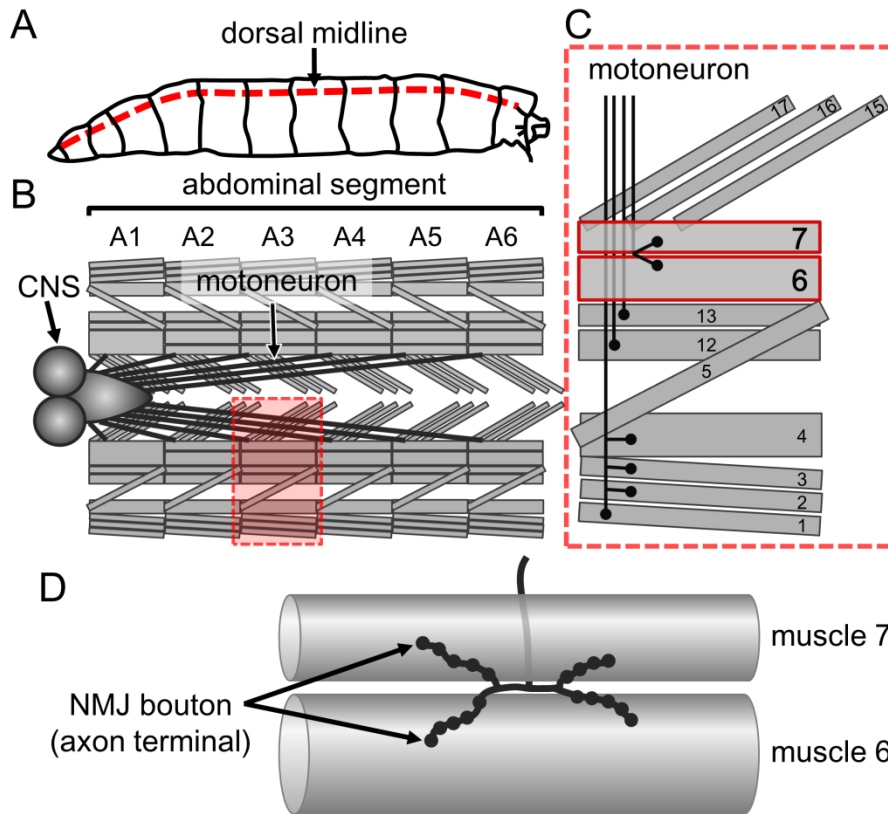
Fig. 1. Schematic diagram of *Drosophila* larval muscles and neuromuscular junctions.
(A) A *Drosophila* larva is shown. Dorsal midline of the larva is indicated in a red dotted-line.
(B) The structure of nervous system and body wall muscles after cutting on the dorsal midline are shown. Each abdominal segment is bilaterally symmetric, and 30 muscle cells are positioned in each hemisegment. Motoneuron axons extend from central nervous system to each segment.
(C) Magnified view of the area bordered by a rectangle in B is shown. Each muscle is numbered. Axon terminals contact with each muscle. Muscles 6 and 7, which are indicated in red, were analyzed in this study.
(D) Axon terminals form neuromuscular junction boutons near the boundary between muscles 6 and 7.
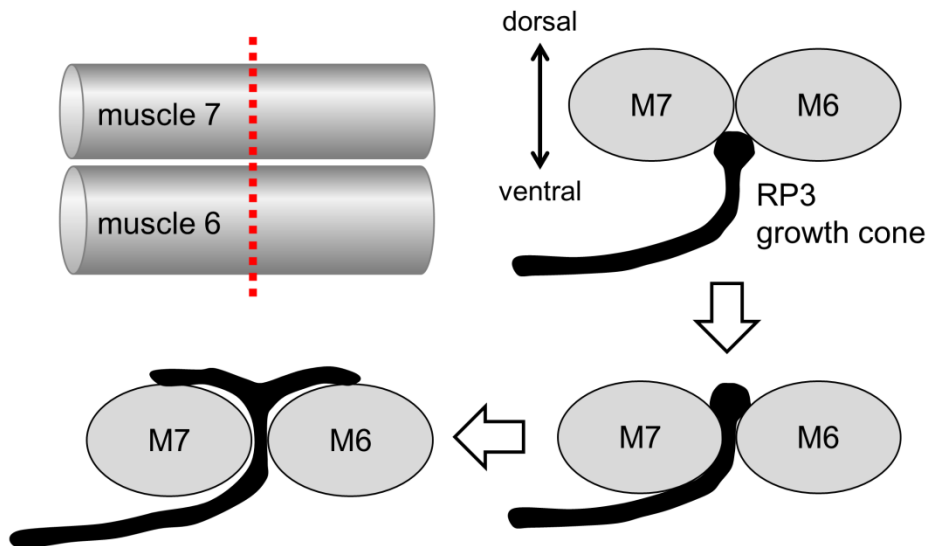
Fig. 2. Formation process of neuromuscular junctions on muscles 6 and 7 at the late stage of embryogenesis.
Cross sectional view of the muscle 6 (M6) and muscle 7 (M7) are indicated. At the late stage of embryogenesis, growth cone of RP3 motoneuron reaches ventral surface of the boundary between two muscles. Then, the RP3 growth cone passes through the muscle 6/7 cleft. Subsequently, it branches and forms neuromuscular junctions on the dorsal surface of two muscles.

3

The BM is a specialized extracellular matrix that is localized on the basal surface of epithelium and surrounds other tissues, such as nerve fibers, fat, and muscles (Timpl, 1989; Yurchenco and Schittny, 1990). Collagen IV (Col IV), perlecan, laminin, and nidogen (Ndg) are main BM components. There are three sources of BM proteins in *Drosophila*. Some parts of the epithelium produce their original BM proteins (Martin et al., 1999; Denef et al., 2008; Sorrosal et al., 2010). On the other hand, both fat body and hemocytes (blood cells) also produce BM proteins that are secreted to the body fluid and accumulated on the various tissue surfaces (Le Parco et al., 1986; Kusche-Gullberg et al., 1992; Yasothornsrikul et al., 1997, Pastor-Pareja and Xu, 2011).

The major BM components are proteins modified by glycans (sugar chains). The glycan is compound consisting of various monosaccharides connected in chain. It can modify proteins and lipids and have pleiotropic physiological functions in *vivo*. Protein glycosylation, which is one of the posttranslational modifications, is the reaction catalyzed by glycosyltransferases that add glycan to proteins. About 50% of the proteins synthesized in animal cells are glycosylated. There are two types of protein glycosylation. One is *O*-glycosylation, in which glycan is added to the serine (Ser) or threonine (Thr) residue of the core protein, the other is *N*-glycosylation, in which glycan is added to the asparagine (Asn) residue in consensus sequence (Asn-X-Ser/Thr) of the core protein.

Mucin-type *O*-glycosylation, one of the major types of *O*-glycosylation, is an evolutionarily conserved protein modification in the animals (Yang et al., 2012; Paschinger and Wilson, 2015). In this glycosylation, *N*-acetylgalactosamine (GalNAc) is initially added in an α1-linkage to Ser or Thr residues of the protein by polypeptide *N*-acetylgalactosaminyl-transferases (Fig. 3). This glycan structure is called Tn antigen (GalNAcα1-Ser/Thr). In mammals, eight distinct forms of mucin-type *O*-glycan have been identified (Brockhausen, 1999). T antigen (core 1 structure; Galβ1-3GalNAcα1-Ser/Thr) is the most general structure and is synthesized by core 1 β1,3-galactosyltransferase 1 (C1GalT1) that adds galactose (Gal) in a β1,3-linkage to GalNAc residues (Ju et al., 2002a, 2002b). In mammals, C1GalT1 cannot synthesize T antigen without Cosmc, which is a molecular chaperone for C1GalT1 (Ju and Cummings, 2002). Additionally, sialylated forms of mucin-type *O*-glycan such as sialylated T antigen (Siaα2-3Galβ1-3GalNAcα1-Ser/Thr) have been also identified (Brockhausen, 1999; Guzman-Aranguez and Argüeso, 2010).

Loss of Cosmc suppresses the capability of C1GalT1 to produce T antigen and leads to Tn syndrome, which shows hemolytic anemia and thrombopenia (Ju and Cummings, 2002, 2005; Narimatsu et al., 2008; Wang et al., 2010). Phenotypic analysis of *C1galt1*-knockout mice has revealed the functions of T antigen. The knockout mice exhibited embryonic lethality, brain hemorrhage, and angiogenetic defect (Xia et al., 2004; Xia and McEver, 2006). Tissue-specific knockout of *C1galt1* caused various aberrations, such as blood/lymphatic misconnections, spontaneous colitis, and thrombopenia (Fu et al., 2008; Fu et al., 2011; Kudo et al., 2013). Therefore, in mammals, T antigen can function in various tissues during development.

The functions of sialylated forms of mucin-type *O*-glycans have been also analyzed. The minus-charged sialic acids on podocalyxin, which is a mucin-type *O*-glycoprotein, provide this core protein for anti-adhesive properties required for filtration slit formation in the glomerular epithelium of the kidneys

(Takeda et al., 2000; Doyonnas et al., 2001). In the lymphatic endothelium, sialylated core 1 glycans on podoplanin prevent this protein from degradation and were required for the interaction with platelets (Pan et al., 2014). Moreover, sialylated core 1 glycans on α-dystroglycan were essential for the acetylcholine receptor (AChR) clustering in a mouse myoblast cell line (McDearmon et al., 2003). Therefore, sialylated mucin-type *O*-glycans also play various roles in mammals.
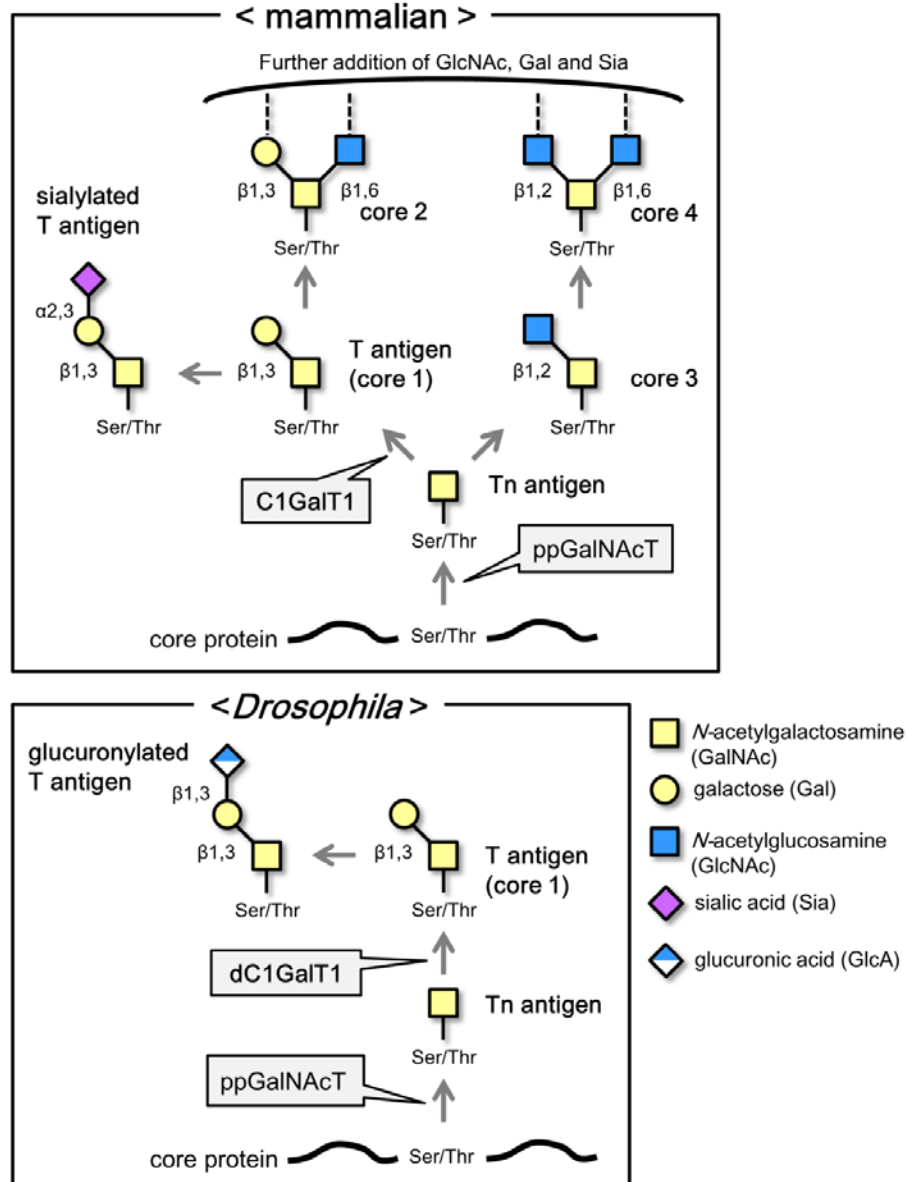
Fig. 3. Biosynthesis of mucin-type *O*-glycans in mammalian and *Drosophila*.
In mammalian, polypeptide *N*-acetylgalactosaminyl-transferases (ppGalNAcTs) transfer *N*-acetylgalactosamine (GalNAc) in an α1-linkage to serine (Ser) or threonine (Thr) residues of core protein to synthesize Tn antigen (GalNAcα1-Ser/Thr). Core 1 β1,3-galactosyltransferase 1 (C1GalT1) transfers galactose (Gal) in a β1,3-likage to GalNAc residues to synthesize T antigen (core 1; Galβ1-3GalNAcα1-Ser/Thr). Then, sialic acid (Sia) is transferred in an α2,3-linkage to Gal residues, and sialylated T antigen (Siaα2-3Galβ1-3GalNAcα1-Ser/Thr) is synthesized. Moreover, core 2, core 3, and core 4 structures are also synthesized, and then those glycan structures are extended by the addition of GlcNAc, Gal, and Sia. In addition, core 5–8 structures are also synthesized.
In *Drosophila*, Tn antigen and T antigen are synthesized by ppGalNAcTs and *Drosophila* C1GalT1 (dC1GalT1), respectively. Unlike the mammalian, glucuronic acid (GlcA) is transferred in a β1,3-likage to Gal residues of T antigen, and glucuronylated T antigen (GlcAβ1-3Galβ1-3GalNAcα1-Ser/Thr) is synthesized. This glycan structure is considered

to correspond to sialylated T antigen in mammalian.

In *Drosophila*, three main structures of mucin-type *O*-glycan, i.e., Tn antigen, T antigen, and glucuronylated T antigen (GlcAβ1-3Galβ1-3GalNAcα1-Ser/Thr), have been identified (Kramerov et al., 1996; Aoki et al., 2008; Breloy et al., 2008; Fig. 3). *Drosophila* C1GalT1 ortholog (dC1GalT1) can predominantly synthesize T antigen (Müller et al., 2005). Unlike the mammalian orthologs, a molecular chaperone such as Cosmc was not required for the enzymatic activity of dC1GalT1. Despite presence of sialylated T antigen in mammals, this glycan structure has never been identified in *Drosophila* (Schwientek et al., 2007; Aoki et al., 2008). However, a minus-charged glucuronic acid (GlcA) can modify T antigen in *Drosophila*. In previous reports, glucuronylated T antigen was found in other species, including *C. elegans*, mosquito, and several Rana species (Florea et al., 1997; Coppin et al., 1999; Guérardel et al., 2001; Mourad et al., 2001; Kurz et al., 2015). Three *Drosophila* β1,3-glucuronyltransferases (dGlcATs), i.e., dGlcAT-I, dGlcAT-S, and dGlcAT-P, have been identified. Previous reports revealed that both dGlcAT-S and dGlcAT-P had enzymatic activity toward T antigen *in vitro*, but only dGlcAT-P had that activity in S2 cells (Kim et al., 2003; Breloy et al., 2016).

In previous studies, we demonstrated that in *Drosophila*, T antigen produced by dC1GalT1 was localized in various tissues, such as CNS, embryonic hemocytes, and lymph glands (Yoshida et al., 2008; Fuwa et al., 2015). *dC1GalT1* mutant larvae exhibited various phenotypes, e.g., the abnormal extension of ventral nerve cord (VNC), malformation of brain hemispheres, reduced number of embryonic hemocytes, and hyper-differentiation of hematopoietic stem cells (Lin et al., 2008; Yoshida et al., 2008; Fuwa et al., 2015). Thus, T antigen has plural functions in various *Drosophila* tissues. In addition, as is the case with *dC1GalT1* mutants, the abnormal extension of VNC was also observed in *dGlcAT-P* null mutant larvae (Pandey et al., 2011), indicating the possibility that the absence of glucuronylated T antigen may cause this phenotype. However, in contrast to the core 1 glycan, the physiological roles of glucuronylated core 1 glycan has not yet been clarified.

In this study, to elucidate the physiological functions of glucuronylated core 1 glycans, we analyzed the phenotypes of both *dC1GalT1* and *dGlcAT-P* mutants. Both the mutant larvae exhibited three phenotypes, i.e., (1) a partial absence of BM components at the border between muscles 6 and 7, (2) ectopic positioning of NMJ boutons at the border between two muscles, and (3) reduced number of NMJ branches. We found a genetic interaction between *dC1GalT1* and *dGlcAT-P*. Furthermore, ultrastructural analysis of NMJ boutons showed that both the mutants displayed shorter length of postsynaptic density (PSD). Together, these results demonstrated that in *Drosophila*, glucuronylated core 1 glycans synthesized by both dC1GalT1 and dGlcAT-P were required for the BM formation, NMJ bouton localization, NMJ arborization, and PSD organization.

2. Materials and Methods

2-1. Fly stocks and mutant establishment

All flies were reared and maintained at 25 °C. Canton-S or w^{1118} strain of *Drosophila melanogaster* was used as the wild-type (WT). The following stocks were also used: *dC1GalT1^{EY13370}* (Bloomington *Drosophila* Stock Center [BDSC]), *dC1GalT1$^{2.1}$* (BDSC), *Df(2L)Exel7040* (BDSC), *Df(3L)BSC817* (BDSC), and *vkg^{G454}* (Kyoto Stock Center [DGRC]). *Df(2L)Exel7040* is a chromosomal deficiency in which *dC1GalT1* gene is completely deleted (Lin et al., 2008). *Df(3L)BSC817* is a chromosomal deficiency in which *dGlcAT-P* gene is completely deleted (Pandey et al., 2011). The following stocks were used for the rescue experiments: *Act5C-Gal4* (BDSC), *UAS-dC1GalT1* (Fly Stocks of National Institute of Genetics [NIG-Fly]), and *UAS-dGlcAT-P* (NIG-Fly). *dGlcAT-P^{SK1}* and *dGlcAT-P^{SK6}* strains were established by using the CRISPR/Cas9 system, as described previously (Kondo and Ueda, 2013).

2-2. Quantitative real-time PCR analysis

Total RNA was extracted from each genotype by using TRIzol II Reagent (Invitrogen, Carlsbad, CA, USA). cDNA was synthesized by using a SuperScript First Strand Synthesis Kit (Invitrogen) and oligo-dT primers (Invitrogen). Real-time PCR was carried out by using Fast Start Universal SYBR Green Master (Rox; Roche Diagnostics, Basel, Switzerland) and an ABI PRISM 7500 Sequence Detection System (Applied Biosystems, Foster City, CA, USA). Real-time PCR primers are indicated in Table 1. *Ribosomal protein L32* (*RpL32*) mRNA in each cDNA sample was measured to normalize the efficiency of cDNA synthesis among individual samples. Amplifications involved 40 cycles of 94 °C for 30 s and 60 °C for 4 min were carried out with a QuantStudio™ 12K Flex Real-Time PCR System (Thermo Fisher Scientific, Waltham, MA, USA). For the quantification of *dGlcAT-P* mRNA, the measurements were evaluated by absolute quantification using standard constructs cloned into a nearly 400 bp amplicon in pGEM®-T Easy Vector (Promega, Fitchburg, WI, USA). The standard constructs were amplified using standard PCR primers indicated in Table 2.

Table 1. Primer sets for real-time PCR analysis.

Gene	Detectable splicing variant	Real-time PCR primer	
		Forward	Reverse
RpL32	RA, RB, RC, RD	GCAAGCCCAAGGGTATCGA	CGATGTTGGGCATCAGATACTG
dGlcAT-P	RB, RC, RE	CTATCAGTACCACATATCCCGTGAA	GTAGGTGGGCGTGATTATGTACAG

Table 2. Primer sets for amplification of standard constructs.

Gene	Amplifiable splicing variant	Standard PCR primer	
		Forward	Reverse
dGlcAT-P	RB, RC, RE	TTTCATCCTGACCACCTG	ATGTCGTAGGTGTTGTCG

2-3. Lectin blotting and immunoblotting

Ten third instar larvae were dissected in phosphate-buffered saline (PBS). The larval body walls, including cuticulated epithelia and muscles, were homogenized in 100 µL of buffer containing 150 mM NaCl, 5 mM $MgCl_2$, 50 mM Tris-HCl (pH 7.4), 1% Triton X-100, 0.1% sodium deoxycholate, 5 mM 2-mercaptoethanol, and 10% glycerol with protease inhibitors (2 µg/mL pepstatin A, 2 µg/mL leupeptin, 2 µg/mL aprotinin, and 1 mM PMSF). After centrifugation at 5,000 rpm for 5 min, the supernatant was used as the total extracts of larval body wall muscles. These extracts were subjected to 10% sodium dodecyl sulfate-polyacrylamide gel electrophoresis (SDS-PAGE). The separated proteins were transferred to Immobilon-P membranes (Millipore, Billerica, Massachusetts, USA), and then these membranes were probed with following lectins and antibodies: horseradish peroxidase-conjugated *Helix pomatia* agglutinin (HPA-HRP; 1000; EY laboratories, San Mateo, CA, USA), HRP-conjugated peanut agglutinin (PNA-HRP; 1:10000; J-Oil Mills, Tokyo, Japan), mouse anti-α-tubulin antibodies (1:10,000; Developmental Studies Hybridoma Bank [DSHB], Iowa City, IA, USA or 1:20,000; Sigma-Aldrich, St. Louis, MO, USA), and rabbit anti-dGlcAT-P antibody (Eurofins Genomics, Tokyo, Japan). The mouse anti-α-tubulin was used as an internal loading control. The rabbit anti-dGlcAT-P antibody was produced against the dGlcAT-P peptide C-KNTNLEHIDRLLVR. Then, the membranes were labeled with an ECL Prime western blotting detection reagent (GE Healthcare, Little Chalfont, UK) in accordance with the manufacturer's instructions.

2-4. Lectin precipitation and immunoprecipitation

Sixty third-instar larvae of $vkg^{G454}/+$ were bled in 100 µL of PBS containing protease inhibitors (2 µg/mL pepstatin A, 2 µg/mL leupeptin, 2 µg/mL aprotinin, and 1 mM PMSF) and 5 mM EDTA. 5 µL of streptavidin magnetic beads (New England Biolabs, Ipswich, MA, USA) or protein G magnetic beads (New England Biolabs) was reacted with 400 µg of corrected total protein at 4 °C for 1 h in order to exclude the proteins that bind to those magnetic beads. After the removal of the magnetic beads, the proteins were reacted with 2 µg of biotinylated PNA (Cosmo Bio, Tokyo, Japan) or mouse anti-GFP antibody (12A6; DSHB) at 4 °C for overnight. This solution was reacted with 10 µL of streptavidin magnetic beads or protein G magnetic beads at 4 °C for 6 h. After washing the magnetic beads with PBS, the proteins binding to the beads were eluted in 20 µL of sample buffer (0.25 M Tris-HCl [pH 6.8], 8% SDS, 4% 2-mercaptoethanol, and 40% glycerol) at 99 °C for 5 min. Eluted proteins were used for lectin blotting by using PNA-HRP (1:10,000) and immunoblotting by using a mouse anti-GFP antibody (1:1,000; Sigma-Aldrich).

2-5. Pretreatment for tissue observation

Wandering third instar larvae from each genotype were dissected along the dorsal midline in PBS or zero-calcium HL3 saline. After removal of the digestive tracts, fat bodies, main tracheae, and CNS, the body walls, including cuticulated epithelia and muscles, were fixed as indicated below.

2-6. Lectin staining and immunostaining

The larval body walls were fixed with 4% paraformaldehyde (PFA) in PBS at room temperature for 20

min. Then, these tissues were washed with either PBS for lectin staining or PBS containing 0.1% Triton X-100 (PBS-T) for immunostaining. Tn antigen and T antigen were labeled with rhodamine-conjugated HPA (HPA-rhodamine; 1:100; EY laboratories) and Alexa Fluor-488-conjugated PNA (PNA-488; 1:50; J-Oil Mills), respectively. The following primary antibodies were used for the immunostaining: rabbit anti-Ndg antibody (1:500; kindly provided by Anne Holz, Justus Liebig University Giessen, Giessen, Germany), rabbit anti-HRP antibody (1:100; MP Biomedicals, Santa Ana, CA, USA), mouse anti-fasciclin II (Fas II) antibody (1:20; DSHB), and mouse anti-Discs large (Dlg) antibody (1:100; DSHB). Primary antibodies were incubated with the fixed tissues in PBS-T at 4°C overnight. All lectins, secondary antibodies (1:300; Life Technologies, Carlsbad, CA, USA), Hoechst 33342 (5 µg/mL; Invitrogen), and Acti-stain 555 phalloidin (1:300; Cytoskeleton, Denver, CO, USA) were incubated with the tissues in PBS or PBS-T at room temperature for 2.5 h. Subsequently, stained tissues were mounted in 90% glycerol in Tris-HCl (pH 7.4). Images of the tissues were collected on an LSM 700 (Carl Zeiss, Jena, Germany) confocal laser microscope. Relative fluorescence intensities of HPA-rhodamine and PNA-488 on the muscle surface and at NMJs were quantified by using NIH ImageJ software.

2-7. *Atmospheric scanning electron microscopy imaging*

Tissues were fixed with 4% PFA in PBS at room temperature for 20 min. The tissues were stained using a slight modification (Memtily et al., 2015) of the NCMIR method developed by the Ellisman group (Deerinck et al., 2010). The tissues were washed with PBS and then further fixed with 2.5% glutaraldehyde and 2% PFA in 0.15 M cacodylate buffer (pH 7.4) containing 2 mM $CaCl_2$ at room temperature for 15 min. Tissues were then washed with 0.15 M cacodylate buffer (pH 7.4) containing 2 mM $CaCl_2$ and further fixed and stained with 1.5% potassium ferricyanide (Sigma-Aldrich) and 2% aqueous osmium tetroxide (OsO_4) (Nisshin EM, Tokyo, Japan) in the same buffer containing 2 mM $MgCl_2$ at room temperature for 10 min. After washing with deionized distilled water (DDW), the tissues were incubated with filtered 1% thiocarbohydrazide (TCH; Tokyo Chemical Industry, Tokyo, Japan) at room temperature for 20 min, washed with DDW, and further stained with 2% aqueous OsO_4 at room temperature for 5 min. After washing with DDW, tissues were stained with filtered 2% uranyl acetate in DDW and incubated at 4°C overnight. Finally, the tissues were washed with DDW and stained with 0.4% lead citrate (TAAB Laboratories Equipment, Aldermaston, UK) at room temperature for 2 min.

Direct observation of wet tissues using atmospheric scanning electron microscopy (ASEM) was performed as described previously (Nishiyama et al., 2010; Memtily et al., 2015). We used a 35-mm ASEM dish that had eight 100-nm-thick, 250 × 250-µm SiN film windows. After fixation and staining, a tissue was placed on the SiN film windows, and a drop of 10 mg/mL (w/v) d-glucose (dextrose; MP Biomedicals) was added on the tissue. A weighted cover glass was then positioned on the upper surface of the wet tissue, and the electron beam was projected onto the tissue surface through the SiN film. The ClairScope ASEM system (JASM-6200; JEOL, Tokyo, Japan) was used to record SEM images (Nishiyama et al., 2010). The acceleration voltage of the SEM was 30 kV.

2-8. Transmission electron microscopy imaging

Transmission electron microscopy (TEM) was carried out as described previously (Ueyama et al., 2010). Tissues were fixed with 2.5% glutaraldehyde in PBS at 4°C overnight. The tissues were then postfixed with 1% OsO_4 in 100 mM phosphate buffer (pH 7.3) at 4°C for 1 h and dehydrated in a graded series of ethanol. After passage through propylene oxide, the specimens were embedded in Epon 812. Ultrathin sections were cut, stained with uranyl acetate and lead citrate, and observed with a TEM (JEM-1010C; JEOL). From two to four larvae of each genotype were analyzed. Vesicles diameter, PSD length, SSR thickness, bouton area, and postsynaptic pocket (PSP) depth were measured using NIH ImageJ software. When measuring vesicle diameter, 30 vesicles were randomly chosen from each bouton. SSR thickness and SSR density (layer number/SSR thickness) were measured in accordance with previously described methods (Budnik et al., 1996).

2-9. Construction, purification, and immunoblotting of FLAG-tagged dGlcAT proteins

Each dGlcAT splicing variant (dGlcAT-I, dGlcAT-P-I, dGlcAT-P-II, dGlcAT-S-I, dGlcAT-S-II, and dGlcAT-S-III) was expressed in *Sf21* insect cells by using GATEWAY™ Cloning Technology (Thermo Fisher Scientific) in accordance with previously reported methods (Ichimiya et al., 2004). DNA fragments of each dGlcAT splicing variants were amplified using PCR primers indicated in Table 3. The amplified DNA fragments were recombined with the pDONR™201 vector, and the inserts were introduced to produce pVL-FLAG-*dGlcATs* (*dGlcAT-I*, *dGlcAT-P-I*, *dGlcAT-P-II*, *dGlcAT-S-I*, *dGlcAT-S-II*, and *dGlcAT-S-III*). pVL-FLAG is a vector come from pVL1393 including the FLAG peptide (DYKDDDDK) and signal sequence of human immunoglobulin κ (MHFQVQIFSFLLISASVIMSRG) at the N-terminal. Each pVL-FLAG-*dGlcAT* was transfected into *Sf21* cells in accordance with previously reported methods (Ichimiya et al., 2004). The culture of each infected cell including FLAG-tagged dGlcAT proteins were applied to an anti-FLAG M1 affinity gel for the purification of those proteins (Sigma-Aldrich). Each purified FLAG-tagged dGlcAT protein and FLAG-BAP Control Protein (Sigma-Aldrich) were subjected to SDS-PAGE. The separated proteins were transferred to an Immobilon-P membrane (Millipore), and then this membrane was probed with a mouse anti-FLAG M1 antibody (Sigma-Aldrich). The membrane was then stained by TMB Membrane Peroxidase Substrate (SeraCare Life Sciences, Milford, MA, USA). In order to quantify the purified proteins, the band intensity was measured by a densitometer. The more information of each FLAG-tagged dGlcAT protein is indicated in Table 4.

Table 3. Primer sets for amplification of DNA fragments of *dGlcAT* splicing variants.

Gene	Amplifiable splicing variant	PCR primer		Source
dGlcAT-I	-	Forward	AAAAAGCAGGCTACGGGAAGCGCACATGCCAG	EST clone GH13618
		Reverse	AGAAAGCTGGGTTTAGACCTCCATGCCGCCATC	
dGlcAT-P	I	Forward	AAAAAGCAGGCTTGTGGTCACCCATTTCCCTGCT	cDNA of Canton-S

				embryos
	II	Reverse	AGAAAGCTGGGTCAGTAAATATCCCTATGGCC	
		Forward	AAAAAGCAGGCTTGCCGCCCCTGTACATAATCA	
		Reverse	AGAAAGCTGGGTCAGTAAATATCCCTATGGCC	
dGlcAT-S	I, II	Forward	AAAAAGCAGGCTCCGAGGATTCGGAGGAGGGATCT	cDNA of Canton-S
		Reverse	AGAAAGCTGGGTTCAGCTAAGAATTTTGGAGTGTGG	embryos
	III	Forward	AAAAAGCAGGCTCCGAGGATTCGGAGGAGGGATCT	cDNA of Canton-S
		Reverse	AGAAAGCTGGGTTCAGCTAAGAATTTTGGAGTGTGG	third-instar larvae

2-10. Measurement of glucuronic acid transferase activity

We measured GlcA transferase activity of each dGlcAT splicing variant toward *p*-nitrophenol labeled T antigen (Galβ1-3GalNAcα1-*p*NP; Toronto Research Chemicals, Toronto, Canada), as an acceptor substrate. The enzymatic reaction occurred at 25 °C for 4 h in 20 μL of a mixture that includes 2 picomoles of each FLAG-tagged dGlcATs, 5 nanomoles of acceptor substrate, 95 μM UDP-GlcA (Sigma-Aldrich), 5μM UDP-[^{14}C]GlcA (300 mCi/mmol; PerkinElmer, Waltham, MA, USA), 2 mM MnCl$_2$, and 50 mM MES buffer (pH 6.5), respectively. The enzymatic reaction was stopped by adding 400 μL of H$_2$O. After centrifugation, the supernatant was applied onto a Sep-PakC18 column (Merck Millipore, Billerica, MA, USA) balanced with H$_2$O. The column was washed with H$_2$O to remove unreacted UDP-GlcA and UDP-[^{14}C]GlcA, and then the enzymatic reaction products were eluted with methanol. Radioactivity of the products was detected by using a liquid scintillation counter Tri-Carb 3100TR (PerkinElmer). In addition, The enzymatic reaction for mass-spectrometry (MS) analysis was carried out at 25 °C for 22 h in 100 μL of a mixture that includes 150 picomoles of FLAG-tagged dGlcAT-P-II, 30 nanomoles of acceptor substrate, 500 μM UDP-GlcA, 2 mM MnCl$_2$, and 50 mM MES buffer (pH 6.5).

2-11. Determination of glycan structure by mass spectrometry

The enzymatic reaction products were permethylated with ^{12}C-methyliodine before MS analysis in accordance with previously described methods (Anumula and Taylor, 1992). Malto-series oligosaccharide standards (maltotriose [Dp3] and maltotetraose [Dp4]; Sigma-Aldrich) were permethylated with ^{13}C-methyliodine (^{13}C-MeI). Glycan structure of the products was examined by nanospray ionization-mass spectrometry (NSI-MS). The amount of the enzymatic products was determined relative to that of maltotriose (Dp3) and maltotetraose (Dp4) standards, and the products were added into the sample before infusion (Mehta et al., 2016). Glycan samples were rearranged in 50% methanol including 1 mM NaOH (Thermo Fisher Scientific) for infusion and transfused into a linear ion trap mass spectrometer (LTQ; Thermo Fisher Scientific) by using a nanoelectrospray source. The instrument was tuned with permethylated oligosaccharide standard for positive ion mode. For fragmentation by collision-induced dissociation (CID) in MS/MS, normalized collision energy of 30% to 35% was used. Detection of glycans was carried out by using total ion mapping functionality of Xcalibur software package version 2.0 (Thermo Fisher Scientific) in accordance with previously described methods (Aoki et al., 2007). Glycans were identified as singly sodiated

species [M+Na] in positive mode.

2-12. Assay of larval locomotor activity

A paper, on which multiple circles (1–8 cm in diameter) were drawn, was put under a 9 cm plastic dish with 3% agar solution, as indicated in Figure 21A. A wandering third-instar larva of each genotype was laid in the middle of circles. The moving distance of the larva during 30 s was determined. At least 18 larvae of each genotype were assayed.

2-13. Statistical analysis

Statistical assessment was performed by Student's *t*-test or multiple comparison tests, i.e., the Dunnett test, Tukey-Kramer test, Steel test, and Steel-Dwass test, using Microsoft Excel 2010. A *P*-value of less than 0.05 was considered significant.

3. Results

3-1. dC1GalT1 mutants showed decreased expression of T antigen in the muscles and neuromuscular junctions

We used two mutant alleles of the *dC1GalT1* gene. One is *dC1GalT1^{EY13370}* (*T1^{EY}*), which had a P-element insertion in the first intron of the *dC1GalT1* gene region (Fig. 4B, upper), the other is *dC1GalT1^{2.1}* (*T1^{2.1}*), which was previously described as a null allele (Lin et al., 2008; Fig. 4B, lower). Then, we analyzed *T1^{EY}/T1^{EY}* and *T1^{EY}/T1^{2.1}*as *dC1GalT1* mutants. The mRNA levels of *dC1GalT1* were significantly decreased in *T1^{EY}/T1^{EY}* and *T1^{EY}/T1^{2.1}* compared with those in WT larvae (Fig. 4C).

PNA can recognize T antigen (Galβ1-3GalNAcα1-Ser/Thr) synthesized by dC1GalT1, while HPA can recognize Tn antigen (GalNAcα1-Ser/Thr) (Fig. 4A). Therefore, in order to estimate the expression levels of T antigen in the muscles of the two mutant larvae, we performed PNA and HPA lectin blot analyses by using the extracts of larval body wall muscles (Fig. 4D). The bands detected by PNA were reduced in the two mutants compared with those in the WT larvae (Fig. 4D, left panel). In contrast, the bands detected by HPA were increased in the two mutants compared with those in the WT larvae (Fig. 4D, right panel). Thus, T antigen synthesized by dC1GalT1 was expressed in the muscles. For subsequent experiments, we analyzed *T1^{EY}/T1^{2.1}* as the *dC1GalT1* mutant rather than *T1^{EY}/T1^{EY}* because the influence of potential secondary site mutations was avoided and because the expression level of *dC1GalT1* transcripts in *T1^{EY}/T1^{2.1}* was lower than that in *T1^{EY}/T1^{EY}*.

We next test whether T antigen expression is reduced on the muscle surface in *dC1GalT1* mutant larvae using lectin staining without permeabilization with PNA-488 and HPA-rhodamine. T antigen expression on the muscle surface was significantly reduced in *dC1GalT1* mutants compared with that in WT larvae (Fig. 4E, left panels and Fig. 4G, left panel), while Tn antigen expression on the muscle surface was significantly increased in *dC1GalT1* mutants compared with that in WT larvae (Fig. 4E, right panels and Fig. 4G, right panel). In this way, the absence of dC1GalT1 led to the reduction in T antigen expression and the increase in Tn antigen expression on the muscle surface. We then analyzed the expression levels of T antigen and Tn antigen at larval NMJs. Presynaptic NMJ boutons were labeled with anti-HRP antibody (Fig. 4F, left panels). T antigen expression at the NMJs significantly reduced in *dC1GalT1* mutants compared with that in WT larvae (Fig. 4F, middle panels and Fig. 4H, left panel). However, Tn antigen expression at the NMJs was similar in the WT and *dC1GalT1* mutant larvae (Fig. 4F, right panels and Fig. 4H, right panel). Thus, T antigen produced by dC1GalT1 was expressed on muscle surface and at NMJs.
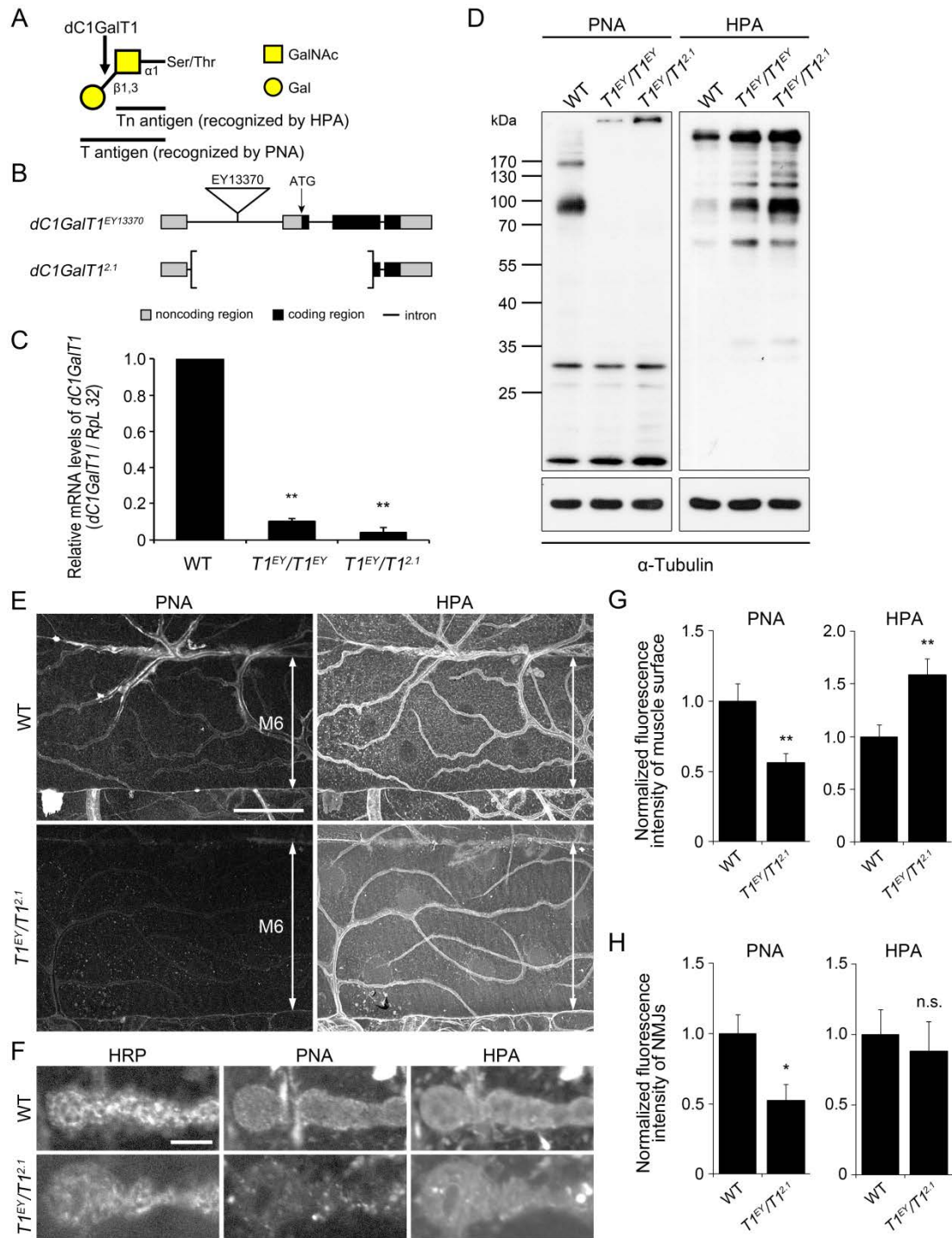
Fig. 4. Reduced expression of T antigen in muscles and neuromuscular junctions in *dC1GalT1* mutants.
(**A**) The glycan structure of Tn antigen and T antigen (core 1 structure). To synthesize T antigen, *Drosophila* core 1 β1,3-galactosyltransferase 1 (dC1GalT1) adds galactose (Gal) in a β1,3-linkage to *N*-acetylgalactosamine (GalNAc) of Tn antigen.
(**B**) Two mutant alleles of the *dC1GalT1* gene are shown. In *dC1GalT1*^{EY13370} (*T1*^{EY}), P-element (EY13370) indicated by a triangle was inserted into the first intron of the *dC1GalT1* gene. The *dC1GalT1*$^{2.1}$ (*T1*$^{2.1}$) was the null allele. Gray and black boxes indicate noncoding and coding regions, respectively.
(**C**) Relative expression levels of *dC1GalT1* transcripts in *T1*^{EY}/*T1*^{EY} and *T1*^{EY}/*T1*$^{2.1}$ third instar larvae. The expression level in the wild-type (WT) larvae was set as 1.0. Experiments were repeated three times. Data are indicated as the mean ± standard error for each genotype. Statistical significance was assessed by Dunnett's test. **$P < 0.01$.
(**D**) Upper panel, peanut agglutinin (PNA) and *Helix pomatia* agglutinin (HPA) lectin blot analyses of WT, *T1*^{EY}/*T1*^{EY}, and *T1*^{EY}/*T1*$^{2.1}$ larval body wall muscles. Lower panel, α-tubulin internal control. Experiments were repeated three times.

14

A representative example is shown.

(E) Confocal images of muscle 6 at abdominal segment 3 in WT (upper) and $T1^{EY}/T1^{2.1}$ (lower) third instar larvae. Surface sectional views of the muscle are indicated. The width of muscle 6 (M6) is shown by a double-headed arrow. T antigen and Tn antigen were labeled with Alexa Fluor-488-conjugated PNA (PNA-488) and rhodamine-conjugated HPA (HPA-rhodamine), respectively, without permeabilization. Cell nuclei (DNA) are stained with Hoechst 33342. Representative examples are shown. Scale bar: 50 µm.

(F) Confocal images of neuromuscular junctions (NMJs) on muscle 6 at abdominal segment 3 in WT (upper) and $T1^{EY}/T1^{2.1}$ (lower) third instar larvae. NMJs were stained with anti-HRP antibodies (a presynaptic NMJ bouton), PNA-488, and HPA-rhodamine without permeabilization. Representative examples are shown. Scale bar: 5 µm.

(G) Relative fluorescence intensities of PNA-488 (left) and HPA-rhodamine (right) on muscle surfaces normalized to the average of the WT data. Data are the mean ± standard error for each genotype (n = 8–10). Statistical significance was assessed by Student's t-test. **$P < 0.01$.

(H) Relative fluorescence intensities of PNA-488 (left) and HPA-rhodamine (right) at NMJs normalized to the average of the WT data. Data are the mean ± standard error for each genotype (n = 6–9). Statistical significance was assessed by Student's t-test. *$P < 0.05$, n.s.: not significant.

3-2. dC1GalT1 mutants exhibited an absence of collagen IV at the muscle 6/7 border

To test whether *dC1GalT1* mutant larvae show muscle phenotype, we labeled the BMs on muscle cells. For labeling the BM component, we used a Viking (Vkg) GFP-trap line, vkg^{G454} (Morin et al., 2001), in which a GFP protein-trap was inserted into the *Drosophila vkg* gene that encodes the α chain of collagen IV (Col IV); a functional GFP-tagged Vkg (Vkg-GFP) protein was produced (Morin et al., 2001; Pastor-Pareja and Xu, 2011). On the surface of muscles 6 and 7, Vkg-GFP was evenly expressed in both control (Fig. 5A) and *dC1GalT1* mutant (Fig. 5B) larvae. In internal sectional views of the muscles, Vkg-GFP was expressed along the lines with border between muscles 6 and 7 in controls (Fig. 5A′), whereas Vkg-GFP was partially lost at the muscle 6/7 border in the *dC1GalT1* mutants (arrowheads in Fig. 5B′). The percentage of Vkg-GFP loss phenotype in $T1^{EY}/T1^{2.1}$ and $T1^{EY}/Df$ (vkg^{G454}, $dC1GalT1^{EY13370}/Df(2L)Exel7040$) were much higher than that in controls (Fig. 5D). The total range of Vkg-GFP loss at the muscle 6/7 border was significantly increased in both $T1^{EY}/T1^{2.1}$ and $T1^{EY}/Df$ compared with that in controls (Fig. 5E). This Vkg-GFP loss phenotype was completely restored by overexpression of *dC1GalT1* with a ubiquitous Gal4 driver (*Act5C-Gal4*) in the $T1^{EY}/T1^{2.1}$ background (vkg^{G454}, $dC1GalT1^{EY13370}/dC1GalT1^{2.1}$, *Act5c-Gal4*; *UAS-dC1GalT1/+*; Fig. 5C–E). These data clearly showed that the loss of mucin-type *O*-glycans led to the partial absence of Vkg-GFP at the muscle 6/7 border.
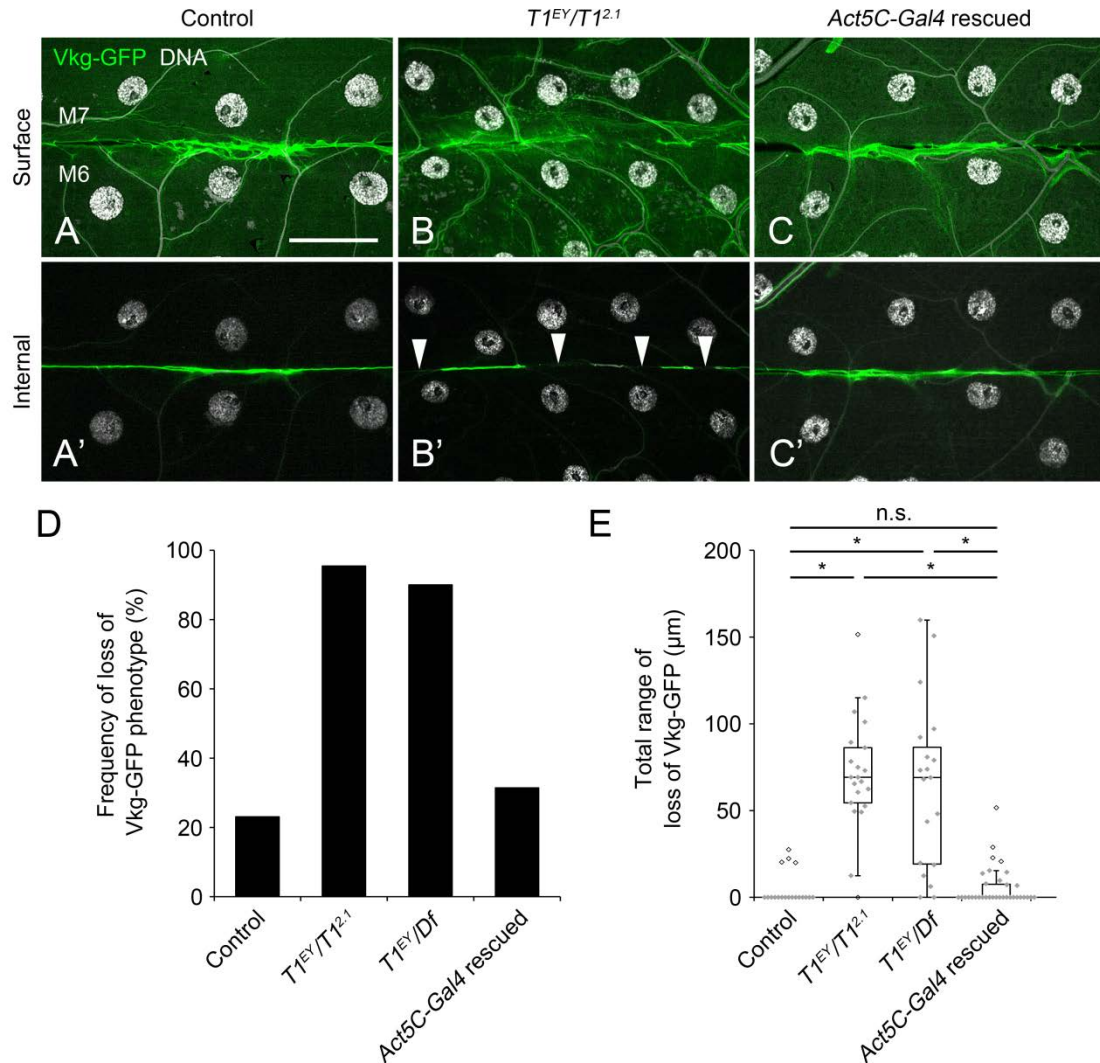
Fig. 5. Partial absence of collagen IV at the muscle 6/7 border in *dC1GalT1* mutants.
(A–C′) Confocal images of basement membranes (BMs) on muscle 6 (M6) and muscle 7 (M7) at abdominal segment 3 in control (*vkg*^{G454}/+) (A and A′), *T1*^{EY}/*T1*$^{2.1}$ (*vkg*^{G454}, *dC1GalT1*^{EY13370}/*dC1GalT1*$^{2.1}$) (B and B′)**,** and *Act5C-Gal4* rescued (*vkg*^{G454}, *dC1GalT1*^{EY13370}/*dC1GalT1*$^{2.1}$, *Act5C-Gal4*; *UAS-dC1GalT1*/+) (C and C′) third instar larvae. Surface sectional views of the two muscles are presented in A–C. Internal sectional views of the two muscles are presented in A′–C′. BMs and cell nuclei (DNA) were stained with Vkg-GFP and Hoechst 33342, respectively. Arrowheads in B′ indicate partial absence of Vkg-GFP at the muscle 6/7 border. Scale bar: 50 µm.
(D) Frequency of Vkg-GFP loss phenotype in control (*n* = 39), *T1*^{EY}/*T1*$^{2.1}$ (*n* = 44), *T1*^{EY}/*Df* (*vkg*^{G454}, *dC1GalT1*^{EY13370}/*Df(2L)Exel7040*) (*n* = 20), and *Act5C-Gal4* rescued (*n* = 35) larvae.
(E) Total range of Vkg-GFP loss at the muscle 6/7 border in control (*n* = 19), *T1*^{EY}/*T1*$^{2.1}$ (*n* = 21), *T1*^{EY}/*Df* (*n* = 19), and *Act5C-Gal4* rescued (*n* = 35) larvae. Data are the mean ± standard deviation for each genotype. Statistical significance was assessed by Steel-Dwass test. *P < 0.01, n.s.: not significant.

3-3. A subunit of collagen IV (Viking) does not carry T antigen

We hypothesized that Vkg beard T antigen, and the absence of T antigen on Vkg caused Vkg loss phenotype in the *dC1GalT1* mutants. To test this hypothesis, we carried out immunoprecipitation of Vkg-GFP by using an anti-GFP antibody and PNA lectin blotting (Fig. 6A). As a previous study showed that most of Vkg-GFP was produced in fat body and secreted into body fluid in larva (Pastor-Pareja and Xu, 2011), we used the proteins come from the body fluid of *vkg*^{G454}/+ larvae for the immunoprecipitation. In the fractions of immunoprecipitation, whereas a band corresponding to Vkg-GFP was recognized by the

16

anti-GFP antibody, the band was not recognized by PNA. Thus, this result suggested that Vkg-GFP was not modified by T antigen. In addition, we also performed PNA precipitation and immunoblotting by using the anti-GFP antibody (Fig. 6B). Contrary to our expectation, in the fractions of PNA precipitation, a band corresponding to Vkg-GFP was recognized by the anti-GFP antibody but not by PNA, indicating that Vkg-GFP could be co-immunoprecipitated with other proteins modified by T antigen. Therefore, these data showed that Col IV did not carry T antigen, and hypoglycosylation of Col IV could not cause Col IV-deficiency phenotype.
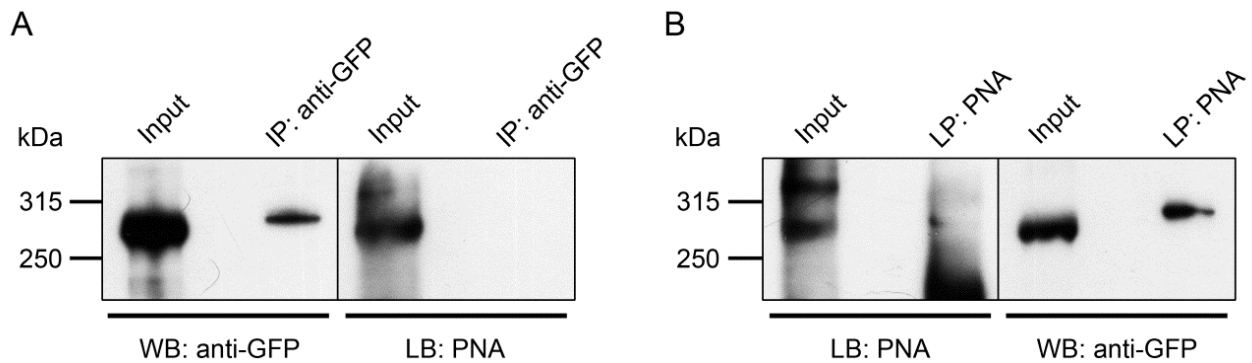

Fig. 6. Immunoprecipitation and lectin precipitation of Vkg-GFP come from larval body fluid.
(A) Vkg-GFP come from body fluid of $vkg^{G454}/+$ third-instar larvae was immunoprecipitated with an anti-GFP antibody. Western blotting (WB) by using the anti-GFP antibody (left panel) and PNA lectin blotting (LB) (right panel) were carried out. IP means immunoprecipitation.
(B) Proteins come from body fluid of $vkg^{G454}/+$ third-instar larvae were precipitated with PNA. PNA LB (left panel) and WB by using the anti-GFP antibody (right panel) were carried out. LP means lectin precipitation.

3-4. dC1GalT1 mutants displayed the ectopic bouton localization at the muscle 6/7 border

We also found morphological defects of NMJs in *dC1GalT1* mutant larvae. Although many boutons were localized away from the border between muscles 6 and 7 in the controls (brackets in Fig. 7A), many boutons were localized at the muscle 6/7 border in the *dC1GalT1* mutant larvae (white arrowheads in Fig. 7B). We measured distance from each bouton to the muscle 6/7 border in each genotype. This distance in the two *dC1GalT1* mutants tended to be shorter than that in WT larvae (Fig. 7D). Moreover, the frequency of boutons positioned at the muscle 6/7 border (number of boutons positioned at the muscle 6/7 border per total bouton number) was significantly higher in the two *dC1GalT1* mutants compared with that in WT larvae (Fig. 7E). This percentage was completely restored in *Act5C-Gal4* rescued larvae (Fig. 7C and E). In addition, while the total number of boutons in the two *dC1GalT1* mutants did not differ from that in WT larvae (Fig. 7F), the total number of branches was significantly lower in the two *dC1GalT1* mutants compared with that in WT larvae (Fig. 7G). Reduced number of NMJ branches was suppressed in *Act5C-Gal4* rescued larvae (Fig. 7G). Therefore, these results showed that absence of mucin-type *O*-glycans led to the mislocalization of NMJ boutons and reduced number of NMJ branches on muscle 6/7.
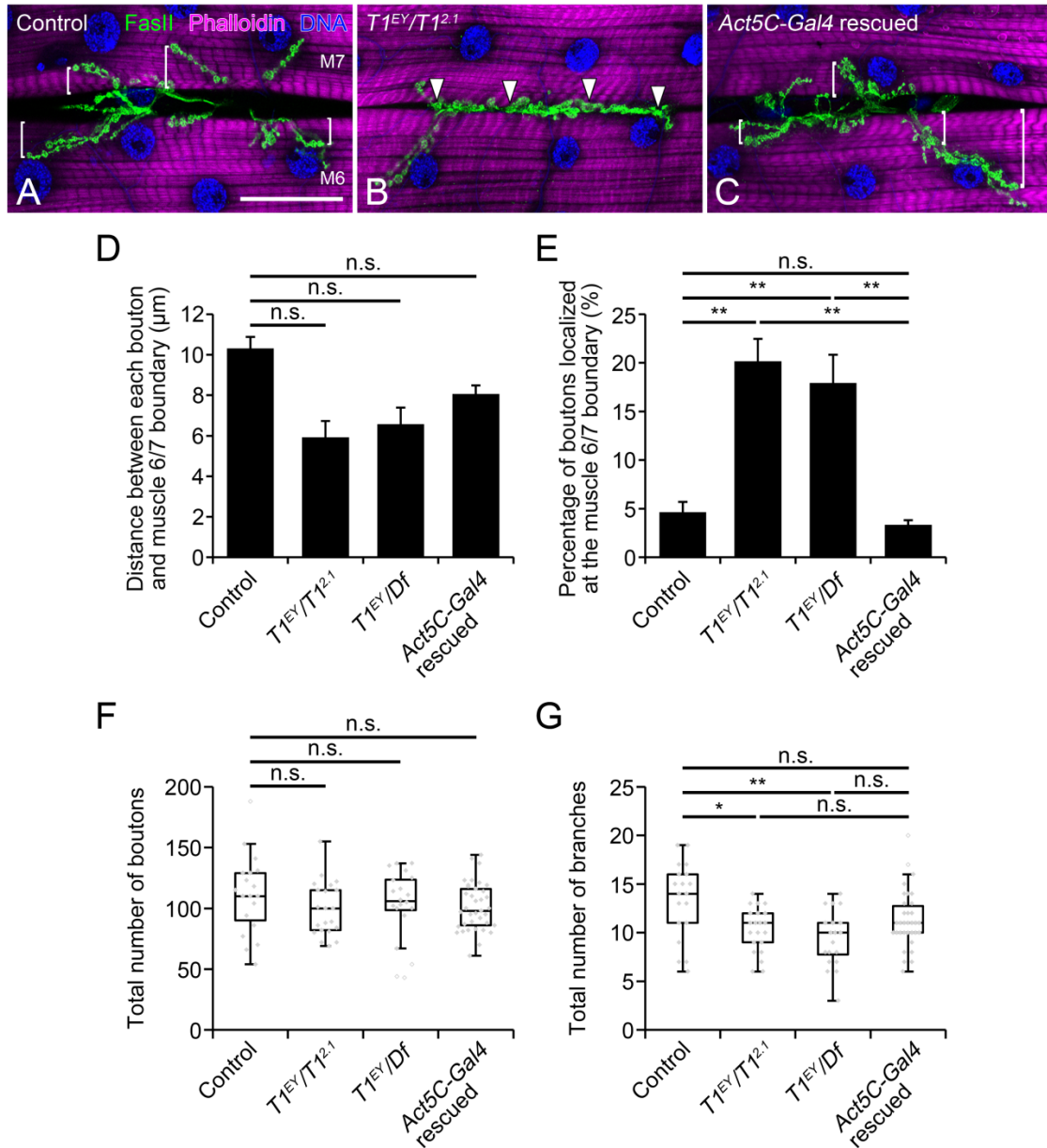
Fig. 7. Ectopic bouton localization at the muscle 6/7 border in *dC1GalT1* mutants.
(A–C) Confocal images of NMJs on muscle 6 (M6) and muscle 7 (M7) at abdominal segment 3 in control (vkg^{G454}/+) (A), $T1^{EY}/T1^{2.1}$ (vkg^{G454}, $dC1GalT1^{EY13370}/dC1GalT1^{2.1}$) (B), and *Act5C-Gal4* rescued (vkg^{G454}, $dC1GalT1^{EY13370}/dC1GalT1^{2.1}$, *Act5C-Gal4*; *UAS-dC1GalT1*/+) (C) third instar larvae. Surface sectional views of the muscles are presented. NMJ boutons were labeled with an anti-fasciclin II (Fas II) antibody (a presynaptic bouton marker; green). Muscle fibers and cell nuclei (DNA) were labeled with phalloidin (magenta) and Hoechst 33342 (blue), respectively. Brackets in A and C show the distance between the bouton and muscle 6/7 border. Arrowheads in B indicate mispositioned NMJ boutons at the muscle 6/7 border. Scale bars: 50 µm (A–C).
(D) Distance between each bouton and muscle 6/7 border in control (n = 19), $T1^{EY}/T1^{2.1}$ (n = 21), $T1^{EY}/Df$ (vkg^{G454}, $dC1GalT1^{EY13370}/Df(2L)Exel7040$) ($n$ = 20), and *Act5C-Gal4* rescued (n = 36) larvae. Statistical significance was assessed by the Steel-Dwass test. n.s.: not significant.
(E) Percentage of boutons positioned at the muscle 6/7 border in control (n = 19), $T1^{EY}/T1^{2.1}$ (n = 21), $T1^{EY}/Df$ (n = 20), and *Act5C-Gal4* rescued (n = 36) larvae. Statistical significance was assessed by the Steel-Dwass test. **P < 0.01; n.s.: not significant.
(F) Total number of boutons in muscle 6/7 NMJs at abdominal segment 3 in control (n = 19), $T1^{EY}/T1^{2.1}$ (n = 21), $T1^{EY}/Df$ (n = 20), and *Act5C-Gal4* rescued (n = 37) larvae. Statistical significance was assessed by the Tukey-Kramer test. n.s.: not significant.
(G) Total number of branches in muscle 6/7 NMJs at abdominal segment 3 in control (n = 19), $T1^{EY}/T1^{2.1}$ (n = 21),
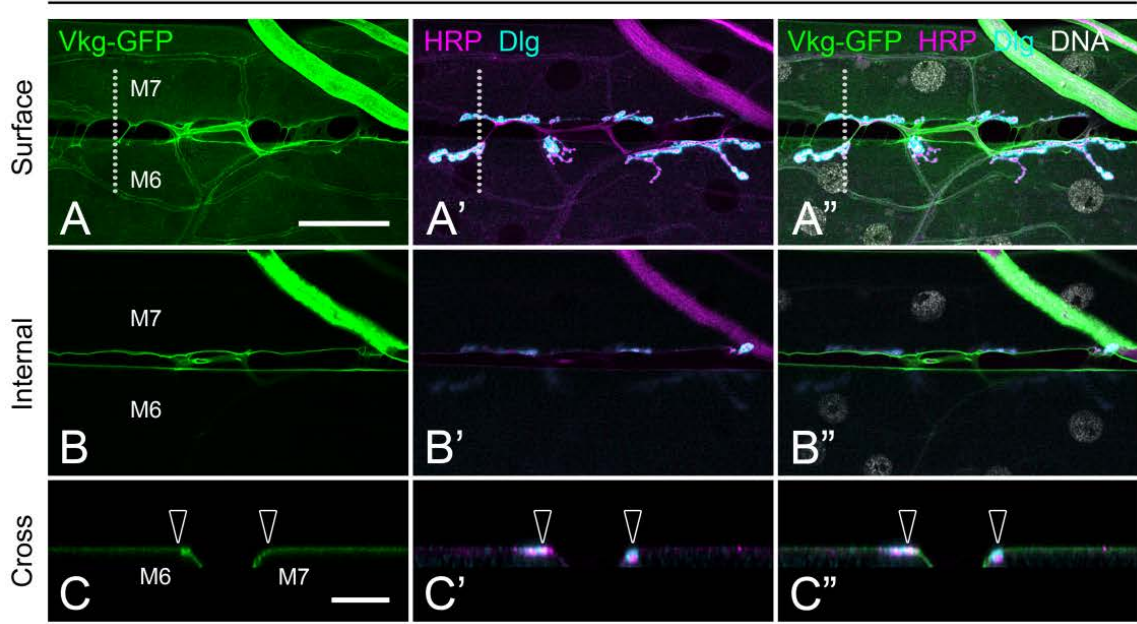
$T1^{EY}/Df$ ($n = 20$), and *Act5C-Gal4* rescued ($n = 34$) larvae. A branch was defined as a terminal neurite containing at least two boutons. Statistical significance was assessed by the Steel-Dwass test. *$P < 0.05$; **$P < 0.01$; n.s.: not significant.

3-5. Absence of basement membrane component was correlated with ectopic bouton localization in dC1GalT1 mutants
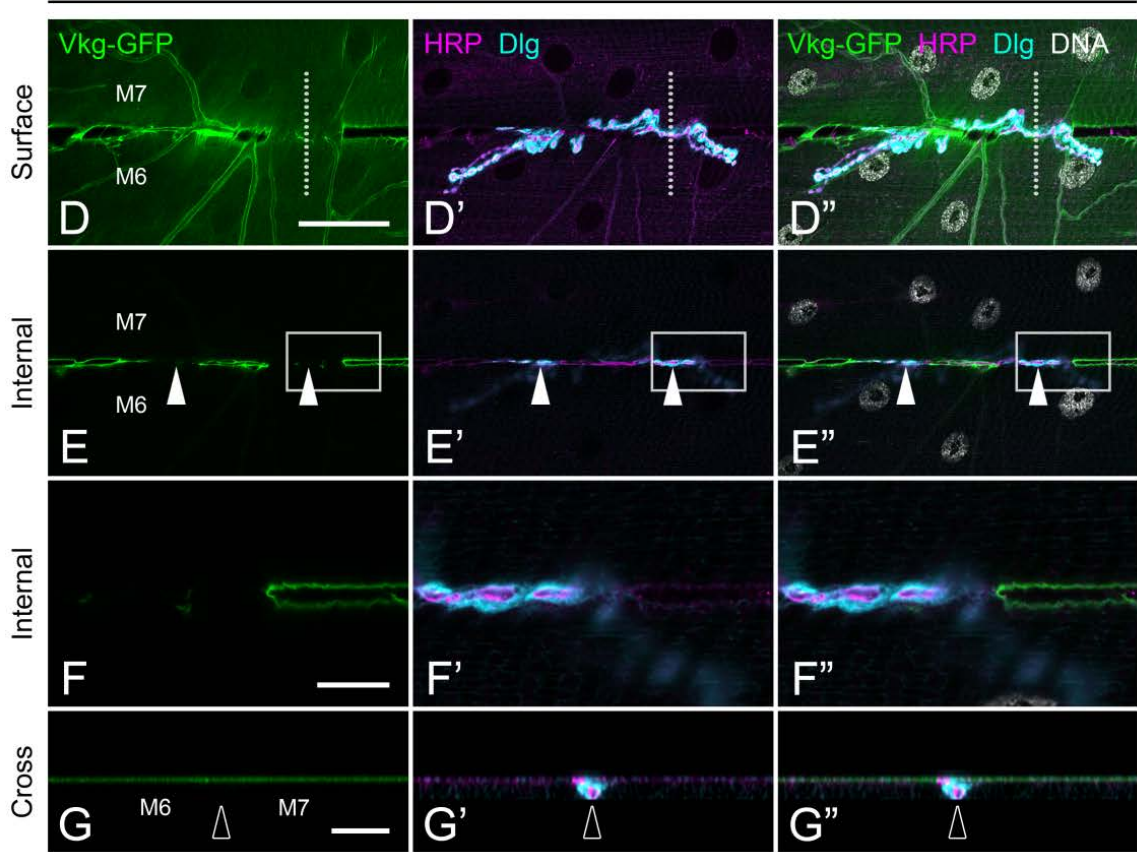
Next, to test whether there is relationship between the two phenotypes, i.e., the partial absence of Vkg-GFP and the ectopic bouton localization at the muscle 6/7 border, we examined the positional relationship between the sites devoid of Vkg-GFP and mispositioned NMJ boutons at the muscle 6/7 border in the *dC1GalT1* mutants (Fig. 8). As described above, in the surface sectional view of the muscles, although many boutons were distant from muscle 6/7 border in the controls (Fig. 8A–A″), many boutons were mispositioned at the muscle 6/7 border in the *dC1GalT1* mutant larvae (Fig. 8D–D″). In the internal sectional view of the muscles, whereas Vkg-GFP was expressed at the muscle 6/7 border in the controls (Fig. 8B), Vkg-GFP expression was partially lost at the muscle 6/7 border in the *dC1GalT1* mutant larvae (white arrowheads in Fig. 8E). In *dC1GalT1* mutants, some NMJ boutons were ectopically positioned at the site devoid of Vkg-GFP (Fig. 8E–F″). Moreover, some boutons were also positioned just above the site devoid of Vkg-GFP in the surface sectional view (Fig. 8D–E″). In the cross sectional view of the muscles, muscles 6 and 7 were individually covered with separate BMs, and NMJ boutons were positioned on muscle surfaces in controls (Fig. 8C–C″). In contrast, in the *dC1GalT1* mutants, the two muscles were covered with a continuous single BM (Fig. 8G–G″). Moreover, boutons were positioned at the muscle 6/7 border (black arrowheads in Fig. 8G–G″). These data indicated that the two muscles may be connected through the mispositioned boutons at the muscle 6/7 border in the *dC1GalT1* mutants.

We found that there was a correlation between the total range of Vkg-GFP loss and the frequency of boutons positioned at the muscle 6/7 border in the two *dC1GalT1* mutants (Fig. 8H), showing that the two phenotypes, i.e., the partial absence of Vkg-GFP and the ectopic localization of NMJ boutons, were directly linked. Furthermore, to verify that NMJ boutons tend to be positioned *at* or *just above* the site devoid of Vkg-GFP in the *dC1GalT1* mutants, we compared the frequency of boutons positioned *at* or *just above* the site devoid of Vkg-GFP vs. the frequency of boutons positioned *at* or *just above* VKg-GFP positive site at the muscle 6/7 border in the two *dC1GalT1* mutants (Fig. 8I). In both mutants, the former was significantly higher than the latter, clearly showing that NMJ boutons were preferentially positioned *at* or *just above* the site devoid of Vkg-GFP at the muscle 6/7 border in the *dC1GalT1* mutants. These results showed that the absence of mucin-type *O*-glycan made NMJ boutons localize *at* or *just above* the site devoid of Col IV at the muscle 6/7 border.

Control

Vkg-GFP | M7 | M6 | A | HRP Dlg | A' | Vkg-GFP HRP Dlg DNA | A''

M7 | M6 | B | B' | B''

M6 | M7 | C | M6 | M7 | C' | C''

T1^{EY}/ T1^{2.1}

Vkg-GFP | M7 | M6 | D | HRP Dlg | D' | Vkg-GFP HRP Dlg DNA | D''

M7 | M6 | E | E' | E''

F | F' | F''

M6 | M7 | G | G' | G''

20

H

$T1^{EY}/T1^{2.1}$ $T1^{EY}/Df$

Percentage of boutons localized at the muscle 6/7 boundary (%)

Total range of loss of Vkg (µm)

I

$T1^{EY}/T1^{2.1}$ $T1^{EY}/Df$

(i) Number of boutons localized *at* or *just above* the site devoid of Vkg /Total range of loss of Vkg (µm^{-1})

(ii) Number of boutons localized *at* or *just above* Vkg positive site /Total range of Vkg positive site (µm^{-1})
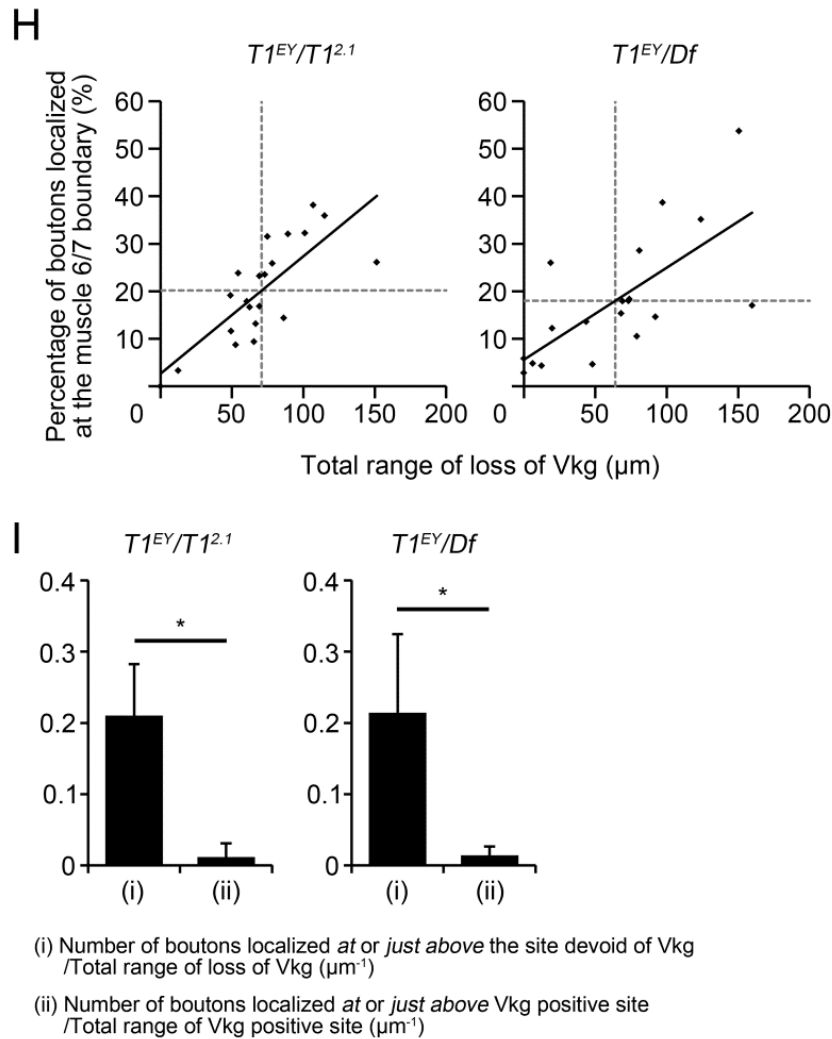
Fig. 8. Correlation between collagen IV loss and bouton mislocalization at the muscle 6/7 border in *dC1GalT1* mutants.
(A–G″) Confocal images of BMs and NMJ boutons on muscle 6 (M6) and muscle 7 (M7) at abdominal segment 3 in control ($vkg^{G454}/+$) (A–C″) and $T1^{EY}/T1^{2.1}$ (vkg^{G454}, $dC1GalT1^{EY13370}/dC1GalT1^{2.1}$) (D–G″) third instar larvae. Surface sectional views of the muscles are presented in A–A″ and D–D″. Internal sectional views of the muscles are presented in B–B″, E–E″, and F–F″. High-magnification views of the area bordered by a rectangle are presented in E–E″ (F–F″). Cross-sectional views of the area within the white dotted-line are presented in A–A″ and D–D″ (C–C″ and G–G″). BMs were labeled with Vkg-GFP. NMJ boutons were stained with anti-HRP antibody (a presynaptic marker) and anti-Dlg antibody (a postsynaptic marker). Cell nuclei (DNA) were labeled with Hoechst 33342. Closed arrowheads in E–E″ indicate partial absence of Vkg-GFP and mispositioned NMJ boutons, respectively. Open arrowheads in C–C″ and G–G″ show positions of NMJ boutons. Scale bars: 50 µm (A and D) and 10 µm (C, F, and G).
(H) Correlation between the total range of Vkg-GFP loss and the percentage of boutons positioned at the muscle 6/7 border in $T1^{EY}/T1^{2.1}$ (n = 21; left) and $T1^{EY}/Df$ (vkg^{G454}, $dC1GalT1^{EY13370}/Df(2L)Exel7040$) (n = 19; right) larvae. Values of the Pearson's correlation coefficient r comprised 0.77 and 0.70 for $T1^{EY}/T1^{2.1}$ and $T1^{EY}/Df$, respectively. Black straight line indicates the approximate line. Gray cross-dotted-lines indicate the average lines.
(I) A comparison between 'the frequency of boutons positioned *at* or *just above* the site devoid of Vkg-GFP at the muscle 6/7 border' vs. 'the frequency of boutons positioned *at* or *just above* Vkg-GFP positive site at the muscle 6/7 border' in $T1^{EY}/T1^{2.1}$ (n ≥ 20; left) and $T1^{EY}/Df$ (n ≥ 17; right) larvae. Statistical significance was assessed by the Student's *t*-test. *$P < 0.001$.

3-6. Ultrastructural analysis of mispositioned NMJ boutons in dC1GalT1 mutants

To observe in detail mispositioned NMJ boutons in *dC1GalT1* mutants, we performed ultrastructural analysis by ASEM and TEM. ASEM permitted the wet tissues to be observed at atmospheric pressure after

21

staining with heavy metals (Nishiyama et al., 2010; Memtily et al., 2015). Many NMJ boutons were observed apart from the muscle 6/7 border in the WT larvae (Fig. 9A and A′). In contrast, in *dC1GalT1* mutants, NMJ boutons were observed at the muscle 6/7 border (Fig. 9B and arrowhead in Fig. 9B′) as well as near the border (Fig. 9B and arrow in Fig. 9B′).

We then observed the mispositioned NMJ boutons by TEM. No NMJ bouton was observed in the muscle 6/7 cleft in WT larvae (Fig. 9C and C′). However, in *dC1GalT1* mutants, some NMJ boutons were observed in the muscle 6/7 cleft and connected the two muscles (Fig. 9D and D′). Therefore, these results clearly showed that mucin-type *O*-glycans were required for the positioning of NMJ boutons.
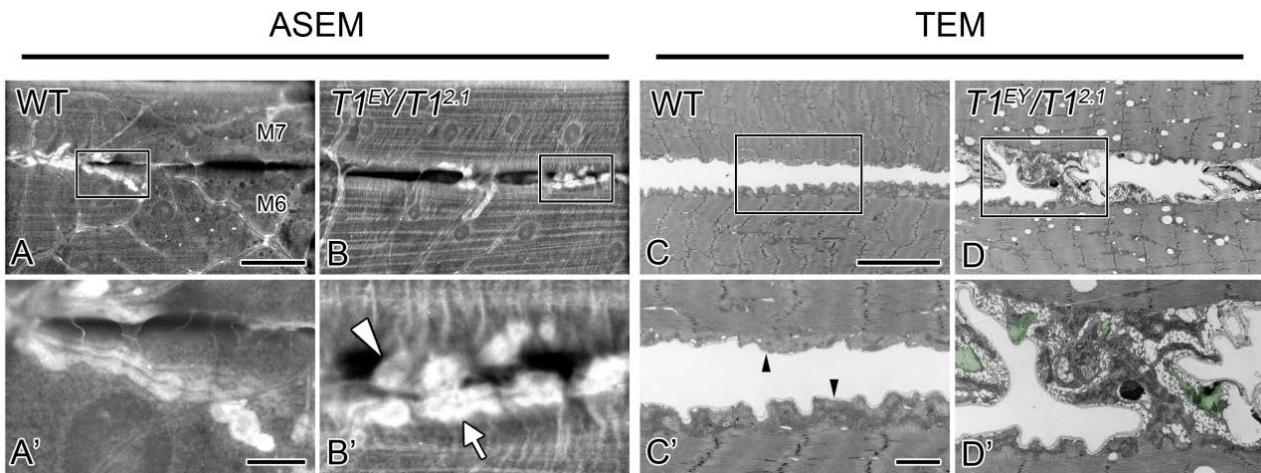

Fig. 9. Ultrastructure of the muscle 6/7 border in *dC1GalT1* mutants.
(A–B′) Atmospheric scanning electron microscopy (ASEM) observation of NMJs on muscle 6 (M6) and muscle 7 (M7) in wild-type (WT) (A and A′) and *T1^EY^/T1^2.1^* (*dC1GalT1^EY13370^/dC1GalT1^2.1^*) (B and B′) third instar larvae. Low-magnification images of the muscle 6/7 border are presented (A and B). High-magnification views of the area bordered by a rectangle are presented in A and B (A′ and B′). Wet muscle tissues were directly observed through SiN film. The arrowhead in B′ shows a mispositioned NMJ bouton at the muscle 6/7 border. The arrow in B′ shows a NMJ bouton near the muscle 6/7 border. Scale bars: 50 μm (A and B) and 10 μm (A′ and B′).
(C–D′) Transmission electron micrographs of the muscle 6/7 border in WT (C and C′) and *T1^EY^/T1^2.1^* (D and D′) third instar larvae. Low-magnification images of the muscle 6/7 border are presented (C and D). High-magnification views of the area bordered by a rectangle are presented in C and D (C′ and D′). Arrowheads in C′ indicate BMs on the surfaces of the two muscles. The presynaptic areas are indicated in green in D′. Scale bars: 10 μm (C and D) and 2 μm (C′ and D′).

3-7. dGlcAT-P is predominant glucuronyltransferase synthesizing glucuronylated core 1 glycan

In *Drosophila*, glucuronylated core 1 glycan (Fig. 10A) has been found in S2 cells, embryos, and larvae (Aoki et al., 2008; Breloy et al., 2008). As mentioned above, three dGlcATs, i.e., dGlcAT-I, dGlcAT-P, and dGlcAT-S have been identified previously in *Drosophila* (Kim et al., 2003). In that paper, enzymatic activities of each dGlcAT toward core 1 glycan were determined. However, their specific activities were not measured. As dGlcAT-I, dGlcAT-P, and dGlcAT-S enzymes have one, two, and four splicing variants, respectively (Table 4), we prepared FLAG-tagged proteins of each dGlcAT splicing variant and determined their specific activities toward core 1 glycan (Galβ1-3GalNAcα1-*p*NP substrate). As dGlcAT-S-PA was considered to be functionless as a glycosyltransferase due to the absence of a transmembrane domain, the specific activity of this splicing variant were not measured. FLAG-dGlcAT-P-II had strong activity, while FLAG-dGlcAT-S-I had poor activity (Fig. 10B). However, FLAG-dGlcAT-S-III (-PC) hardly showed the

activity, and FLAG-dGlcAT-I, FLAG-dGlcAT-P-I, and FLAG-dGlcAT-S-II (-PB) showed no activity.

Next, we determined the glycan structure of enzymatic reaction products derived from the incubation of dGlcAT-P-II with core 1 glycan (Galβ1-3GalNAcα1-pNP substrate) using NSI-MS. Permethylated malto-series oligosaccharide standards (Dp3 and Dp4 permethylated with ^{13}C-MeI) were spiked into the reaction samples before infusion for the quantification of the enzymatic products. MS analysis showed that enzymatic reactions catalyzed by dGlcAT-P-II synthesized glucuronylated core 1 glycan (m/z 725) from the starting material (m/z 527) (Fig. 10C). To determine the position of GlcA added onto core 1 glycan, dGlcAT-P-II enzymatic products were permethylated and analyzed by NSI-MS^n multi-dimensional fragmentation (Aoki et al., 2007, 2008). CID fragmentation of permethylated glucuronylated core 1 glycan (m/z 844) showed position-specific carbohydrate ring-cleavage fragment ions at m/z 329, 359, and 373, consistent with the presence of a terminal GlcA attached to position 3 of Gal residue (Fig. 10D). Thus, this data showed that dGlcAT-P-II preferentially added GlcA to position 3 of the terminal Gal residue of core 1 glycan. Therefore, the glycan structure of enzymatic products synthesized by dGlcAT-P-II was identified as GlcA1-3Galβ1-3GalNAcα1-pNP. Fragment ions that would show the synthesis of a branched form of glucuronylated core 1 glycan, Galβ1-3(GlcA1-4)GalNAcα1-pNP (Aoki et al., 2008), were not detected in the dGlcAT-P-II enzymatic products (Fig. 10D). Together, these data clearly showed that GlcA transferase activity of dGlcAT-P-II was much higher than those of other dGlcATs, and dGlcAT-P-II synthesized glucuronylated core 1 glycan (GlcA1-3Galβ1-3GalNAc).

In order to analyze the expression levels of *dGlcAT-P-RB*, *-RC*, and *-RE* transcripts, which are translated into dGlcAT-P-II protein (Table 4), at various developmental stages and in different tissues, we carried out quantitative real-time PCR analysis (Fig. 10E). Total transcripts of *dGlcAT-P-RB*, *-RC*, and *-RE* were expressed ubiquitously. However, they were insufficiently expressed at the latest stage of embryogenesis (embryo 18–24h) and in the third-instar larval fat body, whereas they were highly expressed in the adult female body. Therefore, these results indicated that glucuronylated core 1 glycan produced by dGlcAT-P-II was expressed and worked in various developmental stages and multiple tissues.
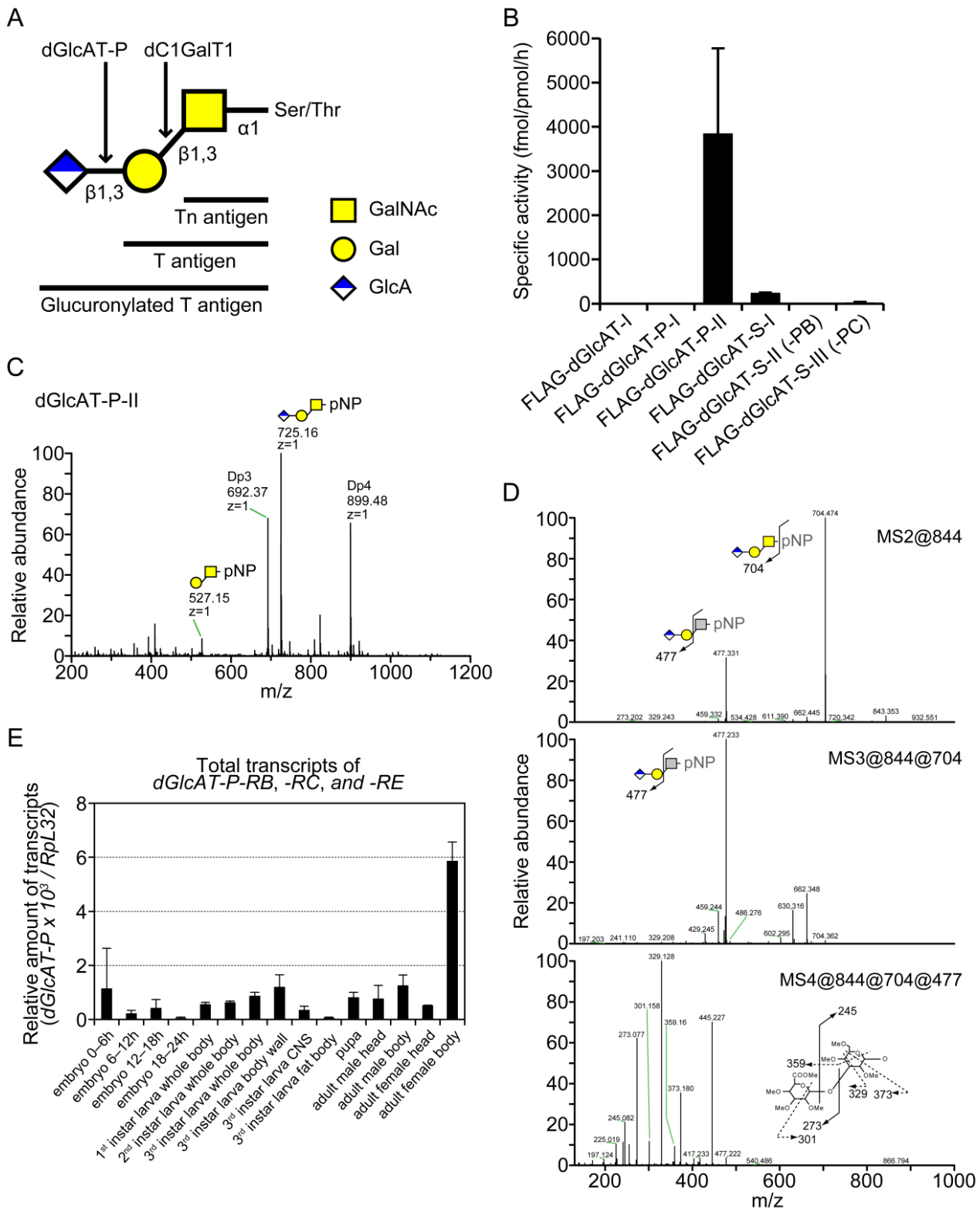
Fig. 10. Glucuronylation of core 1 glycan by dGlcAT-P.

(A) The glycan structure of Tn antigen, T antigen, and glucuronylated T antigen. To synthesize T antigen, dC1GalT1 adds Gal in a β1,3-linkage to GalNAc of Tn antigen. To synthesize glucuronylated T antigen, *Drosophila* β1,3-glucuronyltransferase-P (dGlcAT-P) adds Glucuronic acid (GlcA) in a β1,3-linkage to Gal of T antigen.

(B) GlcA transferase activities of each FLAG-tagged dGlcAT splicing variants toward T antigen (Galβ1-3GalNAcα1-*p*NP substrate). Data are indicated as the mean ± standard deviation of three independent experiments.

(C) T antigen (Galβ1-3GalNAcα1-*p*NP substrate) was reacted with UDP-GlcA and dGlcAT-P-II enzyme, and glycan

24

structure of the enzymatic products was analyzed by nanospray ionization-mass spectrometry (NSI-MS). T antigen was detected at m/z 527.15, and glucuronylated T antigen was detected at m/z 725.16. Maltooligosaccharides (Dp3 and Dp4) were used as reference standards (Dp3: m/z 692.37 and Dp4: 899.48).

(D) T antigen (Galβ1-3GalNAcα1-pNP substrate) was reacted with UDP-GlcA and dGlcAT-P-II enzyme, and the glycan structure of the enzymatic products was determined by NSI-MS following permethylation of the products. The sodiated ion detected at m/z 844 was subjected to MS^n analysis and the fragmentation pattern shows that terminal GlcA was attached at the position 3 of Gal residue.

(E) Quantitative real-time PCR analysis of total transcripts of *dGlcAT-P-RB*, *dGlcAT-P-RC*, and *dGlcAT-P-RE*, which are translated into the dGlcAT-P-II protein, at various developmental stages and in different tissues of wild-types. The actual amounts of total transcripts of *dGlcAT-P-RB*, *-RC*, and *-RE* were divided by that of the *RpL32* transcript for normalization. The measurements were evaluated by absolute quantification using standard constructs in known concentration.

Table 4. Splicing variants of three *dGlcATs*.

Gene	CG number	Splicing variant				Prepared FLAG-tagged protein[1]	Source	
		mRNA		Protein				
dGlcAT-I	CG32775	RA		PA		29th–306th aa	FlyBase	
dGlcAT-P	CG6207	RA		PA	I^{*2}	80th–479th aa	FlyBase	
		RD		PD				
		RB		PB	II^{*2}	68th–316th aa		
		RC		PC				
		RE		PE				
dGlcAT-S	CG3881	I		I		81st–275th aa	DDBJ (LC146674)	
		II	RB	II	PB	81st–409th aa	DDBJ (LC146675)	FlyBase
		III^{*3}	RC	III^{*3}	PC	81st–486th aa	FlyBase	
		RA		PA		-	FlyBase	

[1] FLAG-tagged protein which was used for the determination of specific activity toward the Galβ1-3GalNAcα1-pNP substrate in this study.

[2] In this study, dGlcAT-P-PA and -PD are named as "dGlcAT-P-I" because their amino acid sequences are absolutely identical. For the same reason, dGlcAT-P-PB, -PC, and -PE are named as "dGlcAT-P-II".

[3] In this study, *dGlcAT-S-RC* and -PC are designated as "dGlcAT-S-III".

3-8. Expression level of T antigen was upregulated in the muscles and neuromuscular junctions of dGlcAT-P mutants

To clarify the physiological roles of glucuronylated T antigen, we newly produced two *dGlcAT-P* mutant alleles, *dGlcAT-P^{SK1}* and *dGlcAT-P^{SK6}*, using the CRISPR/Cas9 system (Kondo and Ueda, 2013). In *dGlcAT-P^{SK1}* allele, 4 bases were inserted into the coding region, and frameshifts took place from the 61st to the 91st amino acid residues of dGlcAT-P-I protein and from the 61st to the 178th amino acid residues of dGlcAT-P-II protein (Fig. 11A and Table 5). In *dGlcAT-P^{SK6}* allele, 10 bases were deleted from the coding region, and frameshifts took place from the 60th to the 83rd amino acid residues of dGlcAT-P-I protein and from the 60th to the 68th amino acid residues of dGlcAT-P-II protein. All the products derived from *dGlcAT-P^{SK1}* and *dGlcAT-P^{SK6}* alleles never contain the catalytic domain of the enzyme. To exclude the effects of potential secondary site mutations, we used *Df(3L)BSC817*, a chromosomal deficiency, in which the *dGlcAT-P* gene is deleted completely, and analyzed *dGlcAT-P^{SK1}/Df(3L)BSC817* and

dGlcAT-P^{SK6}/Df(3L)BSC817 as *dGlcAT-P* mutants. To confirm that normal dGlcAT-P enzyme is not expressed in both *dGlcAT-P* mutants, we carried out immunoblotting by using an anti-dGlcAT-P antibody. This antibody is able to detect two splicing variants, dGlcAT-P-I (52.6 kDa) and dGlcAT-P-II (35.8 kDa) (Table 5). Additionally, because the antibody can recognize only the C-terminal domain of both dGlcAT-P-I and dGlcAT-P-II, it never recognized *dGlcAT-P^{SK1}* and *dGlcAT-P^{SK6}* products. A band corresponding to dGlcAT-P-I in WT samples was not detected owing to the detection of non-specific bands around 50 kDa (data not shown). However, although a band corresponding to dGlcAT-P-II (35 kDa) was detected in WT, it was not detected in both *dGlcAT-P* mutant samples (Fig. 11B), demonstrating that normal dGlcAT-P-II protein was never expressed in those mutant larvae. Because T antigen is glucuronylated by dGlcAT-P-II but not by dGlcAT-P-I (Fig. 10), T antigen must not be glucuronylated in both *dGlcAT-P* mutants. Moreover, the extended VNC phenotype was observed in these two mutant larvae (data not shown), similar to that described previously (Pandey et al., 2011). These findings revealed that the two *dGlcAT-P* mutants were null mutants.

To test whether the expression level of glucuronylated T antigen was reduced in the two *dGlcAT-P* null mutants, we carried out lectin blotting and staining using PNA that can bind the T antigen but not the glucuronylated T antigen. T antigen expression was notably increased in the *dGlcAT-P* mutant muscles (Fig. 11C and D), showing that T antigen is also glucuronylated by dGlcAT-P *in vivo*. We also found that on the muscle surface, T antigen expression in the two *dGlcAT-P* null mutants was much higher than that in WT larvae (Fig. 11E–G and K). Moreover, T antigen expression on the muscle surface disappeared in *dC1GalT1* and *dGlcAT-P* double mutants (Fig. 11M–O), demonstrating that the increased unmodified T antigen on the muscle surface of *dGlcAT-P* null mutants was really produced by dC1GalT1. Thus, the depletion of dGlcAT-P resulted in increased expression of non-glucuronylated T antigen on the muscle surface due to the suppression of T antigen glucuronylation. We next examined the expression level of T antigen at larval NMJs. To label presynaptic NMJ boutons, an anti-HRP antibody was used (Fig. 11H–J). At the NMJs, T antigen expression in the two *dGlcAT-P* null mutants was significantly higher than that in WT larvae (Fig. 11H–J″ and L). Therefore, these data clearly showed that dGlcAT-P synthesized glucuronylated T antigen localized on the muscle surface and at the NMJs.
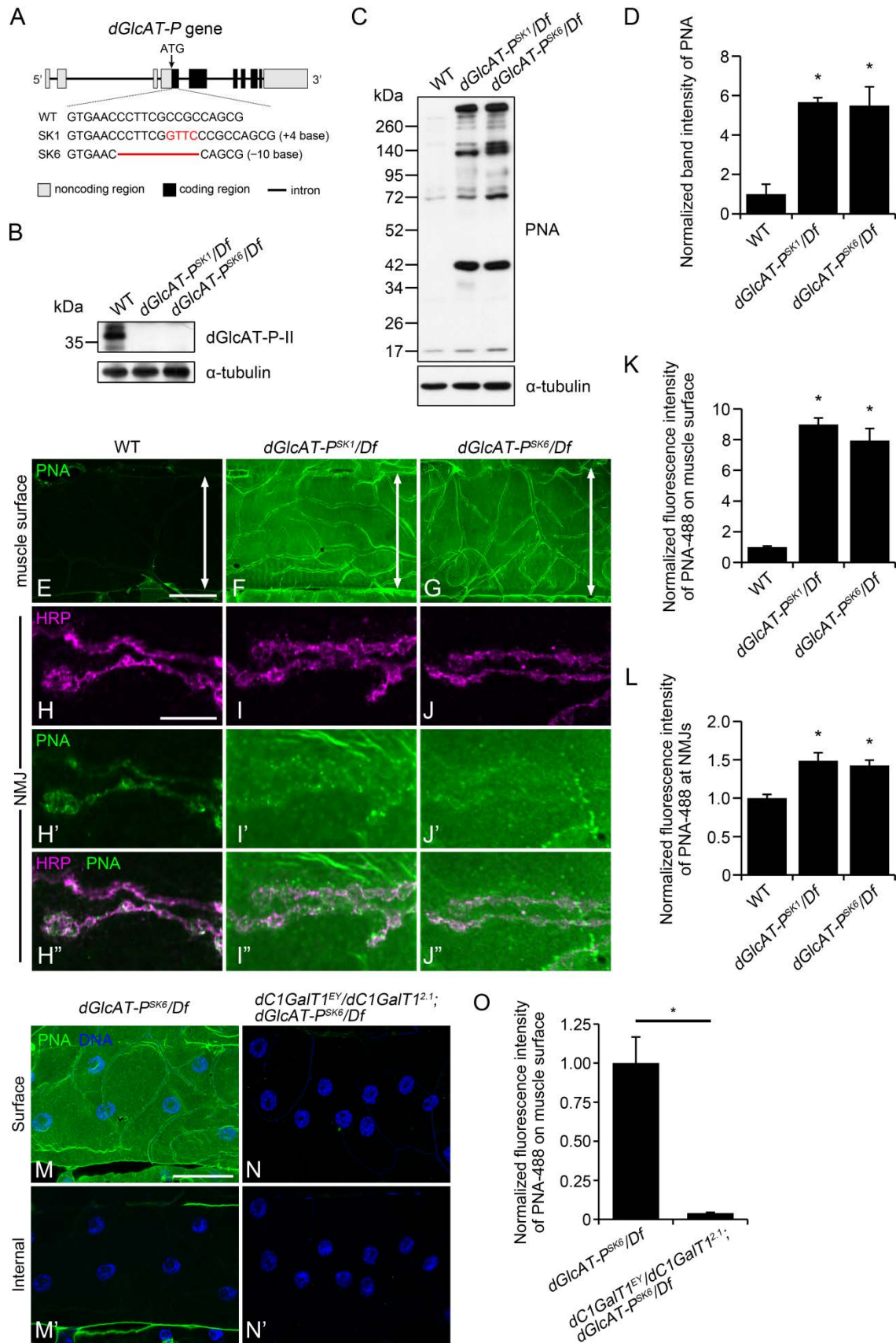
Fig. 11. Increase expression of T antigen in the muscles and neuromuscular junctions in *dGlcAT-P* mutants.
(**A**) Two *dGlcAT-P* mutant alleles (*dGlcAT-P^SK1^* and *dGlcAT-P^SK6^*) are shown. *dGlcAT-P^SK1^* is a 4-base insertion mutant allele, while *dGlcAT-P^SK6^* is a 10-base deletion mutant allele. These two alleles were produced by the CRISPR/Cas9

system. Gray and black boxes show noncoding and coding regions, respectively.

(**B**) Immunoblotting of entire bodies of wild-type (WT), *dGlcAT-P^{SK1}/Df,* and *dGlcAT-P^{SK6}/Df* third-instar larvae using an anti-dGlcAT-P antibody (upper). α-tubulin internal control (lower).

(**C**) Lectin blotting of larval body wall muscles of WT, *dGlcAT-P^{SK1}/Df,* and *dGlcAT-P^{SK6}/Df* third-instar larvae using peanut agglutinin (PNA) (upper). α-tubulin internal control (lower). Experiments were repeated independently three times. A representative example is indicated.

(**D**) Relative band intensity of PNA normalized by band intensity of α-tubulin. Data are presented as the mean ± standard error of the mean for each genotype ($n = 3$). Statistical significance was evaluated by Dunnett test. *$P < 0.01$.

(**E–G**) Representative confocal microscopic images of muscle 6 at abdominal segment 3 in WT (E), *dGlcAT-P^{SK1}/Df* (F), and *dGlcAT-P^{SK6}/Df* (G) third-instar larvae. Surface sectional views of the muscles are indicated. The width of muscle 6 is shown by a double-headed arrow. T antigen was stained with Alexa Fluor-488-conjugated PNA (PNA-488; green) without permeabilization. Tubule like-structures are shape of tracheae on muscle surface. Scale bar: 50 μm.

(**H–J″**) Representative confocal microscopic images of neuromuscular junctions (NMJs) on muscle 6 at abdominal segment 3 in WT (H–H″), *dGlcAT-P^{SK1}/Df* (I–I″), and *dGlcAT-P^{SK6}/Df* (J–J″) third-instar larvae. NMJs were stained with an anti-HRP antibody (a presynaptic bouton marker; magenta) and PNA-488 (green) without permeabilization. Scale bar: 10 μm.

(**K and L**) Relative fluorescence intensities of PNA-488 on the muscle surface (K) and at NMJs (L) normalized to the average of the WT data. Data are presented as the mean ± standard error of the mean for each genotype ($n = 8$–10). Statistical significance was evaluated by Dunnett test. *$P < 0.01$.

(**M–N′**) Representative confocal microscopic images of muscle 6 at abdominal segment 3 in *dGlcAT-P* mutant (*dGlcAT-P^{SK6}/Df*) (M and M′) and *dC1GalT1* and *dGlcAT-P* double mutant (*dC1GalT1^{EY}/dC1GalT1^{2.1}; dGlcAT-P^{SK6}/Df*) (N and N′) third-instar larvae. Surface sectional views of the muscle are shown in M and N. Internal sectional views of the muscle are shown in M′ and N′. T antigen and cell nuclei were labeled with PNA-488 (green) and Hoechst 33342 (blue), respectively, without permeabilization. Scale bar: 50 μm.

(**O**) Relative fluorescence intensities of PNA-488 on the muscle surface normalized to the average of the *dGlcAT-P* mutant data. Data are presented as the mean ± standard error of the mean for each genotype ($n = 12$–14). Statistical significance was evaluated by the Student's *t*-test. *$P < 0.001$.

Table 5. Details about mutant proteins in *dGlcAT-P^{SK1}* and *dGlcAT-P^{SK6}* alleles.

Allele	Splicing variant	Start point of frameshifts	Stop codon	Product	
				Amino acid	MW (kDa)
WT		-	480th	479	52.6
dGlcAT-P^{SK1}	dGlcAT-P-I	61st	92nd	91	10.1
dGlcAT-P^{SK6}		60th	84th	83	9.2
WT		-	317th	316	35.8
dGlcAT-P^{SK1}	dGlcAT-P-II	61st	179th	178	19.1
dGlcAT-P^{SK6}		60th	69th	68	7.5

3-9. dGlcAT-P mutants showed an absence of basement membrane components at the muscle 6/7 border

As described above, a partial absence of Col IV at the muscle 6/7 border was observed in *dC1GalT1* mutant larvae (Fig. 5). We tested whether same phenotype was observed in *dGlcAT-P* mutant larvae. To label the BMs, we used *vkg^{G454}* and an anti-Ndg antibody. Ndg is one of the main BM components. On the muscle 6/7 surface, Vkg-GFP and Ndg were evenly expressed in control (Fig. 12A–C) and both *dGlcAT-P* mutant larvae (Fig. 12D–I). The expression levels of Vkg-GFP and Ndg on the muscle surface were not different between the control and both *dGlcAT-P* mutant larvae. In the internal sectional views of the muscles, Vkg-GFP and Ndg were expressed along the line with muscle 6/7 border in the control larvae (Fig. 12A′–C′). In contrast, they were partially abolished at the muscle 6/7 border in the two *dGlcAT-P* null mutants

(arrowheads in Fig. 12D′–I′). The percentage of Ndg loss phenotype and the total range of Ndg loss at the muscle 6/7 border in the two *dGlcAT-P* null mutants were much higher than those in WT larvae (Fig. 12J and K). Furthermore, Ndg-deficiency phenotype was completely restored by the overexpression of *dGlcAT-P* in whole body on the mutant background (Fig. 12J and K). This phenotype was identical to that observed in *dC1GalT1* mutants. Therefore, these data suggested that the partial absence of BM components at the muscle 6/7 border was caused by the loss of glucuronylated T antigen expression.
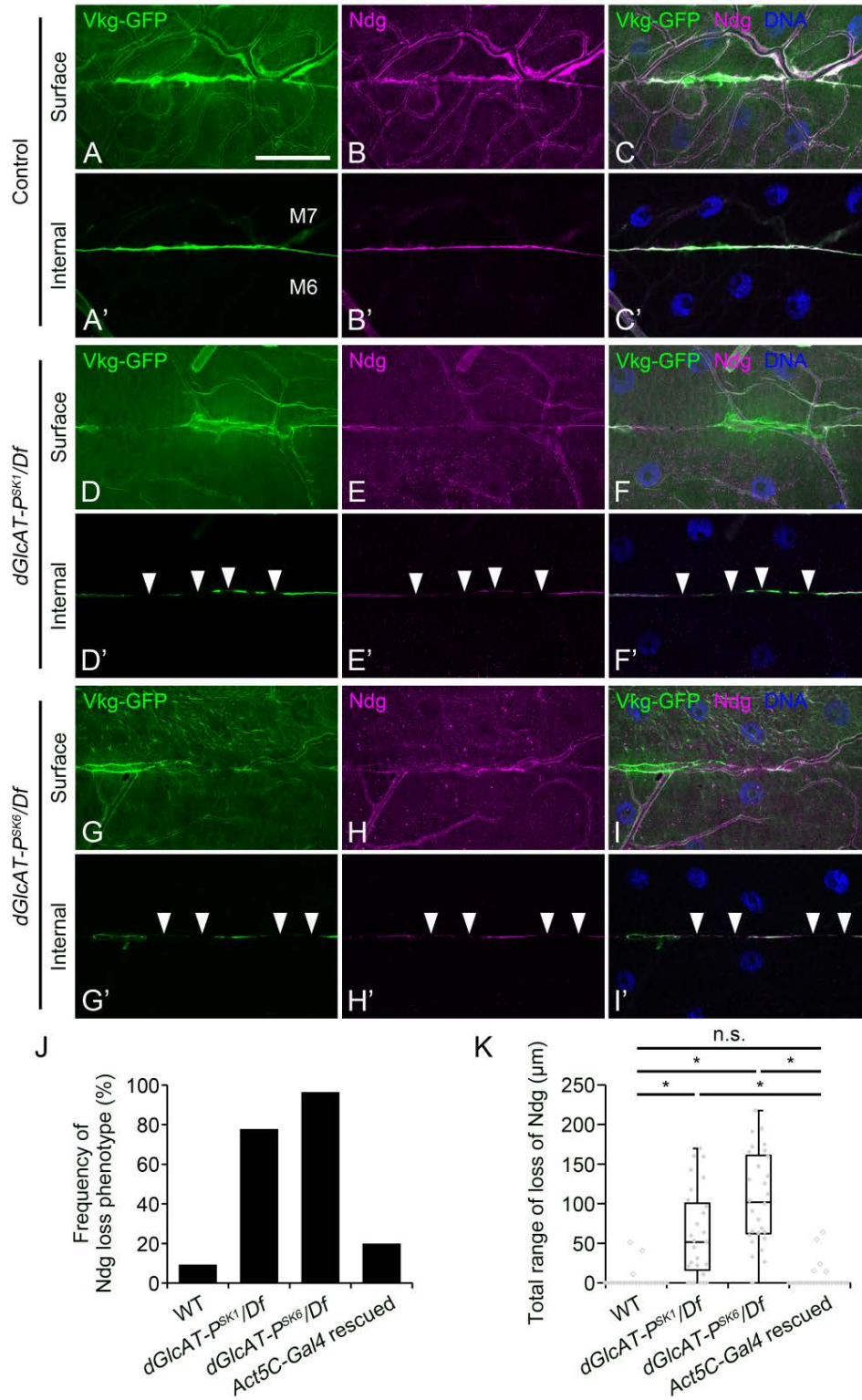
Fig. 12. Absence of collagen IV and nidogen at the muscle 6/7 border in *dGlcAT-P* mutants.
(A–I′) Representative confocal microscopic images of BMs on muscle 6 (M6) and muscle 7 (M7) at abdominal segment 3 in control (*vkg*^{G454}/+) (A–C′), *vkg*^{G454}/+; *dGlcAT-P*^{SK1}/*Df* (D–F′), and *vkg*^{G454}/+; *dGlcAT-P*^{SK6}/*Df* (G–I′) third-instar larvae. Surface sectional views of the muscles are shown in A–C, D–F, and G–I. Internal sectional views of the muscles are shown in A′–C′, D′–F′, and G′–I′. BMs were visualized with Vkg-GFP (green) and an anti-nidogen (Ndg) antibody (magenta). Cell nuclei (DNA) were stained with Hoechst 33342 (blue). Arrowheads in D′–F′ and G′–I′ indicate the absence of Vkg-GFP and Ndg at the muscle 6/7 border. Scale bar: 50 µm.
(J) Percentage of Ndg-deficiency phenotype in wild-type (WT; *n* = 32), *dGlcAT-P*^{SK1}/*Df* (*n* = 27), *dGlcAT-P*^{SK6}/*Df* (*n* = 28), and *Act5C-Gal4* rescued (*Act5C-Gal4/UAS-dGlcAT-P; dGlcAT-P*^{SK6}/*Df*; *n* = 25) larvae.
(K) Total range of Ndg loss at the muscle 6/7 border in WT (*n* = 32), *dGlcAT-P*^{SK1}/*Df* (*n* = 27), *dGlcAT-P*^{SK6}/*Df* (*n* = 28), and *Act5C-Gal4* rescued (*n* = 25) larvae. Statistical significance was evaluated by the Steel-Dwass test. **P* < 0.01; n.s.: not significant.

3-10. dGlcAT-P mutants displayed ectopic bouton localization at the muscle 6/7 border

As we showed that NMJ boutons were mispositioned at the muscle 6/7 border in the *dC1GalT1* mutants, we tested whether *dGlcAT-P* null mutant larvae also display such bouton mislocalization. Whereas many NMJ boutons were distant from the muscle 6/7 border in the WT (brackets in Fig. 13A), many boutons were positioned at the muscle 6/7 border in both the *dGlcAT-P* mutant larvae (white arrowheads in Fig. 13B and C). The distance form each bouton to the muscle 6/7 border in the two *dGlcAT-P* null mutants was significantly lower than that in WT larvae (Fig. 13E). The frequency of boutons mispositioned at the muscle 6/7 border (number of boutons positioned at the muscle 6/7 border per total bouton number) in the two *dC1GalT1* mutants was significantly higher than that in WT larvae (Fig. 13F). Both the decreased distance between each bouton and muscle 6/7 border and the increased frequency of boutons positioned at the muscle 6/7 border were suppressed in *Act5C-Gal4* rescued larvae (Fig. 13D–F). In addition, although the total number of boutons in the two *dGlcAT-P* mutants did not differ from that in WT larvae (Fig. 13G), the total number of branches was significantly lower in the two *dGlcAT-P* mutants compared with that in WT (Fig. 13H). Reduced number of NMJ branches was restored in *Act5C-Gal4* rescued larvae (Fig. 13H). Therefore, these results suggested that absence of glucuronylated core 1 glycan led to the ectopic bouton localization and reduced number of NMJ branches on muscle 6/7.
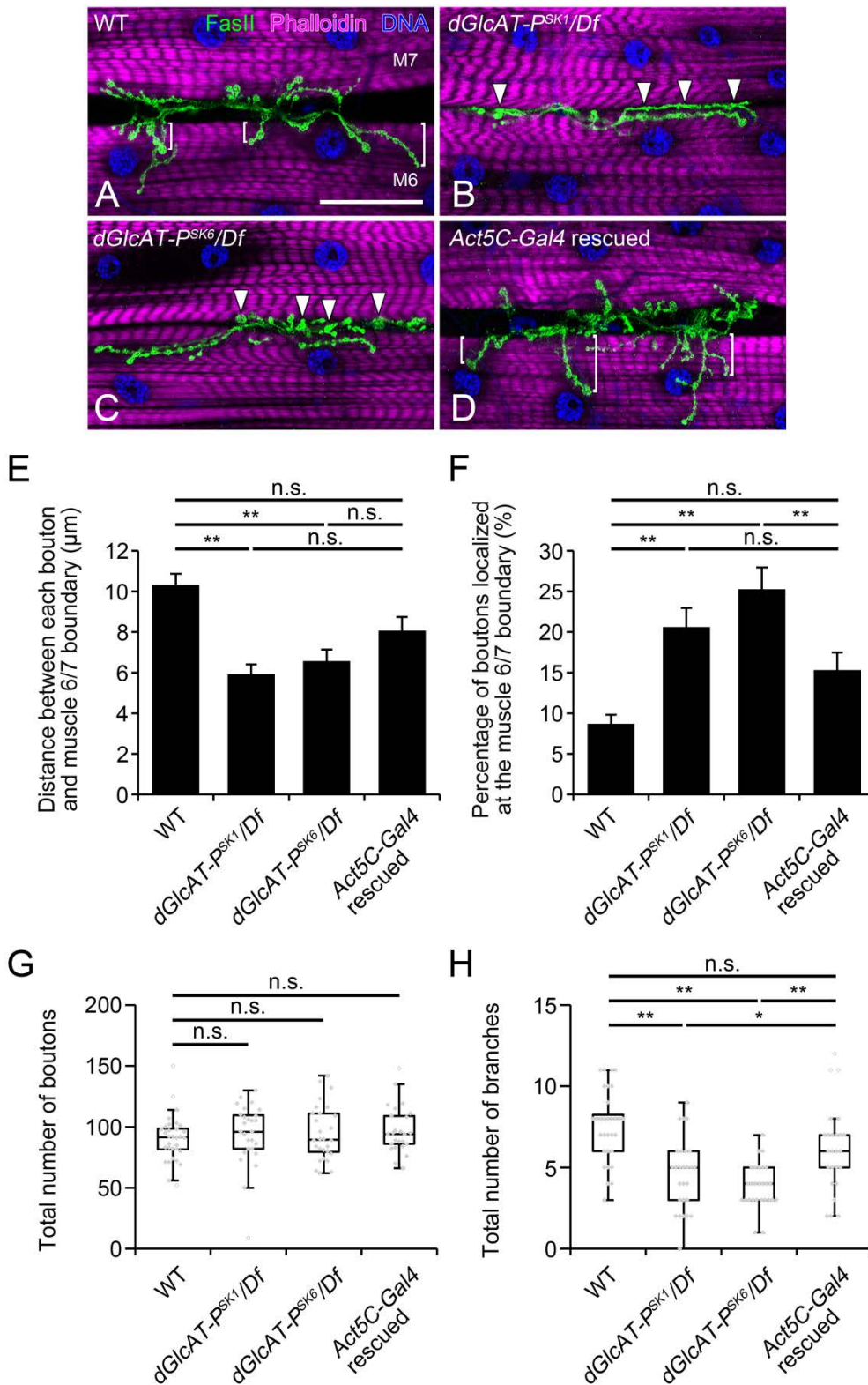
Fig. 13. Ectopic bouton localization at the muscle 6/7 border in *dGlcAT-P* mutants.
(A–D) Representative confocal microscopic images of NMJs on muscle 6 (M6) and muscle 7 (M7) at abdominal segment 3 in wild-type (WT) (A), *dGlcAT-P^{SK1}/Df* (B), *dGlcAT-P^{SK6}/Df* (C), and *Act5C-Gal4* rescued (*Act5C-Gal4/UAS-dGlcAT-P; dGlcAT-P^{SK6}/Df*) (D) third-instar larvae. Surface sectional views of the muscles are shown. NMJ boutons were stained with an anti-fasciclin II (Fas II) antibody (a presynaptic bouton marker; green). Muscle fibers and cell nuclei (DNA) were stained with phalloidin (magenta) and Hoechst 33342 (blue), respectively. Brackets in A and D indicate the distance between the bouton and muscle 6/7 border. Arrowheads in B and C show mispositioned

31

NMJ boutons at the muscle 6/7 border. Scale bars: 50 µm (A–D).

(E) Distance from each bouton to muscle 6/7 border in WT ($n = 32$), *dGlcAT-P*^{SK1}/*Df* ($n = 27$), *dGlcAT-P*^{SK6}/*Df* ($n = 28$), and *Act5C-Gal4* rescued ($n = 25$) larvae. Statistical significance was evaluated by the Steel-Dwass test. **P < 0.01; n.s.: not significant.

(F) Frequency of boutons positioned at the muscle 6/7 border in WT ($n = 32$), *dGlcAT-P*^{SK1}/*Df* ($n = 27$), *dGlcAT-P*^{SK6}/*Df* ($n = 28$), and *Act5C-Gal4* rescued ($n = 25$) larvae. Statistical significance was evaluated by the Tukey-Kramer test. **P < 0.01; n.s.: not significant.

(G) Total number of boutons on muscle 6/7 at abdominal segment 3 in WT ($n = 32$), *dGlcAT-P*^{SK1}/*Df* ($n = 27$), *dGlcAT-P*^{SK6}/*Df* ($n = 28$), and *Act5C-Gal4* rescued ($n = 25$) larvae. Statistical significance was evaluated by the Steel-Dwass test. n.s.: not significant.
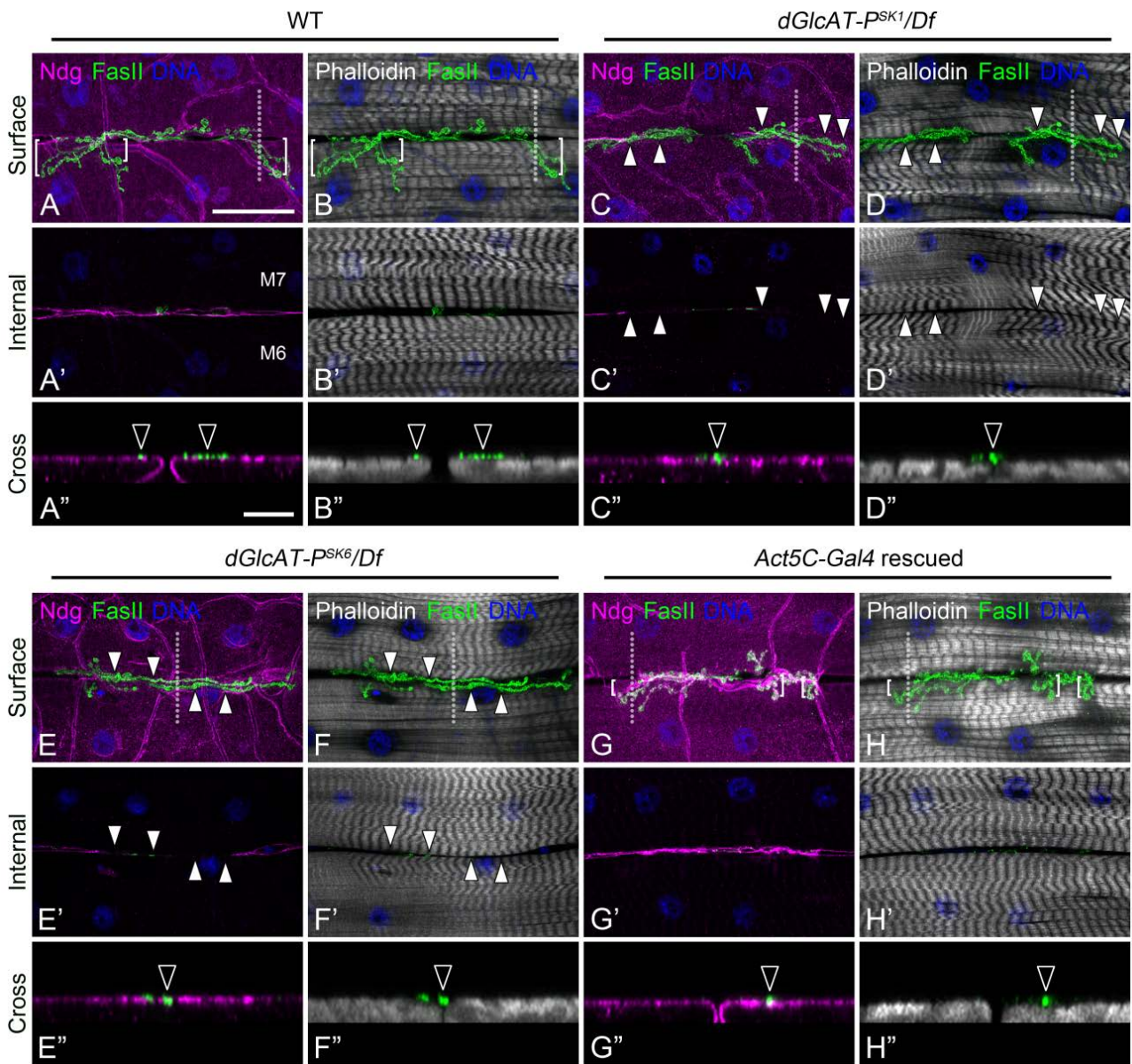
(H) Total number of branches of muscle 6/7 NMJs at abdominal segment 3 in WT ($n = 32$), *dGlcAT-P*^{SK1}/*Df* ($n = 27$), *dGlcAT-P*^{SK6}/*Df* ($n = 28$), and *Act5C-Gal4* rescued ($n = 25$) larvae. A branch was defined as a terminal neurite containing at least two boutons. Statistical significance was evaluated by the Tukey-Kramer test. *ature *P* < 0.05; **P < 0.01; n.s.: not significant.

3-11. Absence of basement membrane components was correlated with ectopic bouton localization in dGlcAT-P mutants

Next, to test whether there is a correlation between the two phenotypes, i.e., the partial absence of BM components and the ectopic bouton localization at the muscle 6/7 border, we analyzed the positional relationship between the sites devoid of Ndg and the mispositioned NMJ boutons at the muscle 6/7 border in the *dGlcAT-P* mutants (Fig. 14). As described above, in the surface sectional view of the muscles, although many boutons were distant from muscle 6/7 border in the WT (brackets in Fig. 14A and B), many boutons were mispositioned at the muscle 6/7 border in both the *dGlcAT-P* mutant larvae (white arrowheads in Fig. 14C–F). In the internal sectional view of the muscles, whereas Ndg was positioned along the line with muscle 6/7 border in the WT (Fig. 14A′), its expression was partially abolished at the muscle 6/7 border in both the *dGlcAT-P* mutant larvae (white arrowheads in Fig. 14C′ and E′). In *dGlcAT-P* null mutants, mispositioned NMJ boutons were frequently positioned just above Ndg-negative site at the muscle 6/7 border (white arrowheads in Fig. 14C, C′, E, and E′). In the cross sectional view of the muscles, muscles 6 and 7 were individually covered with separate BMs, and NMJ boutons were positioned on muscle surfaces in WT (Fig. 14A″ and B″). In contrast, two muscles were in close contact with each other and were covered with a continuous single BM in the two *dGlcAT-P* null mutants (Fig. 14C″–F″). Furthermore, a bouton was positioned at the muscle 6/7 border in both the *dGlcAT-P* mutants (black arrowheads in Fig. 14C″–F″). Beneath the mispositioned boutons, the close contact of the two muscles and absence of Ndg expression were frequently observed.

We found that there was a strong correlation between the total range of Ndg loss and the percentage of boutons mispositioned at the muscle 6/7 border in the two *dGlcAT-P* null mutants (Fig. 14I), showing that the two phenotypes, i.e., the partial absence of BM components and the ectopic bouton localization, were directly associated. Furthermore, to verify that mispositioned NMJ boutons are preferentially positioned just above the missing site of Ndg in the *dGlcAT-P* null mutants, we compared the frequency of boutons positioned just above the missing site of Ndg vs. the frequency of boutons positioned just above Ndg-positive site at the muscle 6/7 border in both the *dGlcAT-P* mutants (Fig. 14J). In both mutants, the former was significantly higher than the latter, clearly showing that mispositioned NMJ boutons tended to be positioned just above the missing site of Ndg at the muscle 6/7 border in the *dGlcAT-P* null mutants.

Therefore, these data demonstrated that the lack of glucuronylated core 1 glycan made NMJ boutons localize just above the site devoid of the BM components at the muscle 6/7 border.
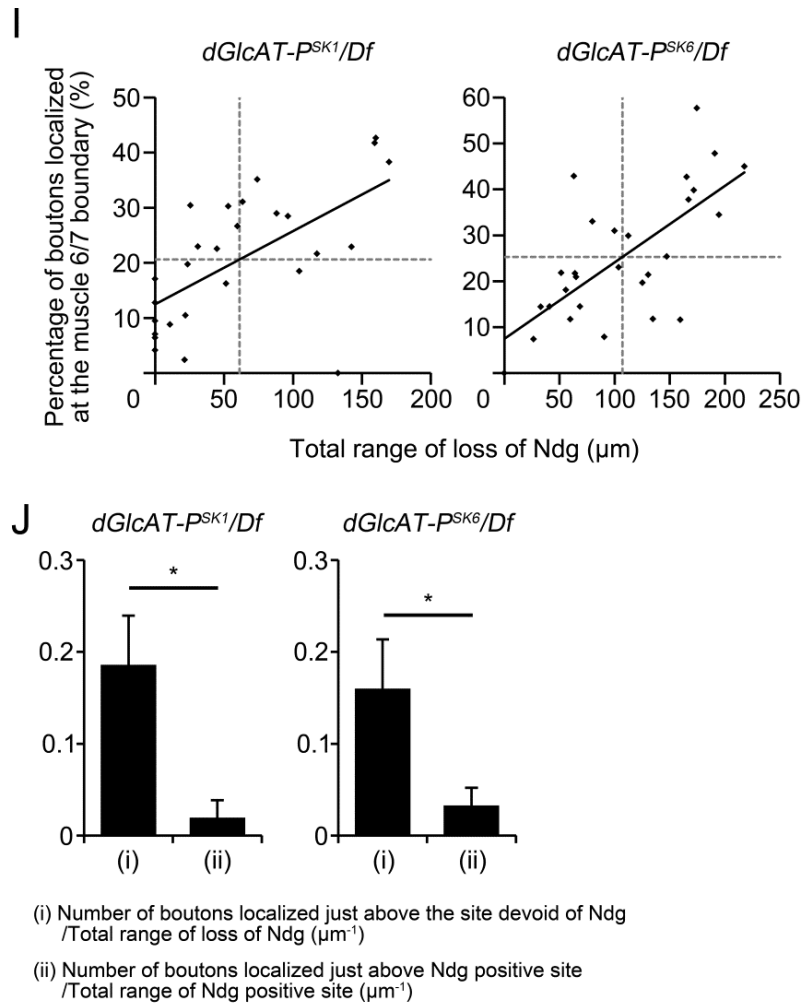
I dGlcAT-P^{SK1}/Df   dGlcAT-P^{SK6}/Df

(y-axis) Percentage of boutons localized at the muscle 6/7 boundary (%)

Total range of loss of Ndg (μm)

J dGlcAT-P^{SK1}/Df   dGlcAT-P^{SK6}/Df

(i) Number of boutons localized just above the site devoid of Ndg /Total range of loss of Ndg (μm^{-1})

(ii) Number of boutons localized just above Ndg positive site /Total range of Ndg positive site (μm^{-1})

Fig. 14. Correlation between Ndg loss and bouton mislocalization at the muscle 6/7 border in *dGlcAT-P* mutants.
(A–H″) Representative confocal microscopic images of BMs and NMJ boutons on muscle 6 (M6) and muscle 7 (M7) at abdominal segment 3 in wild-type (WT) (A–B″), *dGlcAT-P^{SK1}/Df* (C–D″), *dGlcAT-P^{SK6}/Df* (E–F″), and *Act5C-Gal4* rescued (*Act5C-Gal4/UAS-dGlcAT-P; dGlcAT-P^{SK6}/Df*) (G–H″) third-instar larvae. Surface sectional views of the muscles are shown in A–H. Internal sectional views of the muscles are shown in A′–H′. Cross-sectional views of the areas within white dotted-lines in A–H are shown in A″–H″. BMs and NMJ boutons were stained with an anti-nidogen (Ndg) antibody (magenta) and an anti-fasciclin II (Fas II) antibody (a presynaptic bouton marker; green), respectively. Muscle fibers and cell nuclei (DNA) were stained with phalloidin (white) and Hoechst 33342 (blue), respectively. Brackets in A, B, G, and H indicate the distance between the bouton and muscle 6/7 border. White arrowheads in C–F and C′–F′ show mispositioned NMJ boutons and Ndg-negative site at the muscle 6/7 border, respectively. Black arrowheads in A″–H″ indicate positions of NMJ boutons. Scale bars: 50 μm (A–H′) and 10 μm (A″–H″).
(I) Correlation between the total range of Ndg loss and the percentage of boutons positioned at the muscle 6/7 border in *dGlcAT-P^{SK1}/Df* ($n = 27$; left) and *dGlcAT-P^{SK6}/Df* ($n = 28$; right) larvae. Values of the Pearson's correlation coefficient r comprised 0.62 and 0.69 for *dGlcAT-P^{SK1}/Df* and *dGlcAT-P^{SK6}/Df*, respectively. Black straight line indicates the approximate line. Gray cross-dotted-lines indicate the average lines.
(J) A comparison between 'frequency of boutons positioned just above Ndg-negative site at the muscle 6/7 border' vs. 'frequency of boutons positioned just above Ndg-positive site at the muscle 6/7 border' in *dGlcAT-P^{SK1}/Df* ($n \geq 21$; left) and *dGlcAT-P^{SK6}/Df* ($n \geq 26$; right) larvae. Statistical significance was evaluated by the Student's *t*-test. *$P < 0.001$.

3-12. Ultrastructural analysis of mispositioned NMJ boutons in dGlcAT-P mutants

To analyze in detail mispositioned NMJ boutons in *dGlcAT-P* null mutants, we carried out the ultrastructural analysis by TEM. The surface and internal sections of muscles 6 and 7 were observed (Fig. 15A). Assessment of the BM with TEM showed that it was composed of the basal lamina, which was an

34

electron dense band, and lamina lucida, which was an electron-lucent area between the basal lamina and plasma membrane. In the surface section of the muscles, NMJ boutons were hardly observed at the muscle 6/7 border, and each muscle surface was covered with basal lamina in WT larvae (Fig. 15B and B′). However, in the two *dGlcAT-P* null mutant larvae, NMJ boutons were observed at the muscle 6/7 border and connected two muscles (Fig. 15D, D′, F, and F′). Because light microscopic imaging revealed that the main BM components were abolished beneath mispositioned NMJ boutons as described above (Fig. 14), we thus expected that basal laminae would be absent beneath mispositioned NMJ boutons. In the TEM internal section of muscles, against our expectation, basal laminae were observed at the muscle 6/7 border in the two *dGlcAT-P* null mutants (Fig. 15E, E′, G, and G′) similarly as that in WT larvae (Fig. 15C and C′). However, whereas single layered basal laminae were observed on each muscle in WT (Fig. 15C′, black arrowheads), basal laminae were duplicated and ruptured in *dGlcAT-P^{SK1}/Df* larvae (Fig. 15E′, black and white arrowheads, respectively) and were duplicated and thin in *dGlcAT-P^{SK6}/Df* larvae (Fig. 15G′, black arrowheads). Ectopic bouton localization and defects of the basal lamina were completely restored in *Act5C-Gal4* rescued larvae (Fig. 15H–I′).

Together, light microscopy and TEM analyses showed that in *dGlcAT-P* null mutants, NMJ boutons were ectopically positioned at the muscle 6/7 border and connected the two muscles (Fig. 15A). A continuous single BM, which was Col IV/Ndg-positive, surrounded the dorsal surfaces of mispositioned NMJ boutons and muscle 6/7. Moreover, beneath the mispositioned NMJ boutons, Col IV/Ndg-negative BMs were severely deformed. Therefore, these data clearly showed that glucuronylated core 1 glycan was required for the positioning of NMJ boutons and formation of BMs on muscle 6/7.
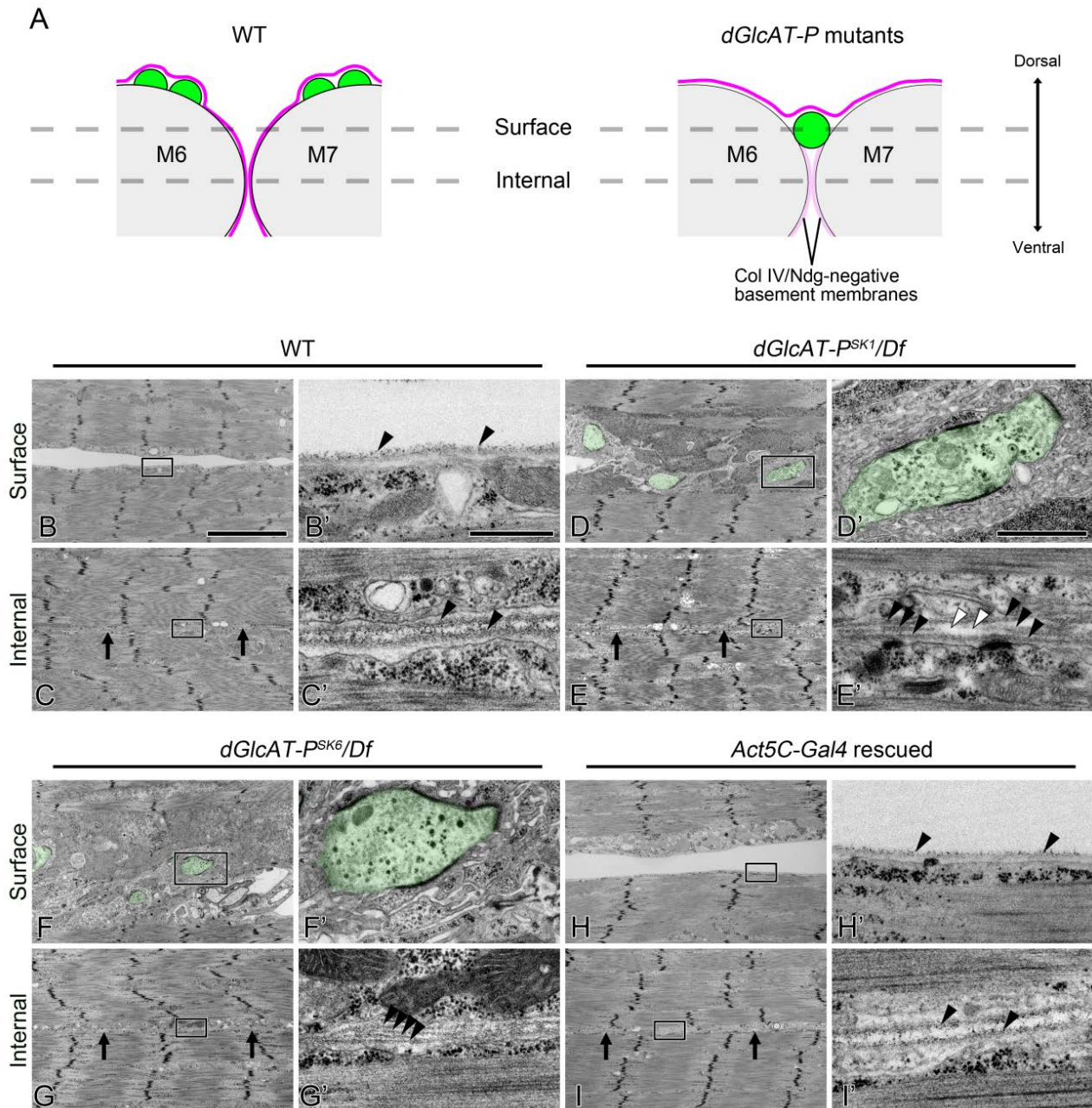
Fig. 15. Ultrastructural analysis of the muscle 6/7 border in *dGlcAT-P* mutants.
(**A**) Schematic diagrams of cross sectional views of muscles 6 and 7 in wild-type (WT; left) and *dGlcAT-P* null mutants (right). Normal BMs (collagen IV [Col IV]/nidogen [Ndg]-positive) and NMJ boutons are shown in magenta and green, respectively. Col IV/Ndg-negative BMs in *dGlcAT-P* mutants are shown in light magenta. Upper and lower dotted-lines reveal surface and internal sections, respectively. A double-headed arrow reveals dorsal and ventral surface of the muscles.
(**B–I′**) Transmission electron micrographs of the muscle 6/7 border at abdominal segment 3 in WT (B–C′), *dGlcAT-P^{SK1}/Df* (D–E′), *dGlcAT-P^{SK6}/Df* (F–G′), and *Act5C-Gal4* rescued (*Act5C-Gal4/UAS-dGlcAT-P; dGlcAT-P^{SK6}/Df*) (H–I′) third-instar larvae. Surface sections of the muscles are shown in B, B′, D, D′, F, F′, H, and H′. Internal sections of the muscles are shown in C, C′, E, E′, G, G′, I, and I′. Low-magnification images of the muscle 6/7 border are shown in B–I. High-magnification views of the area bordered by a rectangle in B–I are shown in B′–I′. Presynaptic boutons are shown in green in D, D′, F, and F′. Arrows in C, E, G, and I reveal the muscle 6/7 border. Black arrowheads in B′, C′, H′, and I′ reveal normal basal laminae on the muscle 6/7 surface. Black arrowheads in E′ and G′ reveal duplicated basal laminae. White arrowheads in E′ reveal the rupture of the basal lamina. Scale bars: 5 µm (B–I), 500 nm (B′, C′, E′, G′, H′, and I′), and 1 µm (D′ and F′).

36

3-13. *dGlcAT-P genetically interacted with dC1GalT1*

As *dGlcAT-P* mutants displayed some phenotypes identical to those observed in *dC1GalT1* mutants, we expected that *dGlcAT-P* may genetically interact with *dC1GalT1*. We then tested whether double heterozygous mutants of *dGlcAT-P* and *dC1GalT1* showed BM and NMJ phonotype (Fig. 16). In the double heterozygous mutants, some NMJ boutons were present just above Ndg-negative site at the muscle 6/7 border (white arrowheads, Fig. 16E–F′). Furthermore, in the cross sectional view of the muscles, a bouton indicated by a black arrowhead was positioned at the muscle 6/7 border, and the two muscles were covered with a continuous single BM (Fig. 16E″ and F″). In contrast, single heterozygous mutants of *dGlcAT-P* and *dC1GalT1* hardly show these phenotypes (Fig. 16A–B″ and C–D″). Frequency of Ndg loss phenotype in the double heterozygous mutants was higher than that in the single heterozygous mutants (Fig. 16G). In addition, the total range of Ndg loss at the muscle 6/7 border was also significantly increased in the double heterozygous mutants compared with that in the single heterozygous mutants (Fig. 16H). Together, these results demonstrated that there was a genetic interaction between *dGlcAT-P* and *dC1GalT1* and that glucuronylated core 1 glycan, rather than unmodified core 1 glycan, regulated the positioning of NMJ boutons and organization of BMs on larval muscles.
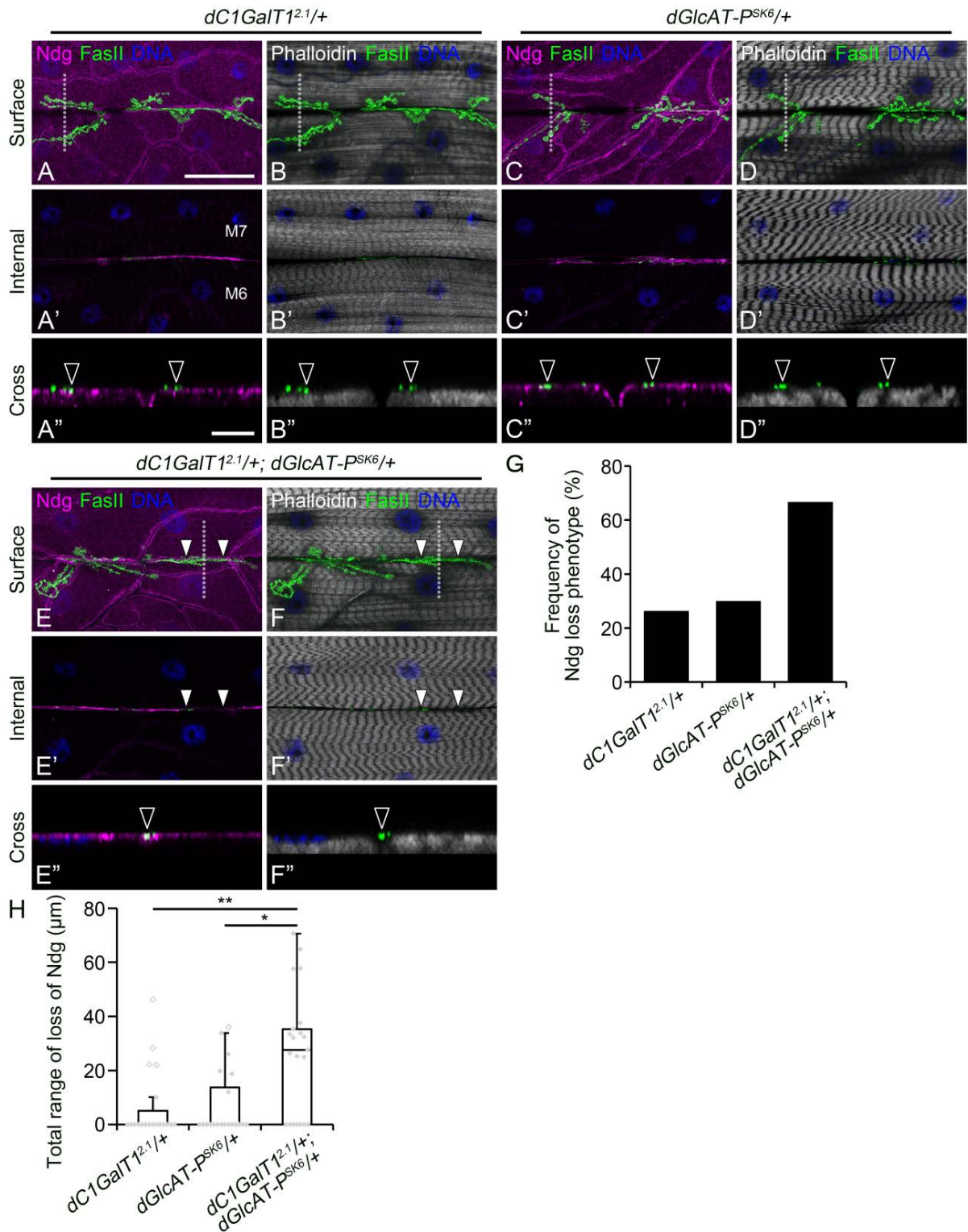
Fig. 16. Genetic interaction between *dC1GalT1* and *dGlcAT-P*.
(A–F″) Representative confocal microscopic images of BMs and NMJ boutons on muscle 6 (M6) and muscle 7 (M7) at abdominal segment 3 in *dC1GalT1$^{2.1}$/+* (A–B″), *dGlcAT-P^{SK6}/+* (C–D″), and *dC1GalT1$^{2.1}$/+; dGlcAT-P^{SK6}/+* (E–F″) larvae. Surface sectional views of the muscles are shown in A–F. Internal sectional views of the muscles are shown in A′–F′. Cross-sectional views of the areas within white dotted-lines in A–F are shown in A″–F″. BMs and NMJ boutons were stained with an anti-nidogen (Ndg) antibody (magenta) and an anti-fasciclin II (Fas II) antibody (green), respectively. Muscle fibers and cell nuclei (DNA) were stained with phalloidin (white) and Hoechst 33342 (blue), respectively. White arrowheads in E/F and E′/F′ reveal mispositioned NMJ boutons and Ndg-negative site, respectively. Black arrowheads in A″–F″ indicate positions of NMJ boutons. Scale bars: 50 µm (A–F′) and 10 µm (A″–F″).

38

(G) Percentage of Ndg-deficiency phenotype in $dC1GalT1^{2.1}/+$ ($n = 19$), $dGlcAT\text{-}P^{SK6}/+$ ($n = 20$), and $dC1GalT1^{2.1}/+$; $dGlcAT\text{-}P^{SK6}/+$ ($n = 21$) larvae.

(H) Total range of Ndg loss at the muscle 6/7 border in $dC1GalT1^{2.1}/+$ ($n = 19$), $dGlcAT\text{-}P^{SK6}/+$ ($n = 20$), and $dC1GalT1^{2.1}/+$; $dGlcAT\text{-}P^{SK6}/+$ ($n = 21$) larvae. Statistical significance was evaluated by Steel-Dwass test. $*P < 0.05$; $**P < 0.01$.

3-14. Absence of dC1GalT1 expression resulted in various ultrastructural defects in NMJ boutons

Next, we analyzed whether ultrastructural defects were observed in NMJ boutons of *dC1GalT1* and *dGlcAT-P* mutants using TEM. Schematic diagram of NMJ bouton ultrastructure is shown in Fig. 17. We firstly observed the *dC1GalT1* mutant NMJ boutons (Fig. 18 and Table 6). On the presynaptic side of NMJ boutons, the diameter of vesicles was significantly increased in *dC1GalT1* mutants compared with that in WT larvae (Fig. 18D and F). It has been reported that vesicle smaller than 80 nm in diameter is considered to be synaptic vesicle, and vesicle larger than 80 nm in diameter is considered to be large endosome-like structure (cisterna), which is observed in endocytic mutants (Zhang et al., 1998; Guichet et al., 2002; Kasprowicz et al., 2008; Matta et al., 2012; Winther et al., 2013; West et al., 2015). The diameter of vesicles smaller than 80 nm in diameter (synaptic vesicles) was not different between the WT and *dC1GalT1* mutants (Fig. 18E). However, percentage of vesicles larger than 80 nm in diameter (large endosome-like structures) in the *dC1GalT1* mutants was higher than that in WT larvae (arrowheads in Fig.18C′ and Fig. 18G). T-bars, electron-dense T-shaped structures, frequently stand on the intracellular side of the presynaptic membrane (Prokop, 1999; Verstreken et al., 2002). To release neurotransmitters, synaptic vesicles gather beside the T-bar and fuse to the presynaptic membrane underneath the T-bar. However, the number of vesicles within 250 nm from T-bar and the number of T-bars per bouton were not different between the WT and *dC1GalT1* mutant larvae (Table 6). Therefore, these results suggested that mucin-type *O*-glycans might be involved in endocytosis in presynaptic NMJ boutons.
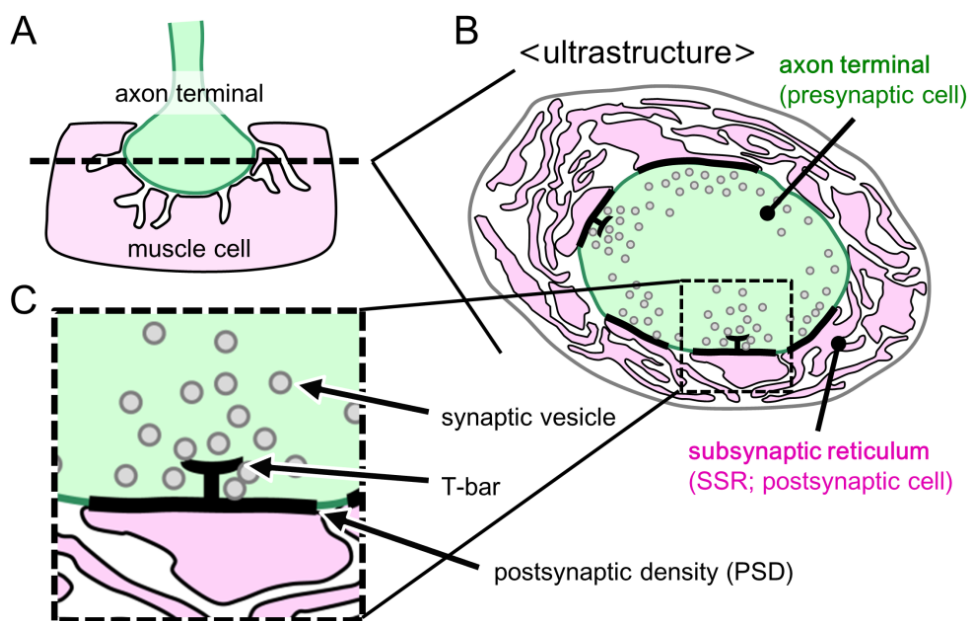

Fig. 17. Schematic diagram of NMJ bouton ultrastructure.
(A) At the NMJs, axon terminal is surrounded by muscle cell that forms folded structure.
(B) Bouton ultrastructure observed by transmission electron microscope is shown. The folded structure of muscle cell is

called subsynaptic reticulum (SSR).

(C) Magnified view of the area bordered by a rectangle in B is shown. In the presynaptic cell, a number of synaptic vesicles accumulate around T-bar that locates on the intracellular side of presynaptic membrane. Neurotransmitters are released beneath the T-bar. Postsynaptic density (PSD), which is electron-dense area of postsynaptic membrane, includes neurotransmitter receptors, adhesion proteins, signaling molecules, scaffolding molecules, and ion channels.

On the postsynaptic side of NMJ boutons, the thickness of SSR per bouton area in the *dC1GalT1* mutants was significantly higher than that in WT larvae (Fig. 18H). However, SSR density (layer number per SSR thickness) in the *dC1GalT1* mutants was significantly lower than that in WT larvae (Fig.18I). Additionally, the length of PSD was significantly reduced in the *dC1GalT1* mutants compared with that in WT larvae (Fig. 18J). However, the number of PSDs per bouton and the depth of PSP in the *dC1GalT1* mutants did not differ from those in WT larvae (Table 6). Therefore, these results suggested that mucin-type *O*-glycans regulated the SSR formation and PSD organization in postsynaptic NMJ boutons.
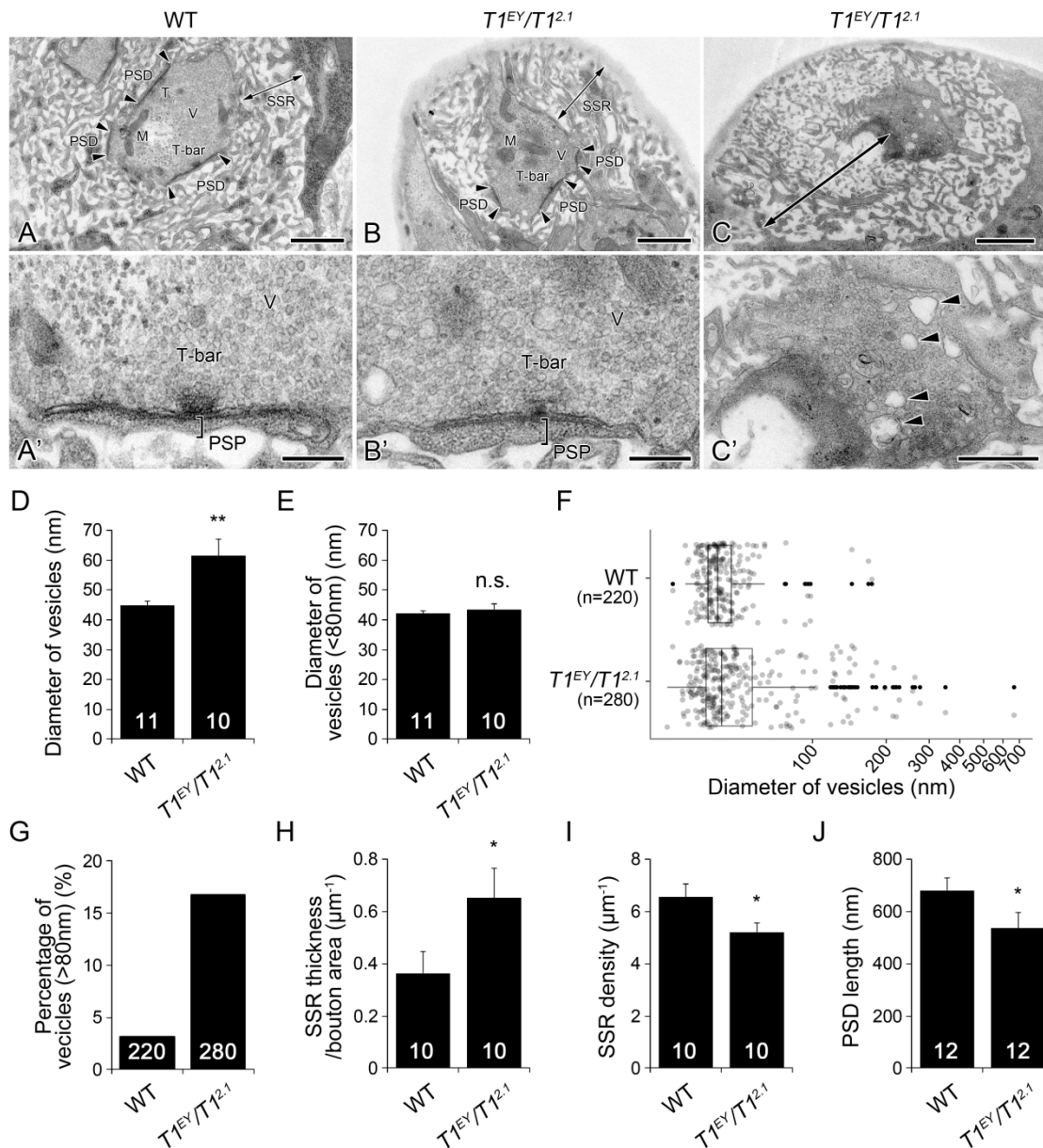

Fig. 18. Ultrastructural aberrations of *dC1GalT1* mutant NMJ boutons.

(**A–C′**) Transmission electron micrographs of NMJs (type Ib boutons) on muscle 6 at abdominal segment 3 in wild-type (WT) (A and A′) and $T1^{EY}/T1^{2.1}$ ($dC1GalT1^{EY13370}/dC1GalT1^{2.1}$) (B–C′) third instar larvae. High-magnification views of T-bar in A and B are presented in A′ and B′. High-magnification view of the presynaptic area in C is presented in C′. Arrowheads in A and B indicate postsynaptic density (PSD) and its length. The double-headed arrows in A–C indicate subsynaptic reticulum (SSR) and its thickness. The U-shaped objects in A′ and B′ indicate postsynaptic pocket (PSP) and its depth. Arrowheads in C′ indicate vesicles larger than 80 nm in diameter, large endosome-like structures. V: vesicle, M: mitochondria. Scale bars: 1 µm (A–C), 250 nm (A′ and B′), and 500 nm (C′).

(**D and E**) Quantification of the diameters of all vesicles (D) and the diameters of vesicles smaller than 80 nm in diameter (synaptic vesicles) (E) in WT and $T1^{EY}/T1^{2.1}$ larvae. Data are the mean ± standard error for each genotype. Statistical significance was evaluated by the Student's t-test. **$P < 0.01$; n.s.: not significant.

(**F**) Box and dot plot of the diameters of vesicles in WT and $T1^{EY}/T1^{2.1}$ larvae. Gray and black dots indicate measured values and outliers, respectively.

(**G**) Percentages of vesicles larger than 80 nm in diameter (large endosome-like structures) in WT and $T1^{EY}/T1^{2.1}$ larvae.

(**H–J**) Quantification of SSR thickness per bouton area (H), SSR density (layer number per SSR thickness) (I), and PSD length (J) in WT and $T1^{EY}/T1^{2.1}$ larvae. Data are the mean ± standard error for each genotype. Statistical significance was evaluated by the Student's t-test. *$P < 0.05$.

The numbers in the bar graphs represent the number of NMJ boutons (D, E, H, I, and J) and vesicles (G) in which respective measurements were performed.

Table 6. Ultrastructural analysis of *dC1GalT1* mutant NMJ boutons.

Ultrastructure	WT	$T1^{EY}/T1^{2.1}$
Presynaptic side		
Number of T-bars/bouton	2.0 ± 0.4 ($n = 10$)	1.3 ± 0.4 ($n = 10$)
Diameter of vesicles (nm)	44.8 ± 1.5 ($n = 11$)	61.4 ± 5.5** ($n = 10$)
Diameter of vesicles (< 80 nm) (nm)	42.2 ± 0.7 ($n = 11$)	43.5 ± 1.7 ($n = 10$)
Percentage of vesicles (> 80 nm) (%)	3.2 ($n = 220$)	16.8 ($n = 280$)
Number of vesicles < 250 nm from T-bar	43.9 ± 3.2 ($n = 10$)	39.4 ± 1.9 ($n = 10$)
Postsynaptic side		
Number of PSDs/bouton	4.8 ± 1.5 ($n = 10$)	4.6 ± 1.5 ($n = 10$)
PSD length (µm)	681.4 ± 47.9 ($n = 12$)	536.9 ± 61.1* ($n = 12$)
SSR thickness/bouton area (µm^{-1})	0.4 ± 0.08 ($n = 10$)	0.7 ± 0.1* ($n = 10$)
SSR density (µm^{-1})	6.6 ± 0.5 ($n = 10$)	5.2 ± 0.3* ($n = 10$)
PSP depth (nm)	216.6 ± 37.6 ($n = 10$)	158.1 ± 26.2 ($n = 11$)

Data are presented as the mean ± standard error of the mean. Statistical significance was assessed by either the Dunnett or Steel test. * $P < 0.05$, ** $P < 0.01$.

3-15. *Absence of dGlcAT-P expression resulted in various ultrastructural defects in NMJ boutons*

We then observed the *dGlcAT-P* mutant NMJ boutons (Fig. 19 and Table 7). On the presynaptic side of NMJ boutons, in contrast with the *dC1GalT1* mutants, the diameter of vesicles was significantly reduced in both *dGlcAT-P* mutants compared with that in WT larvae (Fig. 19D). The diameter of vesicles smaller than 80 nm in diameter (synaptic vesicles) in both *dGlcAT-P* mutants was significantly lower than that in WT larvae (Fig. 19E). The frequency of vesicles larger than 80 nm in diameter (large endosome-like structures) was reduced in both *dGlcAT-P* mutants (Fig. 19F). Furthermore, the number of vesicles within 250 nm from the T-bar was significantly decreased in both *dGlcAT-P* mutants compared with that in WT larvae (Fig. 19G), although the total number of vesicles per bouton area was not different between WT and both *dGlcAT-P*

mutant larvae (Table 7). However, the number of T-bars per bouton in both *dGlcAT-P* mutants did not differ from that in WT larvae (Table 7). Therefore, these results showed that the depletion of dGlcAT-P expression reduced the synaptic vesicle size, frequency of large endosome-like structures, and number of synaptic vesicles around the T bar in presynaptic NMJ boutons.

On the postsynaptic side of NMJ boutons, the PSD length in both *dGlcAT-P* mutants was significantly shorter than that in WT larvae (Fig. 19H). This phenotype was the same phenotype observed in the *dC1GalT1* mutants, suggesting that glucuronylated T antigen contributed to PSD organization. Moreover, the PSP depth was expanded in both *dGlcAT-P* mutants compared with that in WT larvae (Fig. 19I). However, the number of PSDs per bouton, SSR thickness per bouton area, and SSR density were similar in WT and both *dGlcAT-P* mutant larvae (Table 7). Therefore, these data revealed that the absence of dGlcAT-P expression caused shorter PSD length and expanded PSP depth in postsynaptic NMJ boutons.
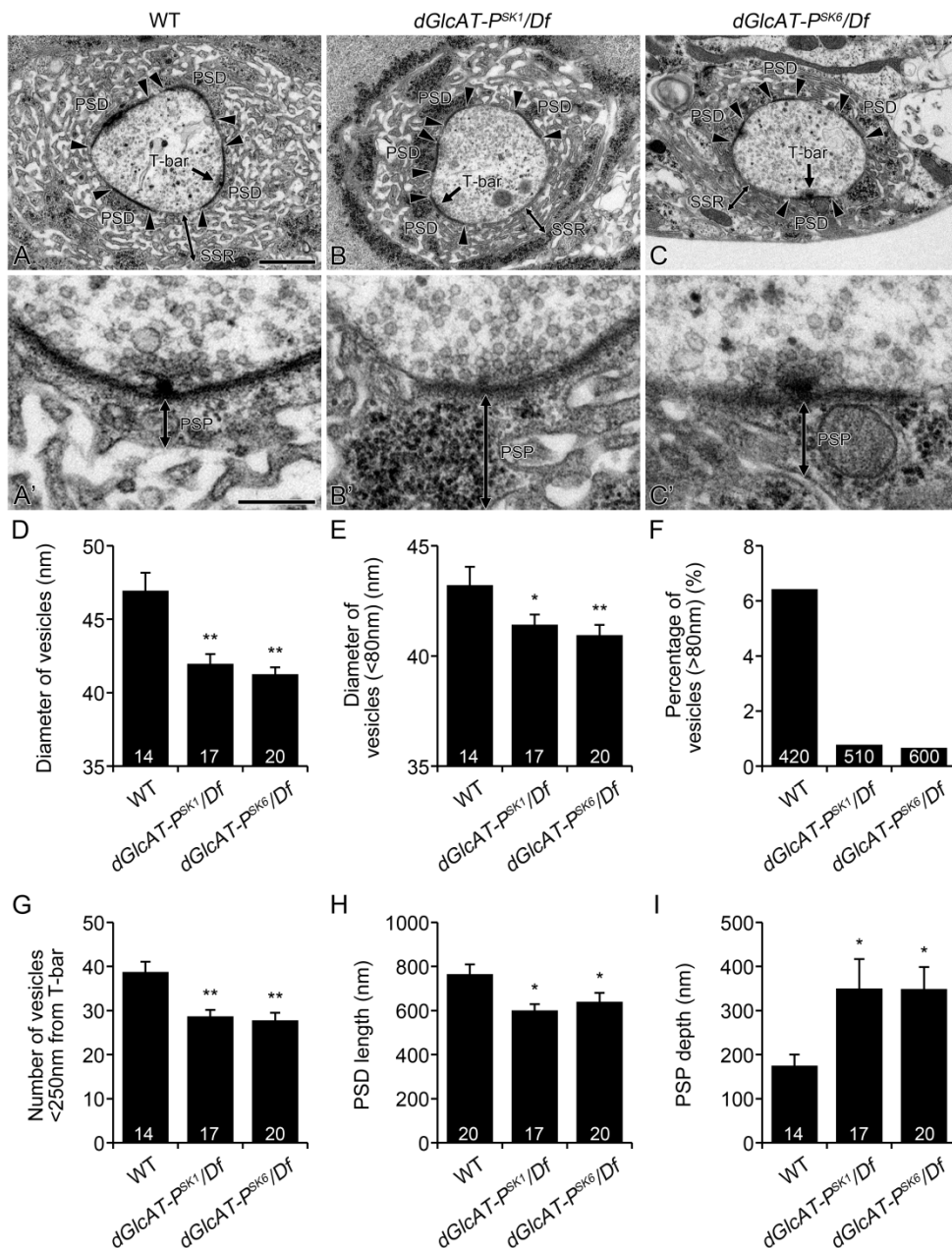
Fig. 19. Ultrastructural aberrations of *dGlcAT-P* mutant NMJ boutons.

(A–C′) Transmission electron micrographs of NMJs (type Ib boutons) on muscle 6 at abdominal segment 3 in wild-type (WT) (A and A′), *dGlcAT-P^{SK1}/Df* (B and B′), and *dGlcAT-P^{SK6}/Df* (C and C′) third-instar larvae. High magnification views of T-bar revealed by an arrow in A–C are shown in A′–C′. Arrowheads in A–C reveal the postsynaptic density (PSD) and its length. The double-headed arrows in A–C reveal subsynaptic reticulum (SSR) and its thickness. The double-headed arrows in A′–C′ reveal postsynaptic pocket (PSP) and its depth. Scale bars: 1 µm (A–C) and 250 nm (A′–C′).
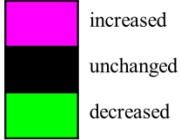
(D–I) Quantification of the diameter of all vesicles (D), diameter of vesicles smaller than 80 nm in diameter (synaptic vesicles) (E), percentage of vesicles larger than 80 nm in diameter (large endosome-like structures) (F), number of vesicles within 250 nm from a T-bar (G), length of PSDs (H), and depth of PSPs (I) at WT and two *dGlcAT-P* mutant NMJs. The numbers inside the bars show the numbers of NMJ boutons (D, E, G, H, and I) and vesicles (F) in which respective measurements were carried out. Data are shown as the mean ± standard error of the mean for each genotype. Statistical significance was evaluated by either the Dunnett or Steel test, as appropriate. *$P < 0.05$; **$P < 0.01$.

Table 7. Ultrastructural analysis of *dGlcAT-P* mutant NMJ boutons.

Ultrastructure	WT	*dGlcAT-P^{SK1}/Df*	*dGlcAT-P^{SK6}/Df*
Presynaptic side			
Number of T-bars/bouton	1.8 ± 0.3 ($n = 20$)	1.0 ± 0.2 ($n = 17$)	2.1 ± 0.3 ($n = 20$)
Diameter of vesicles (nm)	46.9 ± 1.2 ($n = 14$)	42.0 ± 0.7** ($n = 17$)	41.3 ± 0.5** ($n = 20$)
Diameter of vesicles (< 80 nm) (nm)	43.2 ± 0.8 ($n = 14$)	41.4 ± 0.5* ($n = 17$)	40.9 ± 0.5** ($n = 20$)
Percentage of vesicles (> 80 nm) (%)	6.4 ($n = 420$)	0.8 ($n = 510$)	0.7 ($n = 600$)
Number of vesicles < 250 nm from T-bar	38.8 ± 2.3 ($n = 14$)	28.7 ± 1.4** ($n = 17$)	27.8 ± 1.7** ($n = 20$)
Total vesicle number/bouton area (µm^{-2})	103.3 ± 17.5 ($n = 14$)	102.6 ± 16.1 ($n = 17$)	109.8 ± 9.2 ($n = 20$)
Postsynaptic side			
Number of PSDs/bouton	4.5 ± 0.3 ($n = 20$)	4.4 ± 0.4 ($n = 17$)	5.1 ± 0.5 ($n = 20$)
PSD length (µm)	0.8 ± 0.04 ($n = 20$)	0.6 ± 0.03* ($n = 17$)	0.6 ± 0.04* ($n = 20$)
SSR thickness/bouton area (µm^{-1})	0.3 ± 0.04 ($n = 20$)	0.2 ± 0.02* ($n = 17$)	0.3 ± 0.03 ($n = 20$)
SSR density (µm^{-1})	6.8 ± 0.2 ($n = 20$)	7.3 ± 0.4 ($n = 17$)	6.6 ± 0.2 ($n = 20$)
PSP depth (nm)	175.0 ± 24.9 ($n = 14$)	350.1 ± 66.4* ($n = 17$)	348.8 ± 49.5* ($n = 20$)

Data are presented as the mean ± standard error of the mean. Statistical significance was assessed by either the Dunnett or Steel test. * $P < 0.05$, ** $P < 0.01$.

	$T1^{EY}/T1^{2.1}$	$dGlcAT\text{-}P^{SK1}/Df$	$dGlcAT\text{-}P^{SK6}/Df$
Presynaptic side			
Number of T-bars/bouton			
Diameter of vesicles (nm)	**	**	**
Diameter of vesicles (< 80 nm) (nm)		*	**
Percentage of vesicles (> 80 nm) (%)			
Number of vesicles < 250 nm from T-bar		**	**
Total vesicle number/bouton area (μm^{-2})	-		
Postsynaptic side			
Number of PSDs/bouton			
PSD length (μm)	*	*	*
SSR thickness/bouton area (μm^{-1})	*	*	
SSR density (μm^{-1})	*		
PSP depth (nm)		*	*

(magenta)	increased
(black)	unchanged
(green)	decreased

Fig. 20. Comparison of ultrastructural defects in *dC1GalT1* and *dGlcAT-P* mutant NMJ boutons.
Magenta color means that mutant data are significantly increased compared with wild-type (WT) data. Black color means that there is no significant difference between mutant and WT data. Green color means that mutant data are significantly decreased compared with WT data. Statistical significance was assessed by either the Dunnett or Steel test. * $P < 0.05$, ** $P < 0.01$.

3-16. Locomotor activity of dC1GalT1 and dGlcAT-P mutant larvae

As various ultrastructural defects were observed in NMJ boutons of both *dC1GalT1* and *dGlcAT-P* mutants, we expected that these defects affected NMJ neurotransmission and motility function in larvae. To examine this, we performed a larval locomotion assay. Contrary to our expectation, the locomotor activity was not different between WT and both the mutant larvae (Fig. 21).
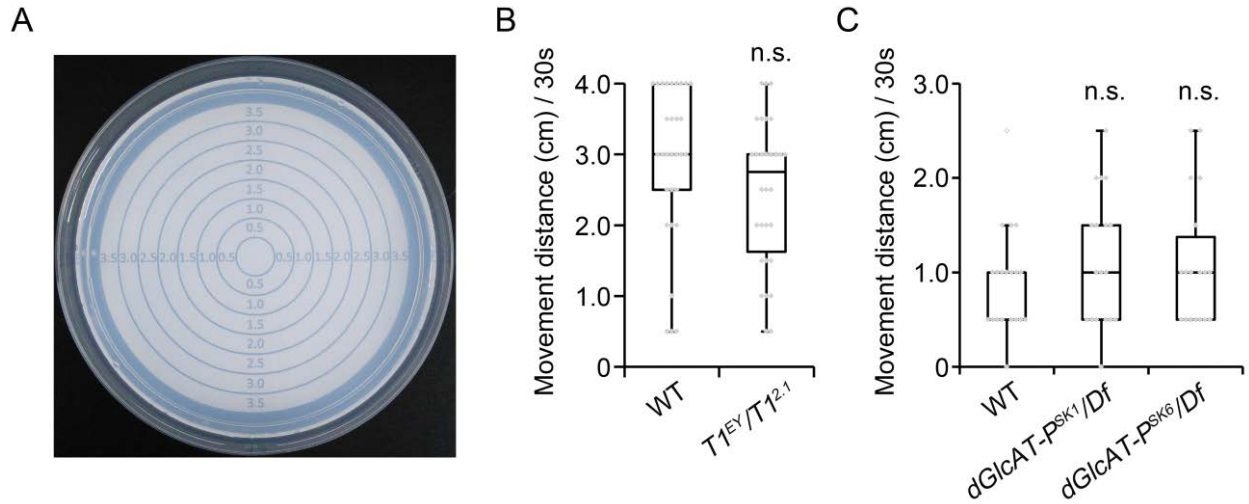
44

Fig. 21. Larval locomotion assay.
(A) An image of a 9 cm plastic dish with 3% non-nutritive agar solution on multiple circles. A wandering third-instar larva was put at the center of multiple circles, and the movement distance of the larva during 30 s was measured.
(B) Movement distance per 30 s of wild-type (WT) ($n = 30$) and $T1^{EY}/T1^{2.1}$ ($n = 30$) wandering third-instar larvae. Statistical significance was evaluated by the Student's t-test. n.s.: not significant.
(C) Movement distance per 30 s of WT ($n = 20$), $dGlcAT\text{-}P^{SK1}/Df$ ($n = 18$), and $dGlcAT\text{-}P^{SK6}/Df$ ($n = 18$) wandering third-instar larvae. Statistical significance was evaluated by the Steel test. n.s.: not significant.

4. Discussion

We clarify for the first time the physiological functions of glucuronylated core 1 glycan in *Drosophila*. Firstly, we found that glucuronylation of T antigen was predominantly catalyzed by dGlcAT-P but not by other dGlcATs. *dGlcAT-P* null mutants, which we newly generated, exhibited increased expression of T antigen on the muscle surface and at NMJs, showing that glucuronylated form of T antigen was expressed in those tissues. Both *dC1GalT1* and *dGlcAT-P* mutant larvae displayed common three phenotypes, i.e., (1) the partial absence of main BM components, (2) ectopic bouton localization, and (3) reduced number of NMJ branches. We demonstrated that the mispositioned NMJ boutons were preferentially positioned *at* or *just above* the sites devoid of BM components. We found that there was a correlation between the two phenotypes, i.e., the partial absence of main BM components and the ectopic bouton localization, showing that these two phenotypes were associated directly. Moreover, ultrastructural analysis of muscle 6/7 border by TEM showed that two muscles were connected through the mispositioned NMJ boutons. In particular, BMs beneath the mispositioned boutons were grossly deformed in the *dGlcAT-P* mutants. We found that there was a genetic interaction between *dC1GalT1* and *dGlcAT-P*. Additionally, ultrastructural analysis of NMJ boutons in *dC1GalT1* and *dGlcAT-P* mutants showed various defects, most of which were not common between the two mutants. However, shorter PSD length was observed in both *dC1GalT1* and *dGlcAT-P* mutant NMJs, suggesting that glucuronylated T antigen was required for the organization of PSD. Taken together, these results clearly showed that glucuronylated core 1 glycan produced by dC1GalT1 and dGlcAT-P was involved in the formation of BMs, positioning of NMJ boutons, arborization of NMJs, and organization of PSDs.

A previous report showed that in *Drosophila* embryos, expression levels of glucuronylated T antigen and T antigen occupied about 10% and 55%, respectively, of total *O*-glycan expression levels except for glycosaminoglycans (Aoki et al., 2008). In addition, in *Drosophila* larvae, the expression levels of glucuronylated T antigen and T antigen occupied about 18% and 45%, respectively (Kurz personal communication), showing that glucuronylated form of T antigen is upregulated during development. Although PNA lectin blotting and staining of muscle cells revealed that T antigen was poorly expressed in WT larvae, T antigen expression was remarkably increased in *dGlcAT-P* mutants (Fig. 11C–G and K), suggesting that most of the T antigens were glucuronylated by dGlcAT-P on the muscle surface. By contrast, at the NMJs, T antigen was richly expressed in WT larvae, and T antigen expression in *dGlcAT-P* mutants was only about 1.5 times higher than that in WT larvae (Fig. 11H–J″ and L), suggesting that the expression level of T antigen was higher than that of glucuronylated T antigen at the NMJs. Thus, the proportion of glucuronylated T antigen and T antigen expression levels differed between the larval muscles and NMJs. A previous study showed that both laminin B1 and B2 could bear T antigen (Lin et al., 2008). Their molecular weights were about 220 kDa and 180 kDa, respectively, both of which were determined by western blotting (Montell and Goodman, 1988). Our PNA lectin blotting revealed that the intensity of a band at about 180 kDa in *dGlcAT-P* mutants was higher than that in WT muscle extracts (Fig. 11C), implying that T antigen on laminin B2 might be glucuronylated by dGlcAT-P. Additionally, as laminin was expressed on the muscle surface and at NMJs (Bogdanik et al., 2008), we expected that the lack of glucuronylated T antigen on

laminin might cause the upregulated T antigen expression in the muscles and NMJs of *dGlcAT-P* mutants (Fig. 11E–L).

Previous studies showed that both dGlcAT-S and dGlcAT-P could catalyze glucuronylation of non-sulfated HNK-1 epitope (GlcAβ1-3Galβ1-4GlcNAc; Kim et al., 2003; Breloy et al., 2016). However, in larvae, its expression level was scarcely decreased despite the absence of dGlcAT-P enzyme (Pandey et al., 2011), suggesting that dGlcAT-P was not predominant enzyme catalyzing the glucuronylation of HNK-1 epitope.

A previous report revealed that fasciclin I (Fas I), which was homophilic cell adhesion molecule, controlled arborization of NMJs (Zhong and Shanley, 1995). NMJ morphology of *Fas I* overexpressed larvae resembled that of both *dC1GalT1* and *dGlcAT-P* mutant larvae. We therefore speculated that enhancement of cell adhesion between neuron and muscle cell might cause morphological defects of NMJs. As GlcA bears a minus charge, the surfaces of neuron and muscle cell can be negatively charged by glucuronylated core 1 glycans that can serve as an anti-adhesion molecule (Fig. 22). Therefore, we assumed that in *dC1GalT1* and *dGlcAT-P* mutants, neuron-muscle adhesion might be enhanced by the absence of glucuronylated core 1 glycans, leading to the morphological defects of NMJs, i.e., reduced number of NMJ branches and mislocalization of NMJ boutons.
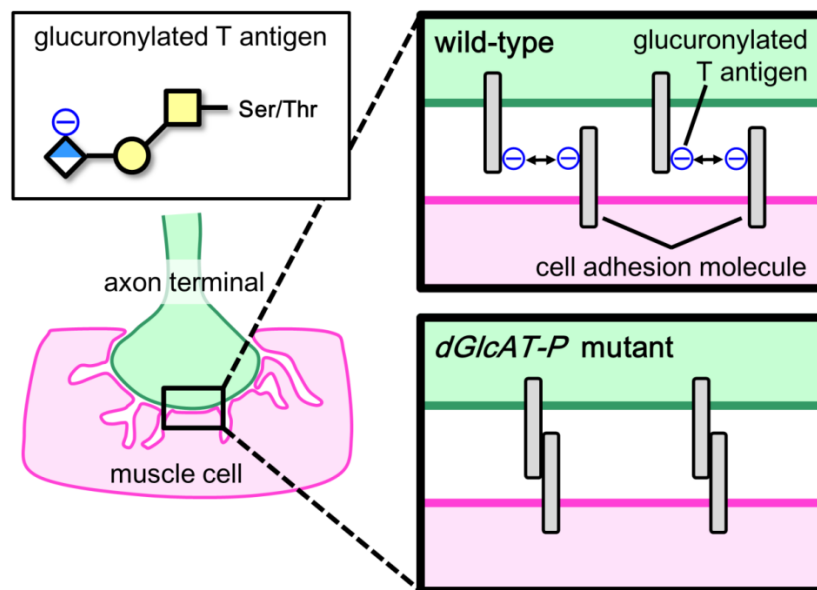

Fig. 22. Expected mechanism of aberrant NMJ morphology in *dGlcAT-P* mutants.
As GlcA has minus charge, glucuronylated T antigen is negatively charged. Given that homophilic cell adhesion molecules, which are expressed on pre- and postsynaptic cells, carry glucuronylated T antigen, adhesion between pre- and postsynaptic cells is diminished due to charge repulsion. However, in *dGlcAT-P* mutants, the adhesion between them is enhanced due to absence of the charge repulsion, resulting in the aberrant NMJ morphology, i.e., reduced number of NMJ branches and mislocalization of NMJ boutons.

As mentioned above, in *Drosophila*, some BM components produced in hemocytes (blood cells) and fat body are secreted to the body fluid and accumulate on various tissue surfaces. BMs are originally formed after the initial formation of NMJs at the late stage of embryogenesis and surround the surfaces of NMJ

bouton and muscle, except for the neuromuscular cleft. Our results revealed that in *dC1GalT1* and *dGlcAT-P* mutants, the NMJ boutons, through which muscle 6/7 were interconnected, were positioned just above the site devoid of Col IV or Ndg at the muscle 6/7 border (Figs. 15A). As a single BM (Col IV/Ndg-positive) surrounded the dorsal surfaces of mispositioned boutons and two muscles, we believed that the accumulation of BM components on the lateral surface of two muscles was physically blocked by the mispositioned boutons, resulting in the formation of BMs lacking Col IV and Ndg in that area (Fig. 23). Furthermore, ultrastructural analysis revealed that in *dGlcAT-P* mutants, Col IV/Ndg-deficient basal laminae beneath the mispositioned boutons were severely deformed, such as their duplication (Fig. 15E′ and G′). We considered two causes of basal lamina deformations in *dGlcAT-P* mutants. Firstly, the lack of Col IV and Ndg may cause those deformations. Additionally, as a previous report revealed that Col IV was essential for the deposition of perlecan into BMs (Pastor-Pareja and Xu, 2011), not only lack of Col IV and Ndg but also lack of perlecan may lead to the deformations. Secondly, we assumed that an absence of glucuronylated form of T antigen on laminin might cause the deformations. In *dGlcAT-P* mutants, the lack of glucuronylated T antigen on laminin might weaken the adhesion between the laminin localized in the basal lamina, and its receptors, e.g., integrin and dystroglycan, causing the dissociation between the basal laminae and plasma membranes. Thereafter, de novo formation of basal laminae on the plasma membranes results in their duplication.
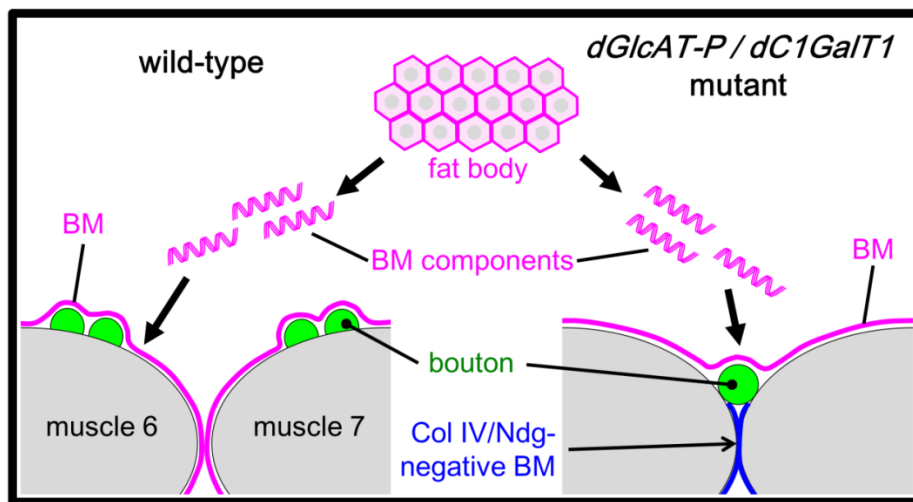

Fig. 23. Expected mechanism of loss of BM components in *dGlcAT-P* and *dC1GalT1* mutants.
In wild-types, NMJ boutons are formed away from the muscle 6/7 boundary. Subsequently, BM components (Col IV and Ndg) secreted from fat body accumulate on the surface of two muscles and boutons. Each muscle is individually surrounded by BM.
In *dGlcAT-P* and *dC1GalT1* mutants, NMJ boutons are formed at the muscle 6/7 boundary and connect the two muscles. Because BM components secreted from the fat body cannot pass through the cleft between bouton and muscle, the surfaces of two muscles and bouton are covered with a single BM, leading to the loss of BM components underneath the mislocalized bouton.

At the postsynaptic side of NMJs, the PSD composes a complex network of neurotransmitter receptors, adhesion proteins, signaling molecules, scaffolding molecules and ion channels (Harris and Littleton, 2015). Our ultrastructural observation of NMJ boutons demonstrated that both *dC1GalT1* and *dGlcAT-P* mutants displayed shorter PSD length (Fig. 20), suggesting that glucuronylated core 1 glycans was required for the

PSD organization. As DGluRs cluster at the PSDs, the shorter PSD length can cause the reduction in cluster size of DGluRs and the depression of neurotransmission in both *dC1GalT1* and *dGlcAT-P* mutants. As a previous report showed that sialylated form of core 1 glycan on α-dystroglycan played a role in AChR clustering on C2C12 cells, a mouse myoblast cell line (McDearmon et al., 2003), we assumed that at the *Drosophila* NMJs, glucuronylated T antigen might be essential for DGluR clustering.

dC1GalT1 mutant NMJs included many large endosome-like structures in presynaptic terminals and showed SSR deformations, while *dGlcAT-P* mutant NMJs did not exhibit those defects (Fig. 20). These observations suggested that those defects were attributed to reduced expression of T antigen but not glucuronylated T antigen. The large endosome-like structures observed in *dC1GalT1* mutant NMJs morphologically resembled those observed in endocytic mutants (Zhang et al., 1998; Guichet et al., 2002; Kasprowicz et al., 2008; Matta et al., 2012; Winther et al., 2013; West et al., 2015), indicating the possibility that T antigen may be involved in endocytosis in the presynaptic NMJ boutons. A previous report showed that a loss of β-spectrin expression caused SSR defects (Pielage et al., 2006), which resembled those observed in *dC1GalT1* mutant NMJs. Moreover, it was reported that at the *Drosophila* NMJs, spectrin was heterotetramer composed of α- and β-spectrins and could interact with the dystrophin-glycoprotein complex (DGC), which mechanically connected the extracellular matrix and cytoskeleton (Bogdanik et al., 2008). DGC contains glycoproteins carrying mucin-type *O*-glycans, e.g., laminin and dystroglycan (Haines et al., 2007; Bogdanik et al., 2008; Breloy et al., 2008; Lin et al., 2008; Nakamura et al., 2010). Therefore, it is possible that T antigen on those glycoproteins may be required for the stabilization of DGC and the formation of SSR.

dGlcAT-P mutant NMJs displayed four phenotypes that were never observed in *dC1GalT1* mutant NMJs (Fig. 20). In particular, (1) shorter diameter of synaptic vesicles, (2) reduced number of synaptic vesicles around the T-bar, (3) decreased number of large endosome-like structures, and (4) expansion of PSP depth were observed only in the *dGlcAT-P* mutant NMJs. Previous studies demonstrated that dGlcAT-P could also synthesize other glycan structures, such as glycosaminoglycans (Kim et al., 2003), and that loss of *sulfateless*, which was essential for the synthesis of heparan sulfate, resulted in decreased number of large endosome-like structures and expansion of PSP at the NMJs (Ren et al., 2009). Therefore, we assumed that those four phenotypes observed only in *dGlcAT-P* mutants might be attributed to the absence of glycan structures other than glucuronylated core 1 glycans.

We presumed that the reduced synaptic vesicle size led to a decreased amount of neurotransmitters in a synaptic vesicle and that the reduced number of vesicles around the T-bar diminished neurotransmitter release. Moreover, the shorter PSD length may lead to the suppression of neurotransmission because neurotransmitter receptors, such as DGluRs, are localized at the PSD, as mentioned above. However, both *dGlcAT-P* and *dC1GalT1* mutant larvae showed normal locomotor activity (Fig. 21), suggesting that in this case, the larval locomotion was not affected by aberrant neurotransmission at the NMJs.

In conclusion, our analyses showed that glucuronylated core 1 glycan produced by dC1GalT1 and dGlcAT-P regulated the arborization of NMJs, positioning of NMJ boutons, and formation of the BMs on *Drosophila* muscles. Furthermore, ultrastructural observation of NMJ boutons suggested that glucuronylated

core 1 glycan could be required for the PSD organization. This study unraveled for the first time the physiological roles of glucuronylated core 1 glycan in *Drosophila*. Future analyses will identify the core protein carrying glucuronylated core 1 glycan and clarify the molecular mechanism underlying the positioning of NMJ boutons.

5. Acknowledgments

6. References

Anumula, K., Taylor, P., 1992. A comprehensive procedure for preparation of partially methylated alditol acetates from glycoprotein carbohydrates. Anal. Biochem. 203, 101–8.

Aoki, K., Perlman, M., Lim, J.-M.M., Cantu, R., Wells, L., Tiemeyer, M., 2007. Dynamic developmental elaboration of *N*-linked glycan complexity in the *Drosophila melanogaster* embryo. J. Biol. Chem. 282, 9127–42.

Aoki, K., Porterfield, M., Lee, S.S., Dong, B., Nguyen, K., McGlamry, K.H., Tiemeyer, M., 2008. The diversity of *O*-linked glycans expressed during *Drosophila melanogaster* development reflects stage- and tissue-specific requirements for cell signaling. J. Biol. Chem. 283, 30385–400.

Bogdanik, L., Framery, B., Frölich, A., Franco, B., Mornet, D., Bockaert, J., Sigrist, S.J., Grau, Y., Parmentier, M.-L.L., 2008. Muscle dystroglycan organizes the postsynapse and regulates presynaptic neurotransmitter release at the *Drosophila* neuromuscular junction. PLoS One 3, e2084.

Breloy, I., Schwientek, T., Althoff, D., Holz, M., Koppen, T., Krupa, A., Hanisch, F.-G.G., 2016. Functional analysis of the glucuronyltransferases GlcAT-P and GlcAT-S of *Drosophila melanogaster*: Distinct activities towards the *O*-linked T-antigen. Biomolecules 6, 8.

Breloy, I., Schwientek, T., Lehr, S., Hanisch, F.-G.G., 2008. Glucuronic acid can extend *O*-linked core 1 glycans, but it contributes only weakly to the negative surface charge of *Drosophila melanogaster* Schneider-2 cells. FEBS Lett. 582, 1593–8.

Brockhausen, I., 1999. Pathways of *O*-glycan biosynthesis in cancer cells. Biochim. Biophys. Acta 1473, 67–95.

Budnik, V., Koh, Y.H., Guan, B., Hartmann, B., Hough, C., Woods, D., Gorczyca, M., 1996. Regulation of synapse structure and function by the *Drosophila* tumor suppressor gene *dlg*. Neuron 17, 627–40.

Chiba, A., Hing, H., Cash, S., Keshishian, H., 1993. Growth cone choices of *Drosophila* motoneurons in response to muscle fiber mismatch. J. Neurosci. 13, 714–32.

Coppin, A., Maes, E., Flahaut, C., Coddeville, B., Strecker, G., 1999. Acquisition of species-specific *O*-linked carbohydrate chains from oviducal mucins in *Rana arvalis*. Eur. J. Biochem, 266, 370–82.

Deerinck, T.J., Bushong, E.A., Thor, A., Ellisman, M.H., 2010. NCMIR methods for 3D EM: a new protocol for preparation of biological specimens for serial blockage scanning electron microscopy. Microscopy 6–8.

Available at: http://ncmir.ucsd.edu/sbfsem-protocol.pdf.

Denef, N., Chen, Y., Weeks, S.D., Barcelo, G., Schüpbach, T., 2008. Crag regulates epithelial architecture and polarized deposition of basement membrane proteins in *Drosophila*. Dev. Cell 14, 354–64.

Doyonnas, R., Kershaw, D.B., Duhme, C., Merkens, H., Chelliah, S., Graf, T., McNagny, K.M., 2001. Anuria, omphalocele, and perinatal lethality in mice lacking the CD34-related protein Podocalyxin. J. Exp. Med. 194, 13–27.

Florea, D., Maes, E., Strecker, G., 1997. Primary structure of seven sulfated oligosaccharide-alditols released by reductive beta-elimination from oviducal mucins of *Rana temporaria*. Characterization of the sequence HSO$_3$(3)GlcA(β1-3)Gal. Carbohydr. Res. 302, 179–89.

Fu, J., Gerhardt, H., McDaniel, J., Xia, B., Liu, X., Ivanciu, L., Ny, A., Hermans, K., Silasi-Mansat, R., McGee, S., Nye, E., Ju, T., Ramirez, M., Carmeliet, P., Cummings, R., Lupu, F., Xia, L., 2008. Endothelial cell *O*-glycan deficiency causes blood/lymphatic misconnections and consequent fatty liver disease in mice. J. Clin. Invest. 118, 3725–37.

Fu, J., Wei, B., Wen, T., Johansson, M., Liu, X., Bradford, E., Thomsson, K., McGee, S., Mansour, L., Tong, M., McDaniel, J., Sferra, T., Turner, J., Chen, H., Hansson, G., Braun, J., Xia, L., 2011. Loss of intestinal core 1-derived *O*-glycans causes spontaneous colitis in mice. J. Clin. Invest. 121, 1657–66.

Fuwa, T.J., Kinoshita, T., Nishida, H., Nishihara, S., 2015. Reduction of T antigen causes loss of hematopoietic progenitors in *Drosophila* through the inhibition of filopodial extensions from the hematopoietic niche. Dev. Biol. 401, 206–19.

Guichet, A., Wucherpfennig, T., Dudu, V., Etter, S., Wilsch-Bräuniger, M., Hellwig, A., González-Gaitán, M., Huttner, W.B., Schmidt, A.A., 2002. Essential role of endophilin A in synaptic vesicle budding at the *Drosophila* neuromuscular junction. EMBO J. 21, 1661–72.

Guzman-Aranguez, A., Argüeso, P., 2010. Structure and biological roles of mucin-type *O*-glycans at the ocular surface. Ocul. Surf. 8, 8–17.

Guérardel, Y., Lanzino, L., Maes, E., Leroy, Y., Coddeville, B., Oriol, R., Strecker, G., 2001. The nematode *Caenorhabditis elegans* synthesizes unusual *O*-linked glycans: identification of glucose-substituted mucin-type *O*-glycans and short chondroitin-like oligosaccharides. Biochem. J. 357, 167–82.

Haines, N., Seabrooke, S., Stewart, B.A., 2007. Dystroglycan and protein *O*-mannosyltransferases 1 and 2

are required to maintain integrity of *Drosophila* larval muscles. Mol. Biol. Cell 18, 4721–30.

Harris, K., Littleton, T., 2015. Transmission, development, and plasticity of synapses. Genetics 201, 345–75.

Ichimiya, T., Manya, H., Ohmae, Y., Yoshida, H., Takahashi, K., Ueda, R., Endo, T., Nishihara, S., 2004. The twisted abdomen phenotype of *Drosophila POMT1* and *POMT2* mutants coincides with their heterophilic protein *O*-mannosyltransferase activity. J. Biol. Chem. 279, 42638–47.

Ju, T., Brewer, K., D'Souza, A., Cummings, R.D., Canfield, W.M., 2002a. Cloning and expression of human core 1 β1,3-galactosyltransferase. J. Biol. Chem. 277, 178–86.

Ju, T., Cummings, R.D., 2002. A unique molecular chaperone Cosmc required for activity of the mammalian core 1 β3-galactosyltransferase. Proc. Natl. Acad. Sci. U.S.A. 99, 16613–18.

Ju, T., Cummings, R.D., 2005. Protein glycosylation: chaperone mutation in Tn syndrome. Nature 437, 1252.

Ju, T., Cummings, R.D., Canfield, W.M., 2002b. Purification, characterization, and subunit structure of rat core 1 β1,3-galactosyltransferase. J. Biol. Chem. 277, 169–77.

Kasprowicz, J., Kuenen, S., Miskiewicz, K., Habets, R.L., Smitz, L., Verstreken, P., 2008. Inactivation of clathrin heavy chain inhibits synaptic recycling but allows bulk membrane uptake. J. Cell Biol. 182, 1007–16.

Kim, B.-T.T., Tsuchida, K., Lincecum, J., Kitagawa, H., Bernfield, M., Sugahara, K., 2003. Identification and characterization of three *Drosophila melanogaster* glucuronyltransferases responsible for the synthesis of the conserved glycosaminoglycan-protein linkage region of proteoglycans. Two novel homologs exhibit broad specificity toward oligosaccharides from proteoglycans, glycoproteins, and glycosphingolipids. J. Biol. Chem. 278, 9116–24.

Kondo, S., Ueda, R., 2013. Highly improved gene targeting by germline-specific Cas9 expression in *Drosophila*. Genetics 195, 715–21.

Koper, A., Schenck, A., Prokop, A., 2012. Analysis of adhesion molecules and basement membrane contributions to synaptic adhesion at the *Drosophila* embryonic NMJ. PLoS One 7, e36339.

Kramerov, A.A., Arbatsky, N.P., Rozovsky, Y.M., Mikhaleva, E.A., Polesskaya, O.O., Gvozdev, V.A., Shibaev, V.N., 1996. Mucin-type glycoprotein from *Drosophila melanogaster* embryonic cells: characterization of carbohydrate component. FEBS Lett. 378, 213–8.

Kudo, T., Sato, T., Hagiwara, K., Kozuma, Y., Yamaguchi, T., Ikehara, Y., Hamada, M., Matsumoto, K., Ema, M., Murata, S., Ohkohchi, N., Narimatsu, H., Takahashi, S., 2013. *C1galt1*-deficient mice exhibit thrombocytopenia due to abnormal terminal differentiation of megakaryocytes. Blood 122, 1649–57.

Kurz, S., Aoki, K., Jin, C., Karlsson, N.G., Tiemeyer, M., Wilson, I.B., Paschinger, K., 2015. Targeted release and fractionation reveal glucuronylated and sulphated *N*- and *O*-glycans in larvae of dipteran insects. J. Proteomics 126, 172–88.

Kusche-Gullberg, M., Garrison, K., MacKrell, A.J., Fessler, L.I., Fessler, J.H., 1992. Laminin A chain: expression during *Drosophila* development and genomic sequence. EMBO J. 11, 4519–27.

Le Parco, Y., Knibiehler, B., Cecchini, J.P., Mirre, C., 1986. Stage and tissue-specific expression of a *collagen* gene during *Drosophila melanogaster* development. Exp. Cell Res. 163, 405–12.

Lin, Y.-R.R., Reddy, B.V.V., Irvine, K.D., 2008. Requirement for a core 1 galactosyltransferase in the *Drosophila* nervous system. Dev. Dyn. 237, 3703–14.

Martin, D., Zusman, S., Li, X., Williams, E.L., Khare, N., DaRocha, S., Chiquet-Ehrismann, R., Baumgartner, S., 1999. *wing blister*, a new *Drosophila* laminin α chain required for cell adhesion and migration during embryonic and imaginal development. J. Cell Biol. 145, 191–201.

Matta, S., Kolen, K. Van, Cunha, R. da, Bogaart, G. van den, Mandemakers, W., Miskiewicz, K., Bock, P.-J.J. De, Morais, V.A., Vilain, S., Haddad, D., Delbroek, L., Swerts, J., Chávez-Gutiérrez, L., Esposito, G., Daneels, G., Karran, E., Holt, M., Gevaert, K., Moechars, D.W., Strooper, B. De, Verstreken, P., 2012. LRRK2 controls an EndoA phosphorylation cycle in synaptic endocytosis. Neuron 75, 1008–21.

McDearmon, E.L., Combs, A.C., Ervasti, J.M., 2003. Core 1 glycans on α-dystroglycan mediate laminin-induced acetylcholine receptor clustering but not laminin binding. J. Biol. Chem. 278, 44868–73.

Mehta, N., Porterfield, M., Struwe, W.B., Heiss, C., Azadi, P., Rudd, P.M., Tiemeyer, M., Aoki, K., 2016. Mass spectrometric quantification of *N*-Linked glycans by reference to exogenous standards. J. Proteome Res. 15, 2969–80.

Memtily, N., Okada, T., Ebihara, T., Sato, M., Kurabayashi, A., Furihata, M., Suga, M., Nishiyama, H., Mio, K., Sato, C., 2015. Observation of tissues in open aqueous solution by atmospheric scanning electron microscopy: applicability to intraoperative cancer diagnosis. Int. J. Oncol. 46, 1872–82.

Montell, D.J., Goodman, C.S., 1988. *Drosophila* substrate adhesion molecule: sequence of laminin B1 chain reveals domains of homology with mouse. Cell 53, 463–73.

Morin, X., Daneman, R., Zavortink, M., Chia, W., 2001. A protein trap strategy to detect GFP-tagged proteins expressed from their endogenous loci in *Drosophila*. Proc. Natl. Acad. Sci. U.S.A 98, 15050–5.

Mourad, R., Morelle, W., Neveu, A., Strecker, G., 2001. Diversity of *O*-linked glycosylation patterns between species. Characterization of 25 carbohydrate chains from oviducal mucins of *Rana ridibunda*. Eur. J. Biochem. 268, 1990–2003.

Müller, R., Hülsmeier, A.J., Altmann, F., Ten Hagen, K., Tiemeyer, M., Hennet, T., 2005. Characterization of mucin-type core-1 β1-3 galactosyltransferase homologous enzymes in *Drosophila melanogaster*. FEBS J. 272, 4295–305.

Nakamura, N., Stalnaker, S.H., Lyalin, D., Lavrova, O., Wells, L., Panin, V.M., 2010. *Drosophila* Dystroglycan is a target of *O*-mannosyltransferase activity of two protein *O*-mannosyltransferases, Rotated Abdomen and Twisted. Glycobiology 20, 381–94.

Narimatsu, Y., Ikehara, Y., Iwasaki, H., Nonomura, C., Sato, T., Nakanishi, H., Narimatsu, H., 2008. Immunocytochemical analysis for intracellular dynamics of C1GalT associated with molecular chaperone, Cosmc. Biochem. Biophys. Res. Commun. 366, 199–205.

Nishiyama, H., Suga, M., Ogura, T., Maruyama, Y., Koizumi, M., Mio, K., Kitamura, S., Sato, C., 2010. Atmospheric scanning electron microscope observes cells and tissues in open medium through silicon nitride film. J. Struct. Biol. 172, 191–202.

Pan, Y., Yago, T., Fu, J., Herzog, B., McDaniel, J.M., Padmaja, Cai, X., Changgeng, Rodger P, Christopher, Kesheng, Chen, H., Lijun, 2014. Podoplanin requires sialylated *O*-glycans for stable expression on lymphatic endothelial cells and for interaction with platelets. Blood 124, 3656–65.

Pandey, R., Blanco, J., Udolph, G., 2011. The glucuronyltransferase *GlcAT-P* is required for stretch growth of peripheral nerves in *Drosophila*. PLoS One 6, e28106.

Paschinger, K., Wilson, I.B., 2015. Comparative glycobiology. In: Taniguchi, N., Endo, T., Hart, G.W., Seeberger, P.H., Wong, C.-H. (Eds.), Glycoscience: Biology and Medicine. Springer, Tokyo, 795–805.

Pastor-Pareja, J.C., Xu, T., 2011. Shaping cells and organs in *Drosophila* by opposing roles of fat body-secreted Collagen IV and perlecan. Dev. Cell. 21, 245–56.

Pielage, J., Fetter, R.D., Davis, G.W., 2006. A postsynaptic spectrin scaffold defines active zone size, spacing, and efficacy at the *Drosophila* neuromuscular junction. J. Cell Biol. 175, 491–503.

Prokop, A., 1999. Integrating bits and pieces: synapse structure and formation in *Drosophila* embryos. Cell Tissue Res. 297, 169–86.

Ren, Y., Kirkpatrick, C., Rawson, J., Sun, M., Selleck, S., 2009. Cell type-specific requirements for heparan sulfate biosynthesis at the *Drosophila* neuromuscular junction: Effects on synapse function, membrane trafficking, and mitochondrial localization. J. Neurosci. 29, 8539–50.

Schwientek, T., Mandel, U., Roth, U., Müller, S., Hanisch, F.-G.G., 2007. A serial lectin approach to the mucin-type *O*-glycoproteome of *Drosophila melanogaster* S2 cells. Proteomics 7, 3264–77.

Sorrosal, G., Pérez, L., Herranz, H., Milán, M., 2010. Scarface, a secreted serine protease-like protein, regulates polarized localization of laminin A at the basement membrane of the *Drosophila* embryo. EMBO Rep. 11, 373–9.

Timpl, R., 1989. Structure and biological activity of basement membrane proteins. Eur. J. Biochem. 180, 487–502.

Ueyama, M., Akimoto, Y., Ichimiya, T., Ueda, R., Kawakami, H., Aigaki, T., Nishihara, S., 2010. Increased apoptosis of myoblasts in *Drosophila* model for the Walker-Warburg syndrome. PLoS One 5, e11557.

Verstreken, P., Kjaerulff, O., Lloyd, T.E., Atkinson, R., Zhou, Y., Meinertzhagen, I.A., Bellen, H.J., 2002. *Endophilin* mutations block clathrin-mediated endocytosis but not neurotransmitter release. Cell 109, 101–12.

Wang, Y., Ju, T., Ding, X., Xia, B., Wang, W., Xia, L., He, M., Cummings, R.D., 2010. Cosmc is an essential chaperone for correct protein *O*-glycosylation. Proc. Natl. Acad. Sci. U.S.A. 107, 9228–33.

West, R.J., Lu, Y., Marie, B., Gao, F.-B.B., Sweeney, S.T., 2015. Rab8, POSH, and TAK1 regulate synaptic growth in a *Drosophila* model of frontotemporal dementia. J. Cell Biol. 208, 931–47.

Winther, Å.M.M., Jiao, W., Vorontsova, O., Rees, K.A., Koh, T.-W.W., Sopova, E., Schulze, K.L., Bellen, H.J., Shupliakov, O., 2013. The dynamin-binding domains of Dap160/intersectin affect bulk membrane retrieval in synapses. J. Cell Sci. 126, 1021–31.

Xia, L., Ju, T., Westmuckett, A., An, G., Ivanciu, L., McDaniel, J.M., Lupu, F., Cummings, R.D., McEver, R.P., 2004. Defective angiogenesis and fatal embryonic hemorrhage in mice lacking core 1-derived *O*-glycans. J. Cell Biol. 164, 451–9.

Xia, L., McEver, R.P., 2006. Targeted disruption of the gene encoding core 1 β1-3-galactosyltransferase (T-synthase) causes embryonic lethality and defective angiogenesis in mice. Meth. Enzymol. 416, 314–31.

Yang, Z., Bennett, E.P., Jørgensen, B., Drew, D.P., Arigi, E., Mandel, U., Ulvskov, P., Levery, S.B., Clausen, H., Petersen, B.L., 2012. Toward stable genetic engineering of human *O*-glycosylation in plants. Plant Physiol. 160, 450–63.

Yasothornsrikul, S., Davis, W.J., Cramer, G., Kimbrell, D.A., Dearolf, C.R., 1997. *viking*: identification and characterization of a second type IV collagen in *Drosophila*. Gene 198, 17–25.

Yoshida, H., Fuwa, T.J., Arima, M., Hamamoto, H., Sasaki, N., Ichimiya, T., Osawa, K.-I., Ueda, R., Nishihara, S., 2008. Identification of the *Drosophila core 1 β1,3-galactosyltransferase* gene that synthesizes T antigen in the embryonic central nervous system and hemocytes. Glycobiology 18, 1094–104.

Yurchenco, P.D., Schittny, J.C., 1990. Molecular architecture of basement membranes. FASEB J. 4, 1577–90.

Zhang, B., Koh, Y.H., Beckstead, R.B., Budnik, V., Ganetzky, B., Bellen, H.J., 1998. Synaptic vesicle size and number are regulated by a clathrin adaptor protein required for endocytosis. Neuron 21, 1465–75.

Zhong, Y., Shanley, J., 1995. Altered nerve terminal arborization and synaptic transmission in *Drosophila* mutants of cell adhesion molecule Fasciclin I. J. Neurosci. 15, 6679–87.